UC Santa Barbara
UC Santa Barbara Electronic Theses and Dissertations

Title

Imaging Channel Connectivity in Proton and Hydroxide Conducting Membranes for Fuel Cells

Permalink

https://escholarship.org/uc/item/1mb8g2w0

Author

Barnes, Austin

Publication Date

2019

Peer reviewed|Thesis/dissertation

UNIVERSITY OF CALIFORNIA

Santa Barbara

Imaging Channel Connectivity in Proton and Hydroxide Conducting Membranes for Fuel

Cells

A dissertation submitted in partial satisfaction of the

requirements for the degree Doctor of Philosophy

in Chemistry

by

Austin Michael Barnes

Committee in charge:

Professor Steven Buratto, Chair

Professor Horia Metiu

Professor Quyen Nguyen

Professor Craig Hawker

December 2019

The dissertation of Austin Michael Barnes is approved.

_____

Craig Hawker

_____

Quyen Nguyen

_____

Horia Metiu

_____

Steven Buratto, Committee Chair

December 2019

Imaging Channel Connectivity in Proton and Hydroxide Conducting Membranes for Fuel

Cells

DEDICATION

       This dissertation is dedicated in memory of Dr. Samuel Boldissar. His selflessness and avid curiosity was remarkable, and he will be truly missed.

ACKNOWLEDGEMENTS

VITA OF AUSTIN MICHAEL BARNES
December 2019

<u>EDUCATION:</u>

University of California, Santa Barbara
Ph.D. Chemistry, December 2019

University of Massachusetts, Amherst
B.S. Physics with Honors, Minor in Mathematics
Integrated Concentration in Science (iCons), Renewable Energy Track
Graduated May 2014, *Cum Laude*

<u>PUBLICATIONS:</u>

Austin M. Barnes, Yifeng Du, Brendan Liu, Wenxu Zhang, Soenke Seifert, E. Bryan Coughlin, Steven K. Buratto. Effect of Surface Alignment on Connectivity in Phosphonium-Containing Diblock Copolymer Anion Exchange Membranes. *Submitted to J. Phys. Chem. C (9/10/19).*

Austin M. Barnes, Brendan Liu, Steven K. Buratto. Humidity-dependent Surface Morphology and Hydroxide Conductance of a Model Quaternary Ammonium Anion Exchange Membrane. *Corrections re-submitted to Langmuir (8/29/19).*

Austin M. Barnes, Yifeng Du, Wenxu Zhang, Soenke Seifert, Steven K. Buratto, E. Bryan Coughlin. Phosphonium-Containing Block Copolymer Anion Exchange Membranes: Effect of Quaternization on Bulk and Surface Morphology at Hydrated and Dehydrated States. *Macromolecules* 2019. *52* (16), 6097-6106. doi: 10.1021/acs.macromol.9b00665

Austin M. Barnes and Steven K. Buratto. Imaging Channel Connectivity in Nafion Using Electrostatic Force Microscopy. *J. Phys. Chem. B* 2018, *122* (3), 1289-1295. doi: 10.1021/acs.jpcb.7b08230

Austin M. Barnes and Anthony D. Dinsmore. Heterogeneity of Surface Potential in Contact Electrification Under Ambient Conditions: A Comparison Between Pre- and Post-contact States. *J. Electrostat.* 2016, *81*, 76-81. doi: 10.1016/j.elstat.2016.04.002

Nicholas J. Economou, Austin M. Barnes, Andrew J. Wheat, Mark S. Schaberg, Steven J. Hamrock and Steven K. Buratto. Investigation of Humidity Dependent Surface Morphology and Proton Conductivity in Multi Acid Side Chain Membranes by Conductive Probe Atomic Force Microscopy. *J. Phys. Chem. B.* 2015, *119,* 14280–14287. doi: 10.1021/acs.jpcb.5b07255

Austin M. Barnes, Mina Baghar, Emily Pentzer, Adam J. Wise, Brenton A.G. Hammer, Todd Emrick, Anthony D. Dinsmore, Michael D. Barnes. Morphology-Dependent

Electronic Properties in Cross-linked (P3HT-*b*-P3MT) Block Copolymer Nanostructures. *ACS Nano* 2014, *8* (8), 8344-8349.

PRESENTATIONS:

"Probing the Nanoscale Morphology and Conductance of Anion Exchange Membrane Fuel Cells by Atomic Force Microscopy (AFM)." Electrochemical Society Meeting. (May 2019) *Contributed Talk*

"Investigation of Morphology and Conductance of Anion Block Copolymer Membranes for Anion Exchange Membrane Fuel Cells Using Atomic Force Microscopy." American Physical Society Meeting. (March 2018) *Contributed talk*

"Investigation of Surface Morphology and Conductance of Multi-Acid Side Chain Membranes by Atomic Force Microscopy." American Chemical Society Meeting. (March 2016) *Contributed talk*

"A Microscopic View of Contact Electrification." Senior Symposium held at UMass. Presented my senior year thesis project studying surface charge pattern using KPFM (May 2014). *Invited talk*

"A Microscopic View of Contact Electrification." 20th Annual Undergraduate Research Conference held at UMass. (May 2014) *Poster Presentation*

"A Microscopic View of Contact Electrification." New England Complex Fluids workshop held at UMass. (June 2013) *Contributed talk*

AWARDS AND HONORS:

Graduate Division Dissertation Fellowship (2019)

Departmental Fellowship (2014)

Commonwealth Honors College Research Grant (2013)

Craig and Suzanne Cervo Undergraduate Research Fund (2012)

TEACHING EXPERIENCE:

Teaching Assistant
Department of Chemistry, University of California Santa Barbara
Physical Chemistry Lab (CHEM 116BL) – guided junior and senior chemistry majors (~18 students) through 8-week experiment using advanced experimental techniques (UV-Vis,

fluorimetry, CV, time-resolved photoluminescence) and proper scientific writing. (Spring 2017, Spring 2018)

Analytical Chemistry Lab (CHEM 116AL) – guided junior chemistry majors (~18 students) through 4 experiments using analytical techniques (gravimetric analysis, UV-Vis, AAS, CV, fluorimetry) and proper scientific writing. (Winter 2017)

Thermodynamics (CHEM 113A) – developed lectures for section and held office hours for ~ 70 students majoring in Chemistry. (Fall 2018)

Statistical Mechanics (CHEM 113C) – developed lectures for section and held office hours for ~ 150 students majoring in Chemistry. (Spring 2016)

Analytical Chemistry Lecture (CHEM 150) – lead office hours, graded homework and exams for ~ 150 students majoring in Chemistry and Chemical Engineering. (Fall 2015, Fall 2017)

General Chemistry Lab (1BL) –developed lectures, demonstrated lab techniques, and wrote quizzes. (Fall 2014 – Summer 2015, Winter 2016)

Mentoring
Have trained and guided:
Alejandra Acosta-Hernandez, 3rd year Chemistry major, California Alliance for Minority Participation (CAMP) MRL Intern (Spring 2019 – present).

Nicolle Hall, 2nd year Chemistry major at Jackson State University, University of California Faculty and Historically Black College and Universities (UC-HCBU) Initiative (Summer 2019).

Brendan Liu, Chemistry major (Fall 2017 – present).

Conor Collins, Chemistry major (Spring 2017-Summer 2018). Graduated in 2018 and now teaching high school chemistry in Seattle, WA.

Chandler Nelson, senior at Ventura High School (2015-2016). Now at UCLA majoring in chemistry.

Outreach
SCOPE – 50 minute presentations to local high schools on graduate research
(2015)

NanoDays – Volunteered workshops at Santa Barbara National History Museum
(2016)

ABSTRACT

Imaging Channel Connectivity in Proton and Hydroxide Conducting Membranes for Fuel

Cells

by

Austin Michael Barnes

Proton exchange membrane (PEM) fuel cells offer an alternative as an efficient power

source with low environmental impact. The heart of the fuel cell is the membrane, which

conducts protons through an aqueous channel network. Proton transport is critically tied to

the channel connectivity – disconnected channels do not participate in the overall

electrochemical activity of the cell. Nafion, the current benchmark PEM, is a random

statistical copolymer, characterized by a percolating network of cylindrical channels. In

previous work, conductive-probe atomic force microscopy (cp-AFM) was used to image the

conductance of Nafion. Although cp-AFM provides relevant information on which channels

are connected, it provides no information on the disconnected "dead-end" channels at the

surface. Electrostatic Force Microscopy (EFM) was used to analyze the structure and

frequency of the "dead-end" channels. Applying a simple parallel plate model allowed us to

assign differences in the EFM signal to particular channel shapes: connected cylindrical

channels, "dead-end" cylinder channels, and bottle-neck channels.

Anion exchange membranes (AEMs), which conduct hydroxide, have attracted recent interest due to improved reaction kinetics in alkaline media, yet suffer from low conductivity and easily degrade. To this end, our AFM methodology was applied to analyze the channel connectivity of a commercial FumaTech AEM was investigated in its hydroxide form over a wide range of relative humidity (RH) by combining phase imaging and cp-AFM. At high RH, our AFM data indicates significant surface swelling. Lastly, we investigated a class of phosphonium-containing diblock copolymer AEMs that formed ordered morphologies. Although channels were observed to be well-connected in the bulk by TEM, channels aligned parallel at the surface leading to many "dead-end" channels shown by EFM. Correlating these findings with bulk measurements could offer insight toward AEMs with improved conductivity and chemical stability.

TABLE OF CONTENTS

LIST OF ABBREVIATIONS

ACF:	Autocorrelation Function
AEM:	Anion Exchange Membrane
AEMFC:	Anion Exchange Membrane Fuel Cell
AFM:	Atomic Force Microscopy
CMS:	Chloromethylstyrene
Cp-AFM:	Conductive-probe Atomic Force Microscopy
DCM:	Dichloromethane
DP:	Degree of Polymerization
DMF:	Dimethylformamide
EFM:	Electrostatic Force Microscopy
EW:	Equivalent Weight
FTO:	Fluorine-doped Tin Oxide
GDE:	Gas Diffusion Electrode
GPC:	Gas Phase Chromatography
HPC:	Hexagonal Close Packing
IEC:	Ion Exchange Capacity
KPFM:	Kelvin Probe Force Microscopy
MaxEnt:	Maximum Entropy
MEA:	Membrane Electrode Assembly
NMR:	Nuclear Magnetic Resonance
NMP:	Nitroxide Mediated Polymerization
PEM:	Proton Exchange Membrane
PEMFC:	Proton Exchange Membrane Fuel Cell
PFSA:	Perfluorosulfonic acid
PFIA:	Perfluoroimide acid
PIp:	Polyisoprene
PCMS:	Polychloromethylstyrene
$P(Ph(OMe)_3)_3$:	tris(2,4,6-trimethoxyphenyl)phosphine
$P(Ph)_3$:	tris(2,4,6-trimethyl)phosphine:
PPO:	Poly(phenylene oxide)
PSD:	Power Spectral Density
QA:	Quaternary Ammonium
QP:	Quaternary Phosphonium
RAFT:	Reversible Addition-fragmentation Chain Transfer
RH:	Relative Humidity
SAXS:	Small-Angle X-ray Scattering
SCFT-LS:	Self-consistent Field Theory – Liquid State
SG1:	*N-tert*-butyl-*N*-[1-diethylphosphono-(2,2-dimethylpropyl)] nitroxide
TEM:	Transmission Electron Microscopy
T_g:	Glass Transition Temperature
THF:	Tetrahydrofuran
VRFB:	Vanadium Redox Flow Battery

LIST OF FIGURES AND TABLES

xvii

xviii

I. Introduction

A. PEM Fuel Cells and Current Challenges

Fuel cells are an electrochemical energy conversion device that convert chemical energy from fuel into electricity with high efficiency and little to no greenhouse gas emission. Fuel cells are composed of a cathode, anode, and electrolyte. They differ from batteries as they require a constant supply of reactant fuel. Although several types of fuel cells exist – varying in electrolyte, reactant, electrode structure, and operating temperature – this thesis work focuses on polymer electrolyte membrane (or proton exchange membrane) fuel cells.

The proton exchange membrane (PEM) fuel cell (PEMFC) depicted in the schematic of Fig. 1.1 consists of hydrogen and oxygen gas that is supplied to the anode and cathode, respectively. The carbon electrodes are a carbon cloth gas diffusion layer with a thin catalyst layer decorated by nanometer-size platinum particles. The catalyst facilitates the half reactions: the standard hydrogen reaction at the anode and the oxygen reduction reaction (ORR) at the cathode. The membrane conducts protons through an aqueous channel network while insulating electrons and separating the reactants. Protons react with electrons and oxygen at the cathode to produce water.

PEM Fuel Cell

Catalyst layer   Membrane   Gas diffusion layer

Platinum

H^+

Anode

$H_2(g) \rightarrow 2H^+ + 2e^-$

Cathode

$2H^+ + 2e^- + \frac{1}{2}O_2(g) \rightarrow H_2O(l)$

Overall Reaction

$H_2(g) + \frac{1}{2}O_2(g) \rightarrow H_2O(l)$

$E^0_{cell} = 1.23\ V$

e^- e^-
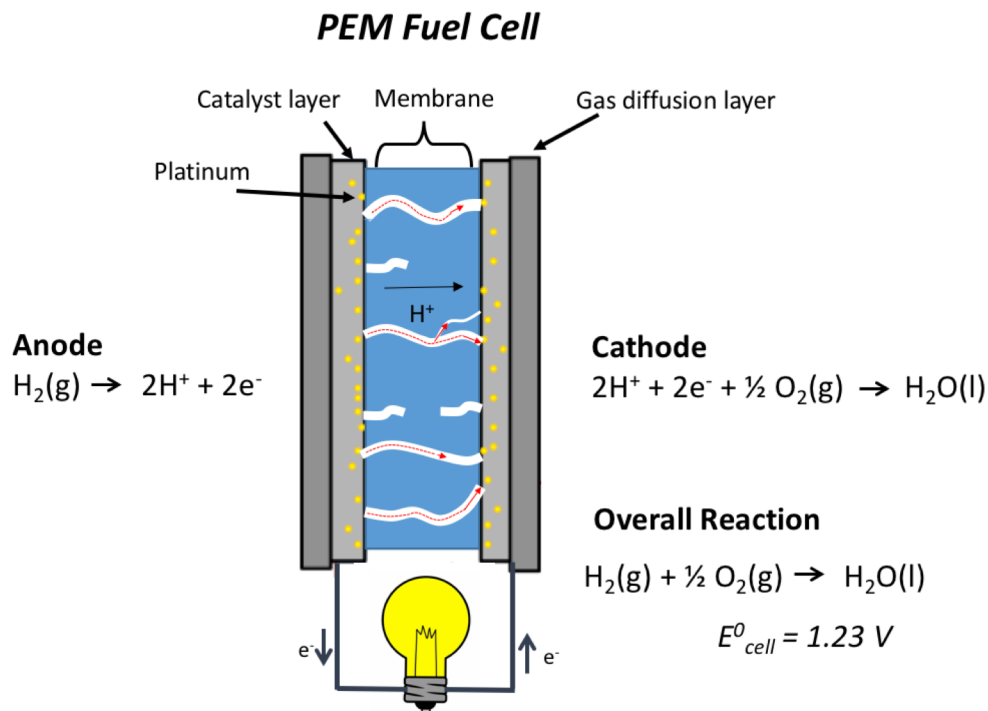
Figure 1.1: Schematic of a PEMFC in which the PEM conducts protons through a random aqueous channel network. Red highlighted channels depict channels that are connected and contribute to the activity of the cell.

Although great progress has been made over the past few decades from improving the cell performance, durability, and cost efficiency, these facets have still impeded commercialization. A significant research effort has focused on the cathode where the ORR kinetics are typically slow.[1] For this reason, the cathode requires higher platinum loadings than the anode. Platinum raises the cost of production, which accounts for ~25% of the total cost.[2] Several strategies have aimed at reducing the platinum loading while increasing its utilization, such as electro-spraying and pulse potential deposition techniques;[3,4] however with its susceptibility to CO poisoning, alternatives such as non-precious metals as well as Platinum group metal-free catalysts have garnered interest.[5–7]

The sluggishness of the ORR can be overcome by operating the fuel cell at higher temperatures; however, this is limited by the membrane's glass transition temperature and its ability to retain water at higher temperatures. DuPont's Nafion has been the benchmark PEM due its high proton conductivity with high chemical and mechanical stability at high temperatures with a glass transition temperature of ~130 °C.[8] Nafion is a random statistical copolymer that consists of a Teflon-like fluorocarbon backbone and a sulfonic acid side-chain. The chemical structure of Nafion is shown in Fig. 1.2. When cast into a film, these components phase separate into hydrophilic proton conducting channels surrounded by a semi-crystalline hydrophobic matrix with channel size 5-10 nm in width. At extremely high temperatures, the membrane becomes dehydrated, which causes the channels to shrink in size and become less connected, thus lowering the conductivity.[9] For this reason, it is crucial to understand the morphology of the membrane and how it impacts the conductance.

Figure 1.2: Chemical structure of Nafion.

B. Morphology of Nafion

Nafion's ability to conduct protons from the anode to the cathode requires that channels connect from one side to the other. It is well-established that proton conduction occurs predominantly by the Grotthuss "hopping" mechanism in which excess protons are passed along by a series of hydrogen bonds.[9] However, other transport mechanisms such as surface-site hopping[10,11] and diffusion[12] are also involved. With either mechanism, a favorable

morphology for conduction is critical. It has been heavily debated how the hydrophilic domains are arranged to support long-range charge transport. The primary technique to characterize Nafion's bulk morphology has been small angle x-ray scattering (SAXS). In SAXS, a monochromatic x-ray beam hits the sample at a small incident angle, and the scattered x-rays are detected. According to Bragg's law, the angle of the incident beam (0.1-10°) is inversely related to the distance between two scattering objects (1-100 nm). In crystalline periodic materials, the scattering profile consists of sharp well-defined peaks providing precise information on the lattice spacing and structure. However, in random statistical copolymers like Nafion, interpretations of the morphology from the scattering profile is difficult - consisting only of a power law dependence and a broad ionomer peak. Interpretations are further complicated by differences in membrane water content.

Several models have been proposed to describe the membrane morphology and conductance that are consistent with the x-ray scattering data, but the accuracy of these models is limited due to the lack of experimental data on the relevant length scale.[13–17] The simplest structural model is the cluster model in which charge can percolate from different sites.[15] Although the percolation model supports conductivity measurements,[16] this model ignores large scattering lengths and is limited to low water content.[18] The parallel water cylinders model proposed by Schmidt-Rohr and Chen argues that the low angle scattering features are due to aqueous domains arranged as cylinders.[19] This model, however, relies on numerical Fourier transform methods and an assumed image of real space is required. Furthermore, this model does not account for structural reorganization with increased hydration. The bicontinuous network model derived from Maximum Entropy (MaxEnt) reconstructions of the scattering data, which suggests a random network of hydrophobic and

hydrophilic components, does not require *a priori* assumptions of the morphology.[17] This

model, however, does not predict the existence of fluorocarbon crystallites; a primary

scattering feature in the parallel cylinder model. In order to achieve a more detailed

understanding of how the membrane morphology influences proton conductance more

experimental data is required.

As opposed to SAXS, which provides a picture of the morphology in Fourier space,

microscopy provides a picture in real space. Cryogenic transmission electron microscopy

(TEM) images the 3D morphology of the membrane through 2D projections.[20] Typically,

the membrane is hydrated, stained by a heavy metal, and the morphology is frozen in place

by liquid N_2. However, interpretation of these results are often affected by larger domain

size than that inferred from SAXS as a result of staining.[21] To this end, atomic force

microscopy (AFM) is used to provide detailed information of the surface morphology and

conductive channels while also probing the relevant length scales in PEMs.[22–24]

Tapping mode AFM requires sinusoidally driving the cantilever tip near its resonant

frequency. While the topographic height images are almost featureless, the phase images

provide a chemical map of the hydrophilic and hydrophobic domains, which is resolved by

differences in power dissipation between the tip and sample. This dissipation is measured as

a phase in the deflection signal relative to the drive frequency.[25]

$$P_{tip-sample} = \frac{\frac{1}{2}kA^2\omega}{Q}[\left(\frac{QA_0}{A}\right)Sin\phi - \frac{\omega}{\omega_0}] \tag{1.1}$$

where P is the power dissipation, ϕ is the phase angle, k is the spring constant, A is the

cantilever's oscillation amplitude when the tip is touching the surface (engaged), A_0 is the

free air amplitude (not engaged), Q is the quality factor of the cantilever, ω is the drive

frequency, ω_0 is the resonant frequency of the cantilever. When the amplitude of the

cantilever is 80-90% of the free space amplitude, the net force between the tip and the

Nafion surface becomes attractive ($\phi \geq 90°$). This amplitude regime is known as attractive-

mode. Further decrease in the amplitude results in a repulsive force between the tip and

sample. In repulsive-mode $\phi \leq 90°$. According to Eqn. 1.1, phase angles approaching 90°

maximizes the power dissipation. Therefore, the hydrophilic domains correspond to dark

contrast in attractive-mode while bright contrast in repulsive-mode.
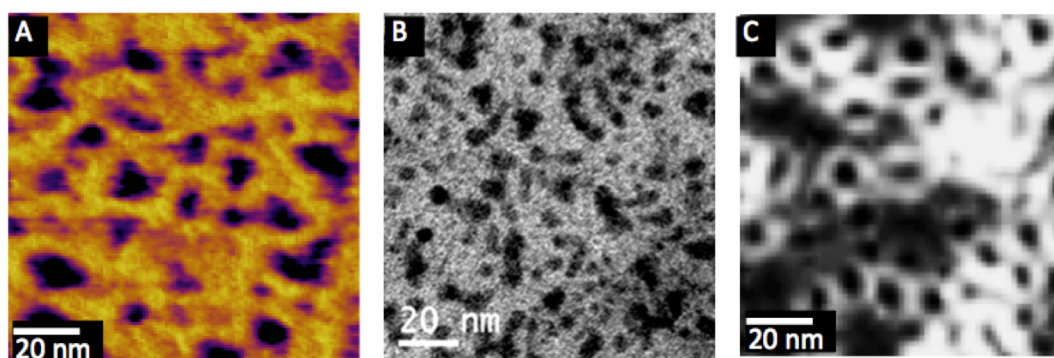
Figure 1.3: (A) 272 nm x 272 nm attractive mode AFM phase of Nafion membrane at ambient RH.[12] Dark regions (~90°) indicate hydrophilic domains and brighter regions (~ 97°) indicate hydrophobic fluorocarbon domains. (B) TEM image of cross section of Nafion stained with silver nanoparticles.[27] (C) MaxEnt reconstructions from Elliot *et. al.*[17] Dark and bright regions correspond to hydrophilic and hydrophobic domains, respectively.

O'Dea *et al.* has compared attractive mode with repulsive mode ($\phi \leq 90°$) noting

smaller domain sizes in attractive-mode that more closely match the domain size in the

bulk.[24] In Fig. 1.3, an attractive-mode phase image is compared with a TEM image and a

MaxEnt reconstruction from SAXS of Nafion at ambient conditions.[17] In all three images,

qualitative similarities can be seen. In 1.3A-C, dark contrast represents the hydrophilic

domains. The average channel diameter of domains from attractive-mode phase was 11 ± 4

nm. While the average diameter from TEM and SAXS reconstructions was 13 ± 2 nm and 6 ± 2 nm, respectively.
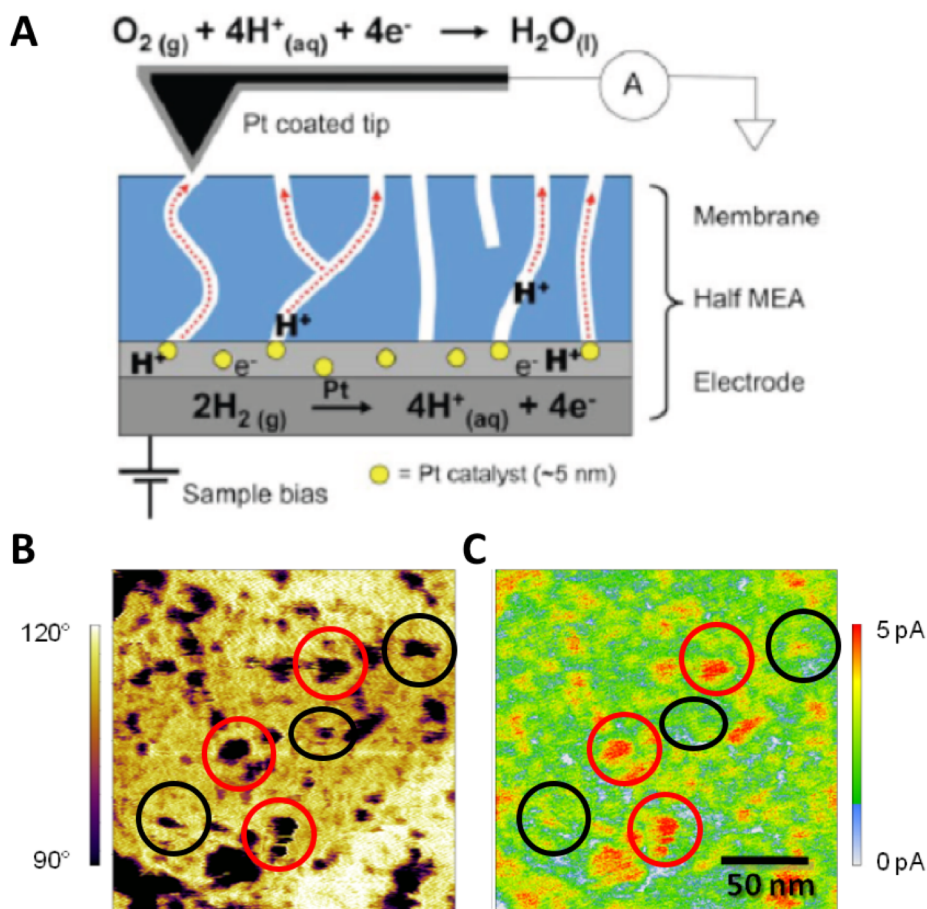
Figure 1.4: (A) Schematic of the cp-AFM experiment showing how current is measured of a Nafion-based half MEA. (B) Attractive-mode phase image of Nafion and (C) cp-AFM current image. The domains highlighted by red circles indicate electrochemically-active channels while black circles indicate un-active channels.

While the phase images map the size and location of hydrophilic channels on the surface, current images from conductive probe AFM (cp-AFM) map which channels produces current.[26,27] Typically, a platinum-coated cantilever is in constant contact with a half membrane electrode assembly (MEA). A schematic illustrating in the experiment is

shown in Fig. 1.4. Hydrogen gas is supplied underneath the sample, while humidified oxygen is supplied over the membrane. The experiments are conducted in a customized closed fluid cell to control the RH. By combining these two techniques, the hydrophilic domains are spatially correlated with regions showing appreciable proton conductance, indicating regions of high electrochemical activity under hydrated and dehydrated conditions.[23,26,28] Attractive-mode phase and current images are shown in 1.4B and 1.4C, respectively. The red highlighted circles indicate the electrochemically-active channels while black circles indicate the un-active channels. Channels that contribute to the electrochemical activity of the cell requires that channels are connected throughout the membrane. However, it is unclear whether channels that provide no current is due to a lack of connectivity or inactive catalyst at the membrane-electrode interface. Hence, more information is needed regarding the connectivity of channels at the membrane surface. It is this question that I address in this thesis.

C. AEM Fuel Cells and Current Challenges

Anion exchange membrane (AEM) fuel cells (AEMFCs) have attracted recent interest because alkaline conditions offer a less corrosive environment and improved ORR kinetics compared to acidic conditions.[29–31] This allows for reduced loading of expensive platinum catalyst or replacement by nickel, silver, or gold.[7]
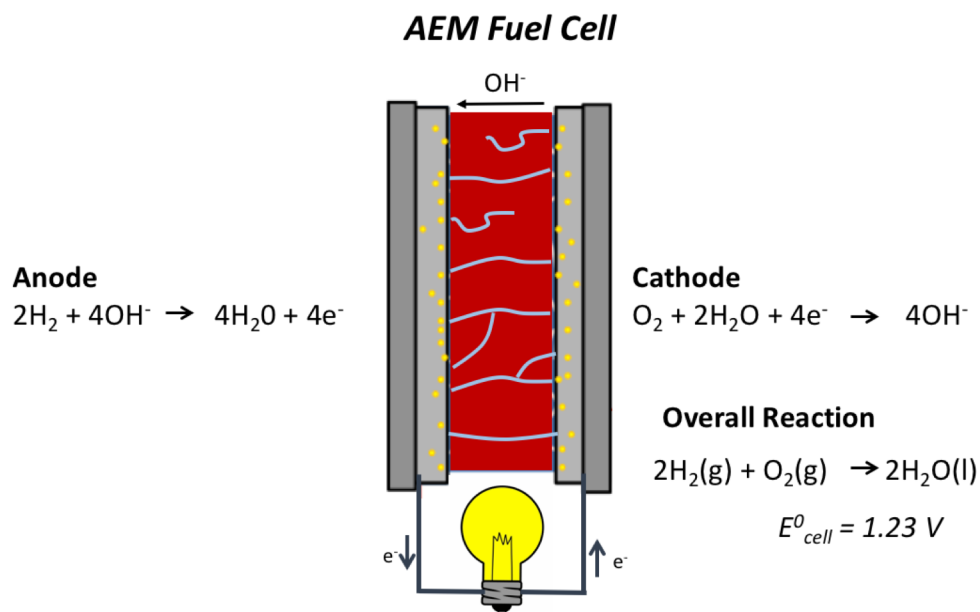
Figure 1.5: Schematic of AEM fuel cell.

AEMFCs and PEMFCs operate very similarly to one another in terms of the fuel used and the electrode components. The key difference between AEMs and PEMs is that AEMs conduct hydroxide from the cathode to the anode. A schematic of an AEM fuel cell (AEMFC) is shown in Fig. 1.5.

Similar to proton conduction, the Grotthuss mechanism is also responsible for the transport of hydroxide. It is important to note that the mechanism involved in hydroxide (OH^-) conduction is similar in both AEMs and PEMs.[9–11,32] While PEMs involve the conduction of an excess proton along adjacent hydrogen bonds, AEMs can be viewed as mirror image in which a proton vacancy, or hole, is transported along hydrogen bonds, with some differences related to the coordination structure of water surrounding the ion.[33] Again, a favorable morphology is critical to hydroxide transport. AEMs typically are random copolymers consisting of a hydrocarbon backbone with a quaternary ammonium side-chain,

which phase separates into hydrophilic and hydrophobic domains on the nanometer scale.[31,34] Therefore, the knowledge and insight gained from studying PEMs like Nafion can be applied toward AEMs.

Low conductivity has posed a roadblock in the development and implementation of AEMFCs. The problem is 3-fold: (1) OH^- is more massive than H^+ and hence less mobile. (2) OH^- can react with atmospheric CO_2, forming heavier HCO_3^- ions.[35] (3) Hydroxyl attack can cause degradation of the backbone and/or the cationic pendant group, which results in reduced ion exchange capacity (IEC).[36,37] In pursuit of higher conductivity and more stable AEMs, the above issues must be addressed in order to achieve a favorable environment for ion transport.[38–41] Chemical degradation of AEMs can be mitigated by implementing quaternary phosphonium (QP) containing polymers.[38,42] The large functional groups provide the necessary steric hindrance to prevent hydroxyl attack and has so far been an important facet of membrane design rationale. At early stage in AEM development, it is imperative that the morphology-conductance properties are well understood to improve hydroxide conductivity and avoid degradation.

D. Overview of Thesis

In this thesis work, we first employ phase-contrast tapping mode and cp-AFM as tools to investigate the nanoscale morphology and proton conductance of a 3M perfluoro-imide acid membrane (625 EW) over a large range of relative humidity (3-95% RH). As a point of comparison, we also investigate 3M PFSA (825 EW) and Nafion. In the phase images, we assess the membrane's water retention and mechanical stability at low and high RH, respectively. Cp-AFM allows us to spatially resolve the hydrophilic and electrochemically

active domains under a similar set of conditions and observe directly the ties between membrane morphology and proton conductance.

We next employ EFM to analyze the structure and frequency of disconnected "dead-end" channels at the Nafion surface. As a tapping-mode AFM based technique, EFM utilizes a Pt-coated tip that probes the electrostatic force gradient based on two-pass interleave scan. In the first pass, the phase image is collected to map the hydrophilic and hydrophobic domains. In the second pass, the tip is lifted off the surface by $20 - 100$ nm and phase deviations of the cantilever are influenced by the electrostatic force gradient, which is attributed to surface charge, dielectric permittivity, and film capacitance. The EFM phase of a single scan area was measured at several voltage biases between the tip and the sample, which allows us to analyze the quadratic behavior of individual channels. Comparing our results to previous models provide an explanation for how variation in channel length leads to heterogeneity in the quadratic fitting parameters.

We next focus on the using cp-AFM to measure the hydroxide conductance through the plane of a well-characterized commercial AEM by FumaTech (Fumapem FAA-3). The manufacturers have not disclosed the chemical structure of FumaTech, but it consists of a poly(phenylene oxide) (PPO) backbone with quaternary ammonium (QA) functionality.[34] The morphology of FAA-3 was observed in the bromide (FAA-3-Br⁻) and hydroxide form (FAA-3-OH⁻) in dehydrated and hydrated conditions. Under dehydrated conditions, both membranes showed no phase contrast indicating the absence of phase-separated hydrophilic domains at the surface. At hydrated conditions, FAA-3-Br⁻ shows randomly dispersed isolated clusters while FAA-3-OH⁻ shows elongated fibrillar structures extending microns in length. Cp-AFM of hydrated FAA-3-OH⁻ revealed elongated regions were insulating

11

suggesting the structure of these regions have a QA-rich interior with a PPO shell. These results provide morphological evidence for the conduction of hydroxide at the surface as a function of hydration level, as well as the effect of excessive swelling by the membrane.

The last chapter focuses on the morphology of QP block copolymer AEMs under hydrated and dehydrated conditions in collaboration with Prof. Coughlin and his graduate student, Yifeng Du in the Department of Polymer Science and Engineering at University of Massachussets, Amherst. Unlike Nafion, block copolymers form well-ordered phases that can be tuned depending on the volume fraction of the ionic block. Our EFM methodology was also applied to study the channel connectivity of two types of QP block copolymer membranes in which one membrane formed cylindrical channels parallel to the surface while the other formed channels perpendicular. From all of the above, these findings will aid the design of future AEMs with improved channel connectivity and chemical stability.

II. Humidity-dependent Surface Morphology and Proton Conduction in Multi-Acid Side Chain Membranes by Conductive-Probe Atomic Force Microscopy

Portions of this chapter are reproduced from:

A. Introduction

Proton exchange membrane fuel cells (PEM-FC's) are a promising power source that is under development for automotive and stationary applications.[43–45] Currently these devices suffer from high system cost and poor durability relative to internal combustion engines, which have impeded commercialization. One route to addressing these factors is to create cells that can operate at higher temperatures (>100 °C). This would mitigate several problems inherent to fuel cells, such as slow oxygen reduction reaction kinetics at the cathode[46] and the propensity for carbon monoxide poisoning to occur at both electrodes.[47] The challenge to accomplishing this goal lies in the PEM itself. These membranes consist of phase-separated polymers with a hydrophilic proton-conducting phase inside of a hydrophobic polymer matrix. The most well-known membrane is Nafion™, a perfluorosulfonic acid (PFSA) membrane. While Nafion™ shows good performance, it has

several drawbacks particularly at high temperature operation. At high temperatures (low RH), water is lost from the hydrophilic phase and proton conductance from anode to cathode drastically decreases.[48] Additionally, high temperatures put Nafion close to its glass transition temperature (~110 °C) which causes a loss of mechanical strength.[49,50]

Water retention and proton conductance can be increased by using lower equivalent weight (EW) membranes, but this in turn reduces size of the crystalline domains of the fluorocarbon backbone, which decreases the mechanical strength of the membrane. Excessive swelling at very low EW can cause dimensional stress leading to accelerated degradation of the membrane electrode interface.[48,51,52] Recent efforts have focused on improving the mechanical strength of low EW membranes through organic/inorganic composite membranes,[53,54] crosslinked ionomers,[55–58] and porous polymer supported ionomers,[57,59] with the latter becoming increasingly popular for fuel cell applications. However, despite the ability to create mechanically robust materials, proton conductance is still lower than in an unsupported material,[58] which necessitates the synthesis of new ionomers with higher proton conductivity.

3M Energy Components Program has developed a new approach to this problem where a PFSA precursor is imparted with a new sidechain functionality that contains two acidic protons per side-chain instead of one.[60] This allows for a membrane with a higher acid content (lower EW) without sacrificing the crystallinity of the resulting membrane. Hamrock and coworkers have shown that these perfluoro-imide acid (PFIA) membranes yield excellent mechanical stability compared to PFSA membranes of a similar equivalent weight.[60]

14
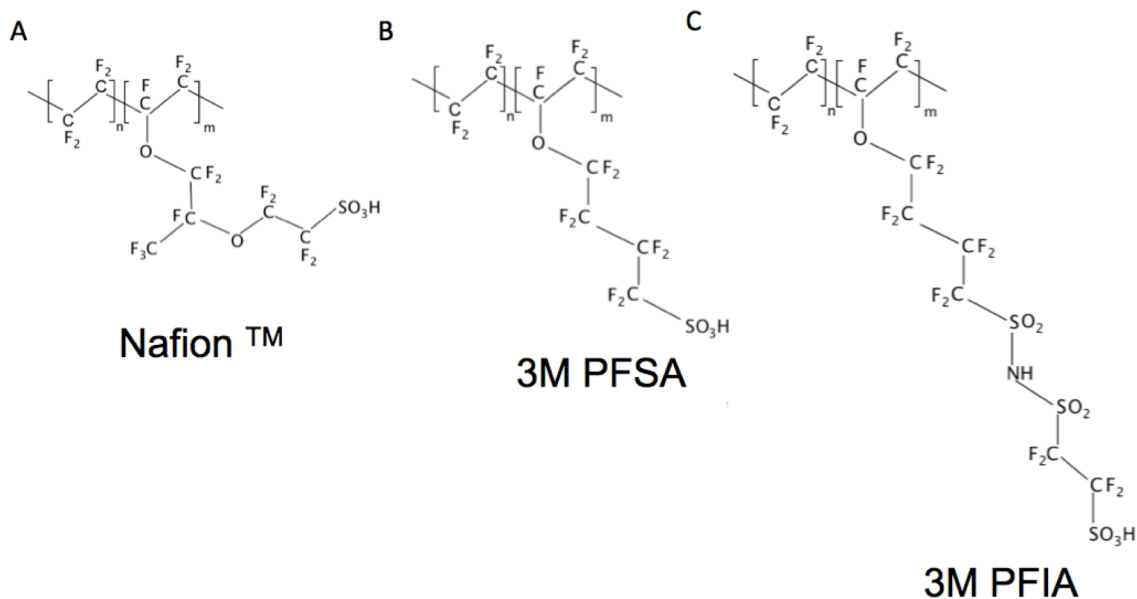
Figure 2.1: Chemical structures of (A) a long side-chain PFSA (Nafion[TM] 212), (B) a 3M PFSA ionomer 825 EW and (C) a 3M PFIA ionomer 625 EW.

Bulk conductivity measurements have already shown that a PFIA membrane has higher proton conductivity than a PFSA membrane made from the same polymer precursor due to an increased concentration of protons. It has also been shown that this leads to increased performance at elevated temperatures.[61] Modeling studies have also suggested a distinct dissociation behavior and hydrogen bond connectivity between the two acid groups.[62] What remains to be understood is how these bulk observations are tied to membrane morphology, swelling behavior, and spatial distribution of proton current coming through the membrane. We have shown previously that the features observed at the surface relate to the bulk structure models inferred from SAXS.[23] At ambient conditions we observe agreement with the parallel cylinder[19] and bi-continuous network models.[63] While at hydrated conditions, we observe features that are in agreement with Rubatat and co-workers' fibrillar model.[13] It

15

also remains to be seen if the membrane morphology is stable across the wide range of water contents that occur during fuel cell operation. Understanding the correlation between the bulk conductance properties and the nanoscale morphology will help to determine to what degree the multi-acid sidechain architecture meets the desired design goals of increased proton conductivity without a loss in mechanical stability under fuel cell operating conditions.

Here we employ tapping mode and conductive probe atomic force microscopy (cp-AFM) as tools to investigate the nanoscale morphology and proton conductivity of a 3M PFIA (625 EW) membrane as a function of relative humidity. Previous AFM work using similar techniques on PEM's has largely focused on Nafion™, with a limited extension to new membrane materials.[23,24,26,64–70] As a point of comparison, we also investigate a PFSA (825 EW) made from an identical polymer precursor (see Fig. 2.1) to directly see the effect of the additional acid group and longer sidechain on the properties of interest. Since it has been shown that there was no observed crystalline backbone for a range of 25-95% RH of the 625 EW PFSA,[71] we used the 825 EW to make this comparison. One advantage, however, is that the side chain spacing of the 825 PFSA is equal to the 625 PFIA, which is an important parameter as Paddison and Elliot have shown that the number of water molecules required to effect proton dissociation decreases when sulfonic acid groups are brought closer to each other.[72]

Because of the large range of relative humidity (RH) that can be present in a fuel cell, we employ a closed fluid cell and investigate morphology over the range 3-95% RH with a specific focus on the extremes of this range. Imaging at extensively dehydrated conditions allows us to assess the membrane's water retention by observing how the size of the

16

hydrophilic domains changes under low RH (3% RH). Conversely at very high RH (95% RH), we evaluate the mechanical stability of the membranes when subjected to various forms of swelling. Cp-AFM spatially resolves the current through the membrane under a similar set of conditions observing the direct ties between membrane morphology and proton conductance. Through this we are able to see evidence of the improved water retention and proton conductance in the PFIA at low RH and elevated temperatures, but at high RH, conditions see evidence of a nearly continuous hydrophilic phase, indicating a high degree of swelling.

B. Experimental

All topography and phase images were acquired simultaneously with an atomic force microscope (Asylum Research MFP-3D-SA). Nafion™ 212 was purchased from Fuel Cells Etc. and all 3M membranes were obtained directly from 3M. Membranes were pretreated by boiling in 0.5 M H_2SO_4 for 1 hour, followed by boiling in de-ionized (DI) water for 1 hour. All membrane samples were mounted on double sided tape on a glass slide for phase imaging. Membranes imaged under dry conditions were then heated in a vacuum oven for 3 days at 80 °C. Membranes under humidified conditions were equilibrated in liquid water at room temperature for 5 days prior to imaging.

Tapping mode images were taken using a standard silicon probe (XSC11, MikroMasch, 2nd lever) with typical resonant frequencies of 140 kHz and spring constants of 5 N/m. A closed fluid cell (modified PolyHeater, Asylum research) was used to achieve varying relative humidity; either dry or humidified nitrogen was supplied at 400mL/minute resulting in a 3% and 95% RH atmosphere in the cell, respectively. Humidity was measured using an external humidity sensor (Honeywell). Membranes were allowed to equilibrate in the cell for

at least 1 hour prior to imaging during which time the humidity of the cell remained constant. Hydrophilic surface area and hydrophilic domain analysis were determined using Igor Pro software by applying a threshold to the sample using the iterative method.[73]

Conductive images were taken using a standard ORCA module with 500MΩ sensitivity using a platinum coated tip (MikroMasch DPER-XSC11) with a nominal spring constant of 0.2 N/m. Images were acquired in contact mode with typical contact forces of ~20 nN. Membrane samples for conductive imaging were hot pressed at 130 °C onto a small patch of a commercial gas diffusion electrode with a Nafion™ post-coating (60% Pt/C, 0.5mg/cm2 Pt, on carbon cloth, FuelCellsEtc.) which served as the anode. Humidified hydrogen was supplied via a gas flow channel under the electrode at 50 mL/minute and humidified air was supplied over the membrane surface at 100 mL/minute while scanning. Using a humidity sensor, we found that the humidity in the chamber was 80% at room temperature and decayed to ~3% at 160 °C. For experiments using dry gas feeds, both flow channels were passed through a dessicator column yielding a relative humidity of 6% at room temperature. At each temperature interval, the sample was allowed to equilibrate with the atmosphere for 30 minutes prior to imaging which was observed to coincide with stable RH values. A positive bias of 1 V was applied to the sample for all images and data reported here, but a linear relationship between current and bias voltage was observed at positive bias.

C. Results and Discussion

Our first goal was to evaluate the morphology of the 3M PFIA ionomer compared to its PFSA counterpart. Since both polymer membranes are made from the same sulfonyl fluoride precursor, one important question to answer is whether the additional acid group on the PFIA has a significant effect on the resulting membrane morphology.   For this we employed tapping mode AFM imaging under a wide range of relative humidity as we have used previously to characterize other PFSA polymers.[23,24,26,74] At ambient conditions
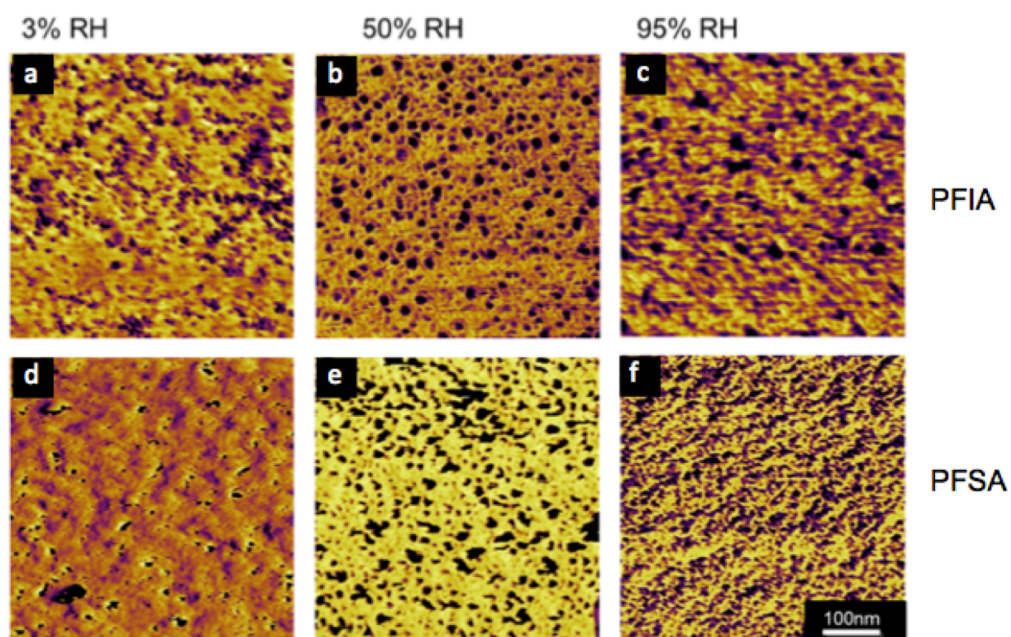
Figure 2.2: (a-f) Attractive mode phase images (z scale range of 99-90º) of a 625 EW PFIA membrane (a-c) and 825 EW PFSA under dehydrated 3% RH (a,d), ambient 50% RH (b,e), and hydrated conditions 95% RH (c,f). Dark regions correspond to the hydrophilic domains where the brighter regions correspond to the hydrophobic domains.

we already notice both polymers showing slightly different morphology seen in Figure 2.2.

Both polymers show a similar degree of phase contrast, implying similar mechanical

properties of both the hydrophilic and hydrophobic domains. We see a well-defined

hydrophilic pore structure in both polymers with each showing a similar fraction of

hydrophilic surface area – 22% for the PFIA and 21% for the PFSA. This is an interesting

result as the slightly lower equivalent weight and higher water uptake observed in the PFIA

polymer might be expected to confer a higher hydrophilic surface area, but they are almost

identical. Despite having a similar amount of hydrophilic surface area, we notice a

significant difference in the size of individual hydrophilic domains. Analysis of phase

images of Figure 2.2 showed that the average radius for hydrophilic domains in the PFIA

membrane was 8.2 nm versus 7.7 nm for the PFSA. Structural models of PEMs including

the cluster network model and parallel cylinder model both predict that cluster size should

increase as equivalent weight decreases, which is consistent with our experimental

data.[19,75,76] In addition to domain size, we also measured the density of domains, which is

quantified by number of domains per square micron. The domain density is an important

metric in addition to domain size as they are both related to the correlation length inferred

from SAXS. Under ambient conditions, the PFIA has roughly twice the domain density

(1276 domains per square micron) as the PFSA (697 domains per square micron).

Approximating the domains as circles the average interspacing between domain centers is

22.3 nm for PFIA and 30.2 nm for PFSA.

Our results are also consistent with previous work by our group on other, higher EW

PFSA's, which both showed smaller average domain sizes.[23,74] It is worth noting, however,

that the domain size nor interspacing in AFM is not correlated with information inferred

from X-ray scattering. The domains we observe on the surface (10-15 nm in diameter) are

larger than those observed in bulk (3-4 nm). This has been explained by various models by

the coalescence of individual clusters to form a larger hydrophilic phase, and by a slightly different morphology at the membrane surface than in the bulk material.[63,77]

Since the PFIA is designed to perform under low relative humidity and high temperature, we next evaluated the water retention ability of the PFIA polymer by conducting imaging under heavily dehydrated conditions and comparing to the PFSA membrane. Water uptake, which is often measured through changes in the mass of the membrane by varying the RH at constant temperature, allows evaluation of the membrane's water retention relative to control PFSAs such as Nafion. Here, rather than measuring the change in mass, we measure the coverage of hydrophilic domains on the surface by measuring the area percent, average domain size, and domain frequency. Hamrock and co-workers have shown that the water content, defined as [mol H_2O]/[mol SO_3^-], of the 625 multi-acid PFIA is similar to the 825 PFSA across a range of 20-80% RH. However, at 80-95% RH, they showed the PFIA swells more than the PFSA.[61] We were interested in comparing our AFM techniques to the results of these materials.

Our previous experience with PFSA polymers has shown that imaging under these conditions requires moving from the attractive imaging regime (phase > 90) to the repulsive imaging regime (phase < 90) in order to observe phase contrast between hydrophilic and hydrophobic domains without coupling strongly to topography. This is likely related to the fact that in attractive mode, only the first atomic layer is being probed mechanically, whereas in repulsive mode the probe depth increases to a few nm.[24,78] In short this implies that other PFSA's such as Nafion™ have essentially no water at the surface and that the phase contrast we see is due to water in subsurface domains in the first few nanometers. This is consistent with work by Kreuer which suggests a fluorine-rich skin on the surface of

Nafion™ at low water contents,[79] and work by Weber and co-workers which shows directly that at low water contents the hydrophilic phase in Nafion consists of isolated spherical clusters.[80] In the case of both the 3M PFSA and PFIA, however, we were able to achieve stable attractive mode phase imaging under dehydrated conditions. This implies that both membranes exhibit better surface water retention, and could indicate that the random network morphology of the hydrophilic phase is more stable to dehydration than was observed in other membranes.[24,74] At dehydrated conditions, the PFIA still exhibits 9% hydrophilic surface area under attractive conditions, whereas the PFSA exhibits 3.9% hydrophilic surface area. The average domain size in the PFSA decreases considerably to 3.7 nm radius, while the PFIA undergoes less of a decrease to 6.7nm. The occurrence of domains in the PFSA is also markedly lower than the PFIA at 195 domains per square micron versus 390. We attribute these results to better surface water retention and a hydrophilic phase which is stable under dehydrated conditions, this effect was most pronounced in the PFIA but seen in both polymers. (Figures 2.2a and 2.2b).

One advantage of the PFIA polymer is that despite being able to effectively retain water, it should exhibit sufficient crystallinity due to polymer backbone packing so that it does not swell excessively at high water contents. This enables the use of lower EW PFIA polymers while maintaining sufficient mechanical strength. Hamrock and coworkers have already shown that these polymers exhibit higher crystallinity than a PFSA of equal equivalent weight.[61] In order to evaluate performance at high water contents, we equilibrated both membranes in water and imaged them in a high (95%) RH atmosphere. In both cases, we see an increase in hydrophilic surface area, consistent with a dilation of ionic clusters. Previous SAXS experiments on 3M PFSA polymers and other PFSA membranes have

shown that the size of ionic clusters increases, or decrease in the structural correlation

length, with increasing water content, as is the case for many phase separated systems.[71,75,76]

By AFM, we notice an increase in hydrophilic surface area in the PFIA to 36% and

in the PFSA to 33%. Particle analysis shows that the average size of hydrophilic domains

greatly increases. The PFIA increases to 13.6 nm in diameter while the PFSA increases to

14.1 nm. Furthermore, because the domains are increasing in size through coalescence, the

domain density of the PFIA (739 domains per square micron) drastically decreases while the

PFSA (1194 domains per square micron) continues to increase in domain density with

increasing RH, implying better domain dispersity with increased water uptake. This is in

agreement with what has been previously shown with water sorption isotherm measurements

(T = 80 °C) indicating PFIA with a hydration number of 21 mol H_20/mol SO_3^- swells more

than PFSA, a hydration number of 16 mol H_20/mol SO_3^-.[61] We also see a movement towards

a near-continuous hydrophilic phase at the surface, which is more pronounced in the PFIA,

in contrast to the isolated hydrophilic domains at ambient and dehydrated conditions.

While this continuous hydrophilic phase has the potential to cause problems at the

interface. Swelling induced mechanical strain or water accumulation inside the electrodes

can cause the membrane to delaminate from the surface,[81,82] but can be remediated through

use of reformulating inks in the catalyst layer.[83] It appears that while the PFIA retains

similar mechanical properties to the corresponding PFSA, the additional acid group causes a

small degree of additional swelling.

We have already shown that qualitatively, both membranes follow a similar change

in morphology but with a quantitative difference in hydrophilic surface area.[23,24,74] To more

directly visualize the proton conductance of these membranes under fuel cell operating conditions, we employed conductive probe AFM as described in our previous work. At room temperature and 80% RH we noticed a substantially higher current in the PFIA as compared to the PFSA, likely due to the increased concentration of protons in the membrane. We also noticed the formation of large, non-conductive fibrils features in both membranes, similar to those observed in Nafion™ 212. This is likely caused by the sample construction method where samples are hot-pressed at 130 °C, close to their glass transition temperature, which leads to structural rearrangement. As can be seen in Figure 2.4, these features are non-conductive indicating that they do not contribute to through-plane conductivity and thus fuel cell performance.

In order to evaluate the performance of these polymers at the designed operating conditions, we conducted cp-AFM imaging at elevated temperature and reduced humidity. Figure 2.3 shows a schematic of our closed flow cell. The ½ MEA is hot-pressed to a steel puck, which is then screwed into the cell. The puck has two holes in the middle to allow for H_2 to reach underneath the sample. In our current measurements of PFSA membranes, humidified air was supplied over the top of the surface of the membrane. A bias wire connects from the conductive cantilever to the sample to complete the circuit and measure current. Figure 2.3B shows a disassembled cell that shows how the ½ MEA is mounted onto the stage. Figure 2.3C shows the chip holder used for conductive imaging (ORCA holder) and how the chip holder is screwed onto the imaging cell as it is important to create a tight seal to maintain constant RH and temperature.
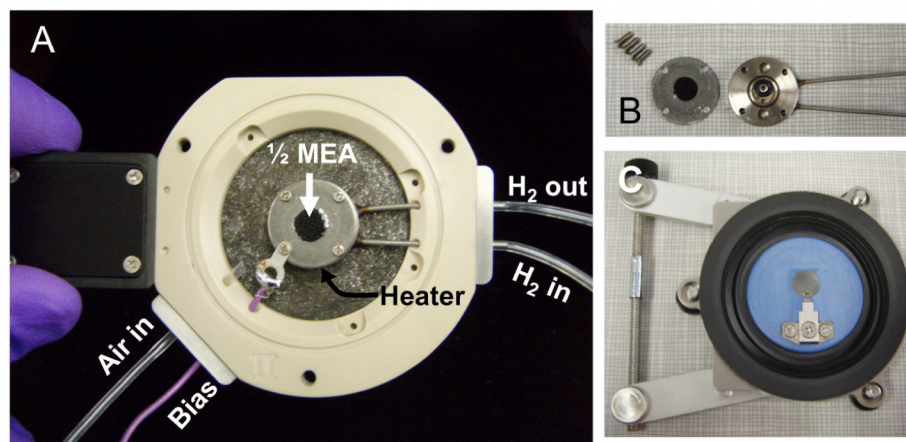
Figure 2.3: (A) Fully assembled flow cell with ½ MEA loaded into the heating cell (beige) used for measuring current at the surface of PEMs and AEMs. The heating element is located below the stage. (B) Fully disassembled flow cell showing how the ½ MEA is mounted onto the cell. (C) Cp-AFM chip holder (ORCA holder) with gasket, which is secured to the heating stage with 3 screws. This creates a sealed environment to control the RH and temperature.

We could not find a practical way to increase the temperature of our gas streams without introducing substantial electrical noise into the cp-AFM measurements. For this reason, we used room temperature gas feeds and raised the temperature of the fluid cell, which increased temperature and simultaneously decreased relative humidity. We found that at the flow rates used in this study, we achieved a relative humidity of 80% at 25 °C which decays to ~25% at 100 °C. Figure 2.4 shows the relationship between temperature and relative humidity at the conditions used in this study.
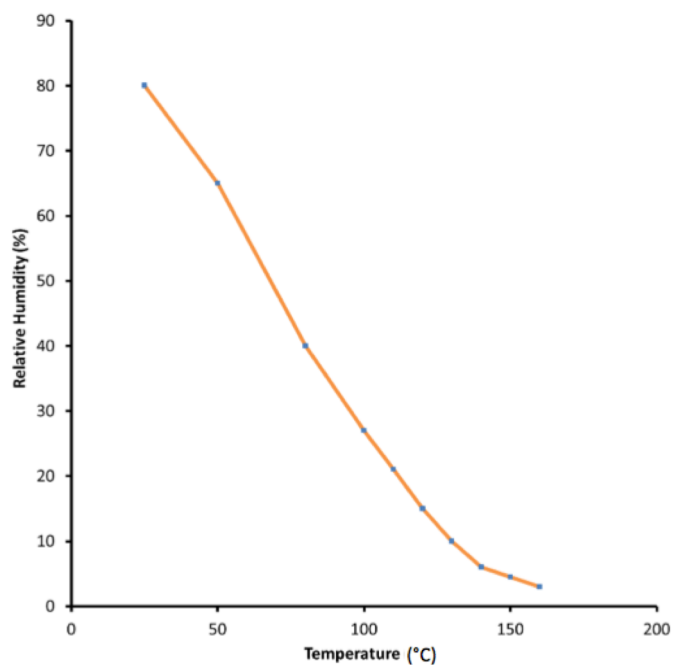
Figure 2.4: Relative humidity versus temperature relationship for our sample chamber with membrane sample and flow rates of 50 mL per minute humidified H_2 (g) and 100 mL per minute humidified N_2(g) at anode and cathode respectively.

Not surprisingly, in this temperature range, both membranes lost conductivity quickly as temperature was raised and did so at a rate consistent with bulk ionic conductivity observed in previous measurements by the 3M group.[61] Above 100 °C, the decrease in conductivity was more rapid likely due to additional evaporation of the surface from being above the boiling point of water.

Figure 2.5 below shows spatially resolved current images for each membrane at 25, 100 and 140 °C. The bright red regions indicate proton current through the membrane to the cantilever tip indicative of the hydrophilic and electrochemically active domains. The green and blue regions indicate little to no proton current indicative of the hydrophilic regions. The

26

images qualitatively show that as temperature is increased, the proton current gradually decays in both membrane systems. We observed that the PFIA maintained a small amount of proton current up to 160 °C whereas the PFSA we observed no current above 130 °C. This result appears to be in line with our previous observations about the more hydrophilic character of the PFIA surface, and suggests that the bulk hydrophilic phase may retain a higher degree of connectivity between hydrophilic clusters.
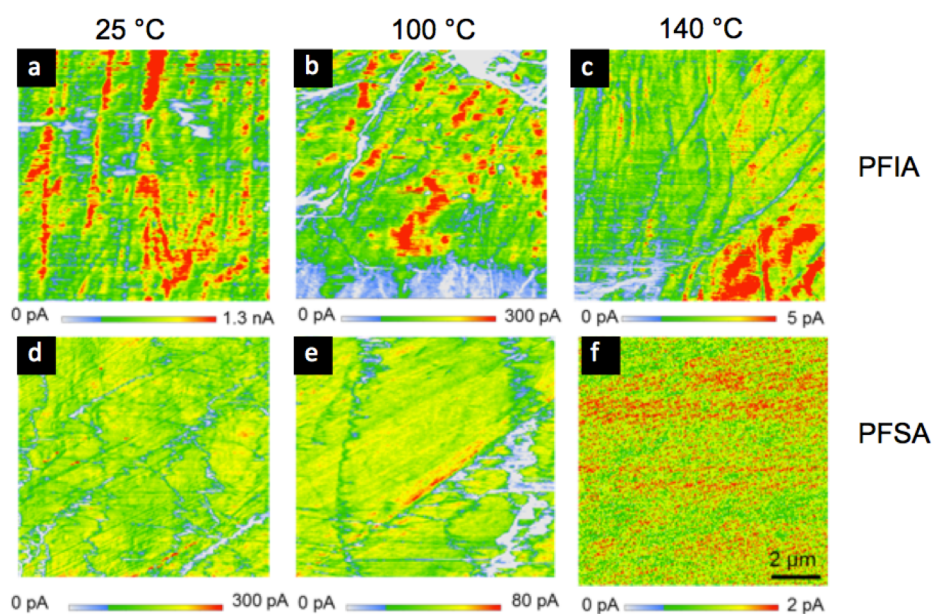
Figure 2.5: Cp-AFM current images of PFIA (a-c) and PFSA (d-f) at 25 °C (a,d) 100 °C (b,e) and 140 °C (c,f). The red from the color map indicates strongest current showing proton flow through the membrane to the tip. Green indicates low current and light blue indicates zero current.

As is readily apparent, the PFIA shows higher current values across all of the conditions explored in this study. This is not surprising, as the lower equivalent weight is expected to yield a higher density of proton charge carriers and thus a higher proton conductivity. Interestingly, the PFIA shows much broader current distributions as well. This

often was manifested as "hot spots" in the current images, which were in the hundreds of nanometers to micron size range, and was most pronounced at high relative humidity. A possible interpretation of these results is that there is a distinct morphology causing a non-uniform concentration of sulfonic acid groups near the surface. Figure 2.6 shows an illustration of our cp-AFM data. At dry and ambient conditions, a random distribution of hydrophilic clusters was observed in the phase images. At hydrated conditions, we observed non-conductive fibrils at the surface, suggesting significant structural rearrangement at the surface.
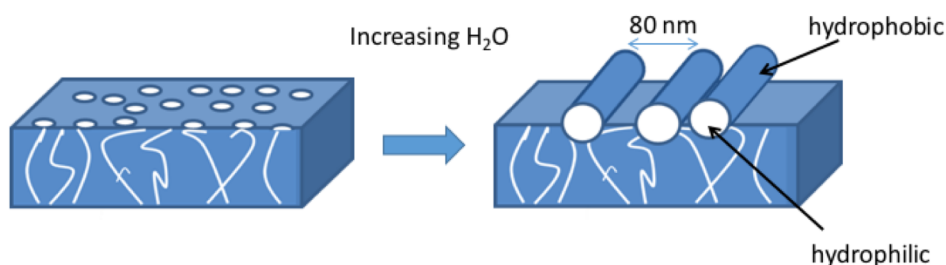
Figure 2.6: Cartoon illustrating the change in morphology between dry conditions and hydrated conditions of a PFSA or PFIA membrane supported by our AFM data.

Figure 2.7 shows a series of histograms displaying the average currents from a 20 x 20 um conductive AFM image at a range of temperature and RH conditions. Figure 2.8 shows a plot of the log of average current in these experiments versus RH at each temperature and shows how each of the membranes has a near linear decrease in current in the $80 - 20\%$ RH range and then a more drastic decrease in current at very low relative humidity. The lower humidity range also corresponds to areas above the boiling point of water, thus it is likely that under these conditions loss of water from the membrane surface is

a large factor, even if some water is maintained in the bulk. As can be seen in figure 2.7 and 2.8d, both the PFSA and PFIA show substantially higher average currents than Nafion™ 212 and all membranes showed an exponential decay in average current as a function of decreasing RH ($R^2 > 0.93$). By carefully monitoring the relative humidity inside of the sample chamber at each temperature value, we were able to accurately relate each temperature to a relative humidity.
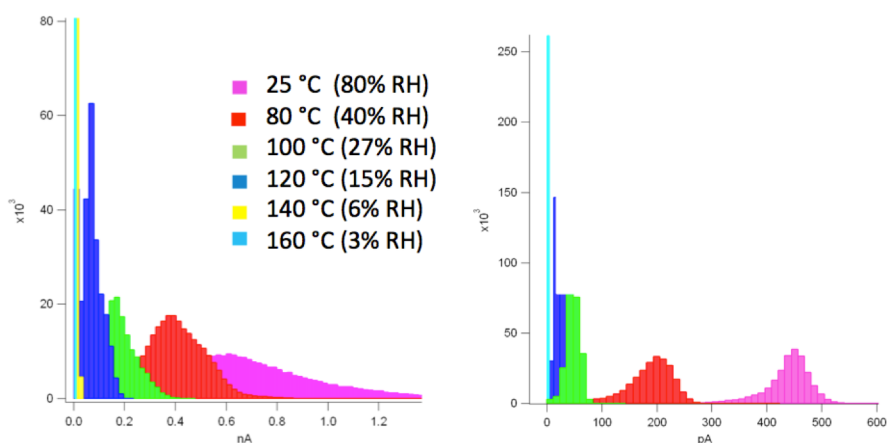
Figure 2.7: Current histograms at various temperatures for 625 EW 3M PFIA (left) and 825 EW PFSA (right). From Figure 2.3, RH decreases linearly with increase in temperature. Broad current distributions were observed at low temperature and high RH, while narrow distributions were observed at high temperature (>100 °C). Larger currents were measured for PFIA over the PFSA at similar EW.

It has been found in previous studies on Nafion™ that despite a theoretical increase in proton conductance at elevated temperatures,[84,85] values at different temperatures but constant RH showed very little change.[81] For this reason we assumed that temperature was

not a factor in these experiments in order to plot our data as a function of relative humidity. Additionally, the PFIA was able to reach higher temperatures and maintain measurable proton conductance. Looking at the normalized proton current we can see that in the extremely low RH and high temperature regime, both membranes lose a similar percentage of proton current. The largest differences occurred at 100 °C and 120 °C (15% and 27% RH) where the PFIA shows about double the normalized proton current implying the biggest improvement in performance in this temperature regime. This is generally regarded as a target range for higher temperature PEMFC's.
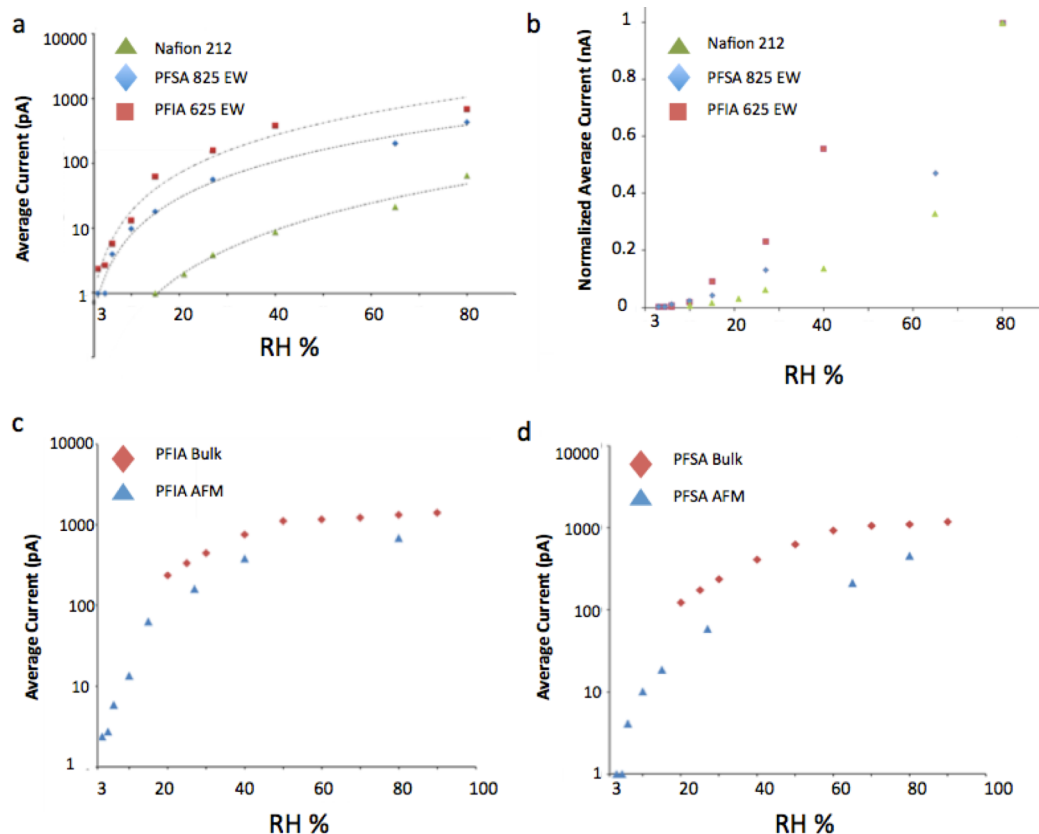
Figure 2.8: Average current values versus RH (a,c,d) for PFIA, PFSA, and Nafion 212 membranes on a log-linear scale. Normalized average current vs. RH (b) shows the current expressed as a fraction of the maximum current at 80% RH on a linear scale. Logarithmic fits for each series are shown as a dashed line in (a). Comparison between AFM and bulk conductivity data for 3M PFIA (c) and 3M PFSA (d).

If we compare our AFM conductivity values to those acquired by Schaberg *et al.* during bulk conductivity measurements, we see good quantitative agreement.[60] This is impressive given the differences in the techniques being employed, bulk measurements are made in the in-plane direction using a high frequency AC bias, while our AFM measurements are conducted in the through-plane direction under a constant DC bias. Figure 2.8b shows a plot of our conductive AFM data alongside theoretical currents based on bulk conductivity values and assuming a fixed tip-sample contact area (20 nm radius half-sphere)

and fixed membrane thickness for the PFIA and PFSA polymers. For example, the PFIA showed a conductivity of 120 mS/cm at 80% RH. If we apply our assumptions and assume no interfacial resistance or kinetic limitations, we get a theoretical value of 1.14 nA/V. The current we actually measure under these conditions is 704 pA/V, about 30% lower, but a very good estimate given the lack of information on the actual tip/sample contact area. At lower relative humidity, we see that the through plane conductivity is decreasing more rapidly than the in plane conductivity likely due to increased dehydration directly at the surface and a decreased electrochemical contact area with the AFM tip.

We conducted a similar set of experiments using dry gas feeds, where temperature was varied and humidity remained essentially constant (6% RH at 25 °C and 3% RH at 150 °C). Under these conditions we notice a linear decrease in current as temperature is increased, due to increased evaporation at high temperatures. These measurements highlight an important consideration when interpreting bulk conductivity measurements of ionomer materials. During fuel cell operation, the surface properties of the membrane ultimately dictate through-plane conductivity and the performance of the fuel cell and need to be considered when evaluating these materials.

D. Conclusions

In summary, we have investigated two of 3M's perfluorinated ionomers that are designed specifically for PEM fuel cells operating under high temperature and low relative humidity. We show that both membranes have impressive water retention capability at low relative humidity, and that the PFIA is especially well suited for these conditions. At high

32

RH we see a large amount of hydrophilic surface area in both, and the formation of a continuous hydrophilic phase in the PFIA which likely indicates unfavorable swelling. Using conductive imaging we measured the through plane proton current at conditions closely resembling the operating conditions for these cells. We saw that the PFIA membrane shows higher currents and broader current distributions across all temperature and humidity. Comparison to bulk proton conductivity yields fairly good quantitative agreement at high relative humidity, but poorer agreement at low humidity due to a reduced electrochemical contact between the AFM tip and membrane surface. These measurements are useful because they allow us to visualize the effect of operating conditions on through membrane current under a steady DC bias, which closely mimics fuel cell operation. The changing contact area of the tip also allows a quantification of surface contributions to overall resistance when compared to bulk conductivity values. Further optimization of this technique will allow for the effective evaluation of other high temperature membrane materials. Of particular interest is the investigation of porous polymer supported membranes, which represent a growing portion of fuel cell systems. The ongoing analysis of the morphology and spatially resolved proton conductivity of these materials under operating conditions will aid in the design of new, higher performing systems.

III. Imaging Channel Connectivity in Nafion by Electrostatic Force Microscopy (EFM)

A. Introduction

Understanding charge transport within polymer electrolyte membranes requires detailed understanding of the membrane morphology and channel connectivity on the nanometer scale; the size of an individual channel. This chapter focuses on adapting long-established electrostatic force microscopy (EFM) methods to study the channel structure and length in Nafion.

Previously established AFM techniques such as conductive probe AFM (cp-AFM) provides direct insight into channel connectivity.[83] While the current image is acquired in contact mode and the phase image is acquired in tapping mode, correlations between the images indicate which of the hydrophilic channels results in electrochemical current.[26,28,74,86] These experiments not only show relative conductance of individual channels consistent with the model of Schmidt-Rohr and Chen,[26] but also shows the existence of hydrophilic surface domains that do not support proton conductance or produce electrochemical current. We have denoted these hydrophilic domains as dead-end channels that do not connect one side of the membrane to the other. Since these dead-end channels do not produce

electrochemical current, cp-AFM does not report on the structure of these domains. In addition, cp-AFM usually requires imaging under hydrated conditions and becomes challenging under dry conditions.[14]

Electrostatic force microscopy (EFM) is a tapping mode technique that offers improved resolution over cp-AFM.[23] EFM has been established for decades and have been used to investigate the surface charge characteristics of both isolated nanostructures[87] and structures embedded in an insulating thin film.[88–90] EFM has been used for acquiring local impedance spectra of Nafion.[91] EFM is influenced by tip-sample geometry, surface charge, and dielectric properties. Hence, we can infer how differences in the surface charge and dielectric properties are influenced by differences in channel size and shape. An additional advantage of EFM is that a phase image can be acquired in the first pass while a capacitive force image can be acquired over the exact same image area in an inter-leaved scanning fashion. By varying the DC bias between the tip and sample, charge migration can be observed and directly correlated in XY with the attractive mode phase image.

We discuss the use of EFM to map the charge distribution of the Nafion membrane surface on a nanometer scale and to provide insight into the connectivity of individual channels. To our knowledge, no one has used this imaging method to characterize the connectivity of the hydrophilic channels of Nafion. Our results show a variation in the measured surface charge in the hydrophilic domains which are attributed to differences in channel conductivity. Using our EFM image data we are able to develop a model for the hydrophilic domains based on three categories; connected channels, branched channels and dead-end channels. The morphological domains we propose are consistent with the parallel water cylinders model proposed by Schmidt-Rohr and Chen.[92,93]

35

B. Experimental

1. Sample Preparation

For the data discussed in this chapter, conductive substrates consisted of single-sided copper tape on a glass coverslip. The copper was cleaned by rinsing with deionized (DI) water for 1 minute followed by rinsing in isopropyl alcohol (IPA) for 1 minute. Thin films of Nafion were deposited on the copper by dipping the coverslip halfway into a 50 mL beaker of 5% Nafion: IPA solution. The films were left to dry in a sealed container at ambient conditions (30-50% RH) for 3 days. The thickness of the films was measured to be 100-300 nm using AFM topography across the edge of the film. For EFM experiments in later chapters, fluorine-doped tin oxide (FTO) substrate was used since copper could potentially dissolve at the membrane-substrate interface. However, it is important to note, we found no measurable differences in surface charge variation between FTO and copper substrates.

2. EFM

EFM relies on a two-pass interleaved scan. In the first pass, the tip is maintained in attractive mode, in which tip-surface interactions are influenced by both van der Waal's and electrostatic forces. At this regime, the distance of the cantilever z-position is ~ 5nm away from the point of contact position of the Nafion surface. We define the point of contact position as the point in which the lower turning point of the tip apex makes contact with the surface. This is measured by taking force deflection curves, shown in Figure 3.1.
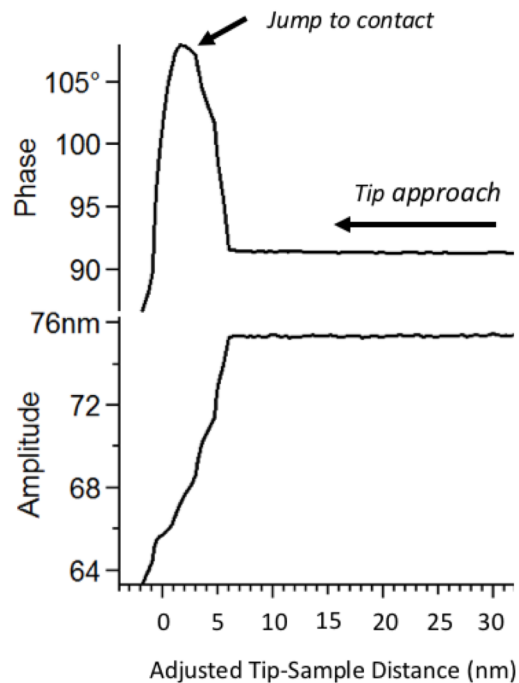
Figure 3.1: Shown is a force-deflection plot in which the tip is in tapping mode, approaches the surface and measures the amplitude and phase as a function of the tip's z position. The point of contact position is labeled. The attractive-mode imaging regime is typically 5 nm above the point of contact, while repulsive-mode is 5 nm below the point of contact.

We map the topography and spatial variation of the hydrophilic domains surrounded by the hydrophobic matrix using the first pass phase images. Scan regions of interest are located by finding flat areas (roughness of 4 nm peak-to-peak) to ensure the attractive interactions of the probe are not corrupted by topography. In the second pass, the tip is lifted from the attractive mode by 100 nm thus corresponding to ~105 nm from the surface. In EFM, a constant DC sample bias is applied to the electrode substrate while the tip is held at ground. We scanned the same region for different voltage biases applied to the substrate from the microscope controller. We applied -1.5V to +1.5V in 0.5V increments.

37

Images were collected using an Asylum Research MFP3D AFM with a conductive Pt-coated tip provided by Micromasch (model HQ:XSC11/Pt) with a resonant frequency of ~325 kHz, spring constant k = 40 N/m, nominal quality factor Q = 424, and tip radius of curvature (< 27 nm). We found higher resonant frequency tips are optimal for attractive-mode phase imaging. We have also shown that while imaging in attractive-mode, the sizes of the domains are not limited by the radius of curvature of the probe.[14] The measurements were done under ambient conditions (30-50% RH) and at room temperature such that the pore morphology would be observed. All the images were acquired using the retrace image scanning top to bottom.

3. Analysis

The images were analyzed in Igor Pro with an MFP3D image analysis plugin. Hydrophilic domains were manually chosen for analysis by inspecting the consistency between the trace and retrace phase images. Throughout analysis the (x,y) position of the domains in the phase image were marked by a cursor which highlights the (x,y) position in the EFM images. Domains that appeared to be influenced by roughness in the height image were neglected. Domains that were influenced by scan direction were also neglected. The sizes of the domains in first pass phase images were analyzed by applying an iterative method image threshold. The EFM phase data was averaged over the spatial location of the domain in the first pass and an uncertainty was also computed. The EFM phase as a function of V_{EFM} (V_{tip} - $V_{substrate}$) was plotted for each domain and was fit to a 3rd order polynomial.

4. Height Artifacts in EFM

The spatial resolution in EFM depends on the radius of curvature of the tip and the lift height. While a lower lift height improves the resolution, the image quality becomes compromised by the occurrence of height artifacts. Height artifacts in EFM occurs when the short-range Van der Waal's forces dominate the cantilever phase shifts over the Coulombic force, which results in an EFM spatial resolution comparable to the first pass height. Examples of height artifacts are highlighted in Fig. 3.2.
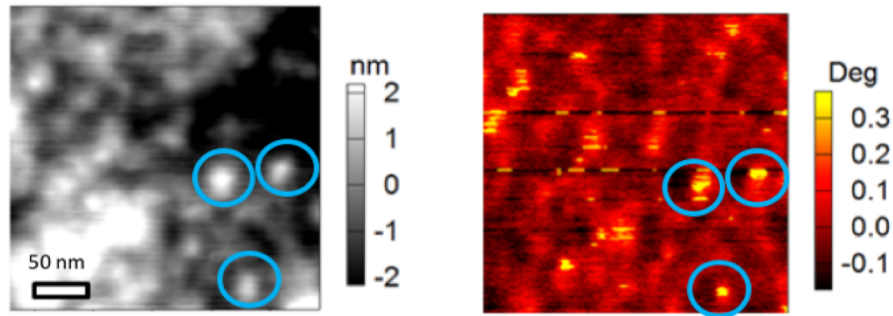
Figure 3.2: Highlighted examples of topographically-induced image artifacts shown in both the height image (left) and the EFM image (right).

Height artifacts were quantitatively identified by calculating the correlation between the height and EFM images. An XY image plot is generated where each pixel is the correlation coefficient, which indicates how well two images are correlated. Thus, regions of positive correlation imply topographically-influenced EFM signals. The correlation is defined by multiplying the normalized height image by the normalized EFM image then taking the absolute value:

$$C(x, y) = |H(x, y) \times E(x, y)| \qquad (3.1)$$
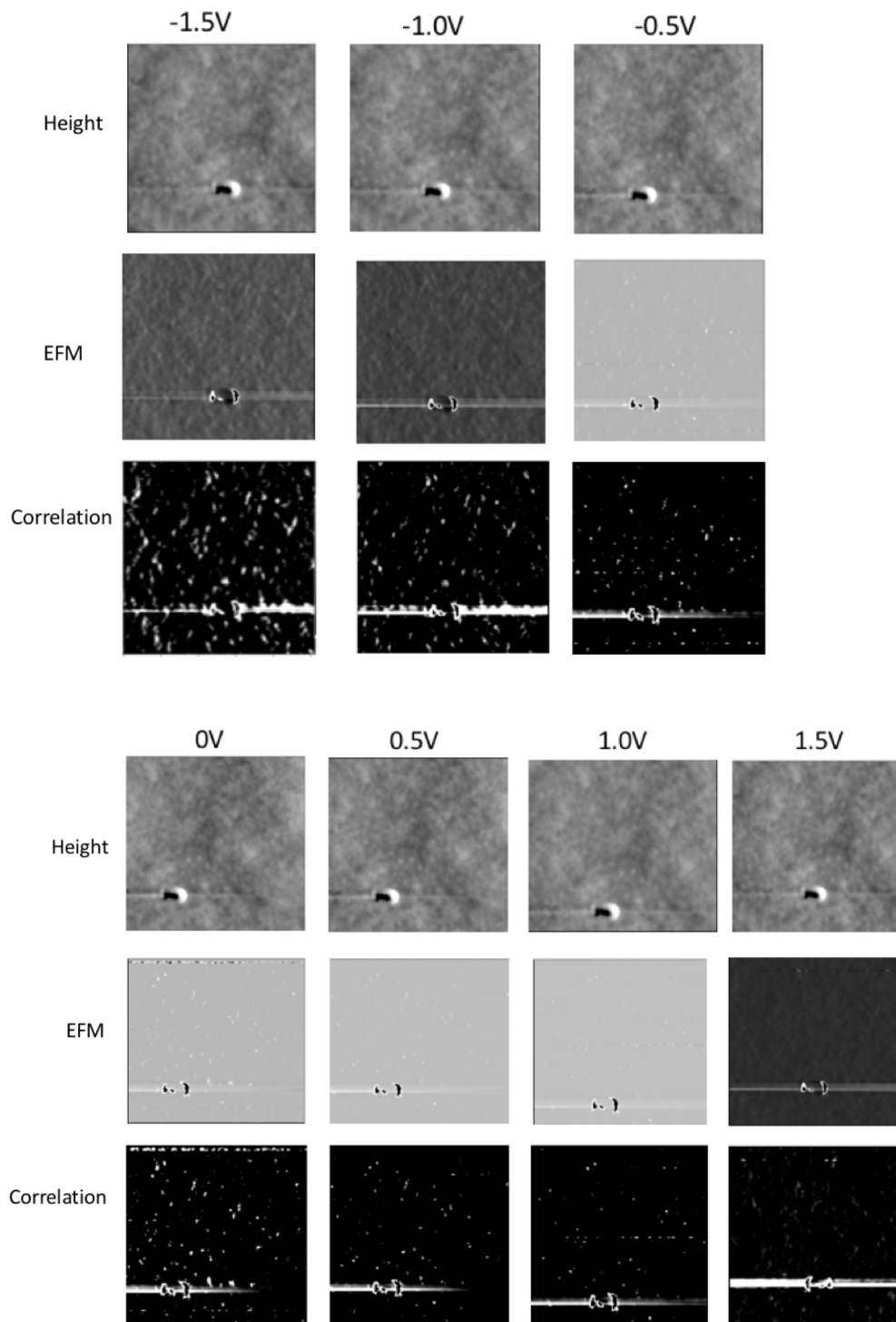
Figure 3.3: 1.6 x 1.6 μm height, EFM, and correlation images for all V$_{sample}$ collected.

The correlation images were generated in ImageJ software. Figure 3.3 shows an entire image-set consisting of height, EFM, and the calculated correlation image. All images were normalized so pixel values range from 0 – 1. We found a stronger correlation for negative sample biases (positive V_{EFM}). Thus, the -1.5V sample bias image was used to identify which hydrophilic domains are not corrupted by the topography. The channels that were analyzed by EFM are highlighted by numbers and yellow circles in the first pass phase image and corresponding correlation image. It is important to note that domains labeled 1, 5, 14, and 15 were deemed to be corrupted by the topography.
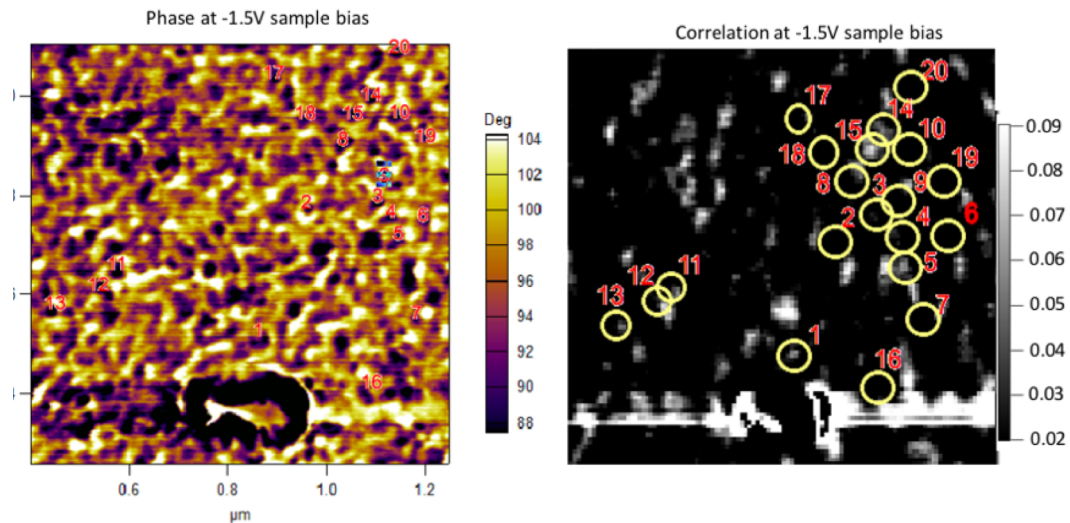
Figure 3.4: Phase image and correlation image at -1.5V sample bias.

C. Theory of EFM

EFM is a two-pass interleaved scan in which the topography and phase is measured in the first pass and the EFM phase is measured in the second pass. An illustration of this method is shown in Fig. 3.5. In the second pass, also known as lift-mode, the tip is lifted off the surface while mechanically driven on the cantilever's resonance frequency with a small (10 mV) drive amplitude. At this lift-height distance (20-100 nm), only the electrostatic force gradient established between the conductive tip and the sample influences the phase deviations of the probe.

1st pass

2nd pass scan (lift-mode)

Lift-height

FTO substrate

FTO substrate
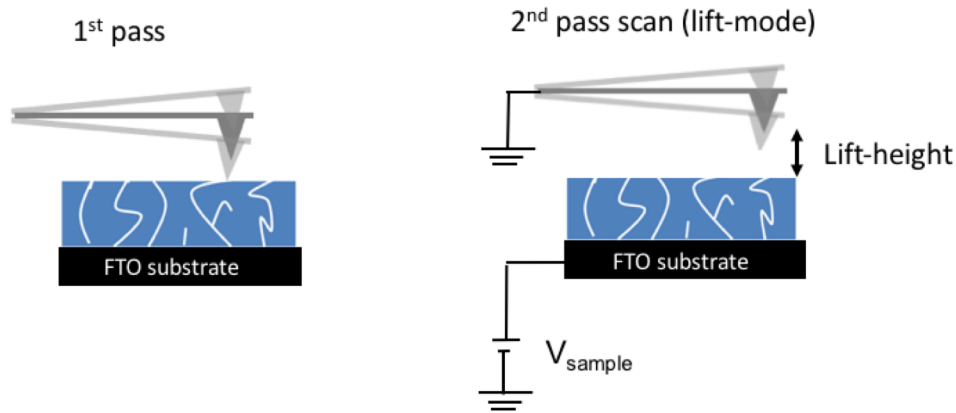
V_{sample}

Figure 3.5: Schematic of the EFM 2-pass method. In the second pass scan in our experiment, the voltage is applied to the sample while the tip is held at ground.

Mathematically, the phase deviations are defined as:

$$\Delta\phi = \frac{Q}{2k}\frac{\partial F}{\partial z}$$ (3.2)

where Q is the quality factor of the cantilever, k is the spring constant, F is the electrostatic force exerted by the sample onto the tip, and z is the direction of the tip oscillation. In general, the work (U) done on a test charge (q) by an electric field is defined as:

$$dU = Vdq$$ (3.3)

42

Since V = q/C where C is the capacitance and V is the potential difference, we can substitute

and integrate Eq. 3.2

$$U = \frac{1}{2}CV^2 \qquad (3.4)$$

Since C is a function of z,

$$F = -\frac{\partial U}{\partial z} = -\frac{1}{2}\frac{\partial C}{\partial z}V^2 \qquad (3.5)$$

Therefore, the expression for the EFM phase shift is:

$$\Delta\phi = -\frac{Q}{2k}\frac{\partial^2 C}{\partial z^2}V^2 \qquad (3.6)$$

According to Eqn. 3.6, the EFM phase shift has a quadratic dependence with respect to the

voltage, which is the total potential difference between the tip and the sample. This consists

of 3 components: (1) the voltage bias controlled by the user, $V_{EFM} = V_{tip} - V_{substrate}$. (2) the

surface potential of the membrane film, V_s. (3) the potential due to charge enclosed in the

membrane, V_q. Accounting for all of these contributions, Eqn. 3.6 becomes[23,24]:

$$\Delta\Phi = -\frac{Q}{2k}\frac{d^2 C}{dz^2}[(V_{EFM} - V_s)^2 - 2(V_{EFM} - V_s)V_q + V_q^2] \qquad (3.7)$$

Eqn. 3.7 shows that the linear term provides information regarding the stored charge

enclosed, from which we can make inferences regarding the channel connectivity.

D. Quadratic EFM Phase Behavior: 3 Classes of Channels

In our EFM experiment, a two-pass scanning method is used; topography is acquired via

tapping-mode phase in the first pass and EFM phase shift is acquired in the second pass. In

the first pass, the Nafion is imaged under attractive mode conditions. The results of EFM

applied to a Nafion film are presented in Figure 3.6. The topography and phase images are

shown in Figs. 3.6A and 3.6B, respectively. Contrast in the first pass tapping-mode phase is

related to the power dissipated by tip-sample interactions.[94] Phase greater than 90° signify

attractive mode and deviations toward 90°, or dark contrast in Fig. 3.6B, signify maximum

power dissipation and are assigned as the hydrophilic domains. As we have discussed in our

previous work, the phase images show a surface morphology consistent with both the

parallel water cylinders[25] and bicontinuous network models[14] predicted from bulk small

angle scattering, but quantitatively distinct in size and density of aqueous domains on the

surface.[17]
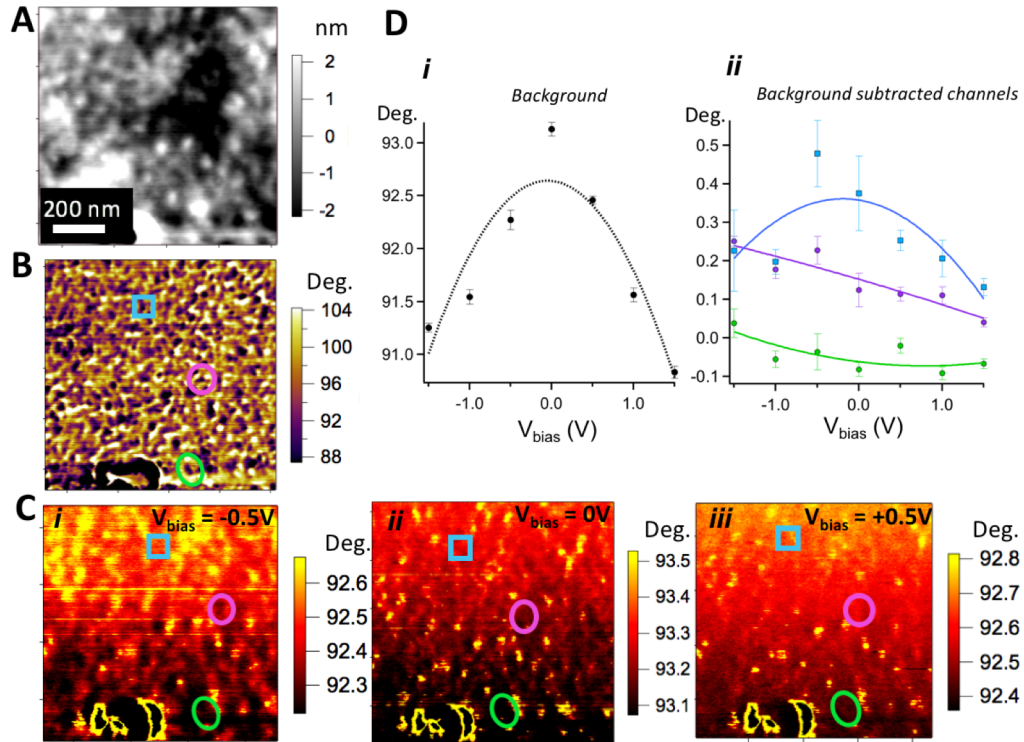
Figure 3.6: AFM images that include the first pass (A) height and (B) attractive mode phase and the second pass EFM phase shifts. The lift height above the surface is 100 nm. (C) i-iii shows EFM phase images at different V_{bias}. (D) i shows phase shift as a function of V_{EFM} for the average background. (D) ii shows the background subtracted phase shift as a function of V_{bias} for three different highlighted domains in B and C. All of the domains were fit to a quadratic function.

In the second pass, the EFM image is acquired. In EFM, the conductive tip is placed at a height of 100 nm above the surface and is mechanically driven at its resonant frequency while a DC bias is applied between the tip and substrate. The topography image acquired in the first pass is used to maintain the 100 nm separation during the second pass. During both passes, a bias is applied to the tip and FTO sample electrode. The bias voltage between the tip and the FTO sample is defined conventionally as $V_{EFM} = (V_{tip} - V_{sample})$. In all of our experiments the voltage at the tip is held at ground, which implies the bias voltage $V_{EFM} = -V_{sample}$. Protons migrate according to the sign of the bias.[23] A bias voltage $V_{EFM} = -0.5V$ for example, implies a positive sample voltage, which forces protons toward the surface. The presence of protons within the hydrophilic channels results in an electrostatic force on the tip. Difference in phase between the drive signal and the response of the cantilever caused by this electrostatic force is measured as the EFM phase shift, which is imaged in EFM.[92,95] Figs. 3.6Ci, 3.6Cii, and 3.6Ciii show EFM phase images of Nafion at three different applied voltages $V_{EFM} = -0.5V$, 0V, and +0.5V, respectively.

Structural information can be gleaned from the EFM phase images by considering the voltage dependence of the EFM phase signal for individual aqueous domains. The blue square, green oval and magenta circle in 3.6B are used to mark the locations of three individual hydrophilic domains. These same markers are used in the EFM phase images of Fig. 3.6Ci, 3.6Cii and 3.6Ciii to illustrate the change in EFM phase contrast of these three individual domains as a function of applied voltage. Fig. 3.6D shows a plot of EFM phase shift vs. V_{EFM} for each of these three domains. The data points are labeled by blue squares, green ovals and magenta circles; the same colors as in the corresponding EFM images in

Figs. 3.6Ci, 3.6Cii and 3.6Ciii. The line traces in Fig. 3.6D represents a fit to the data points

using a quadratic function.

To this end, the EFM phase vs. V_{EFM} data of three individual channels in Nafion shown

in Fig. 3.6D were fitted to a quadratic function, which is illustrated in the line traces of Fig.

3.6D. The data of Fig. 3.6D are representative of the three categories of EFM phase shifts

observed in Nafion films as a function of V_{EFM}: a quadratic (blue), linear (magenta), and null

(green) dependence. We have analyzed a total of 19 individual hydrophilic domains with

EFM. For each domain the EFM phase ($\Delta\Phi$) vs V_{EFM} was fit to a quadratic function:

$$\Delta\Phi = \Delta\Phi_q + \Delta\Phi_C = AV_{EFM} + BV_{EFM}{}^2 \qquad (3.8)$$

which contains a linear and quadratic term. If $A \cong 0$ then the plot of $\Delta\Phi$ vs V_{EFM} has a

quadratic dependence. If $B \cong 0$ then the plot of $\Delta\Phi$ vs V_{EFM} has a linear dependence. If both

A and B are very small, then the plot of $\Delta\Phi$ vs V_{EFM} has a null dependence.

It is important to note that before background subtraction, we observed parabolic

dependence of the phase shift with bias voltage. Figure 3.7 shows the parabolic response

before background subtraction of the same channels shown in Fig. 3.6.
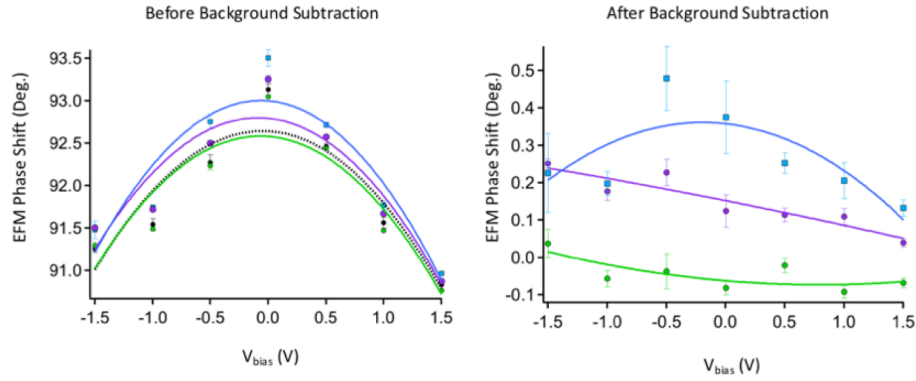
Figure 3.7: Representative parabolas before background subtraction for all regions shown in Figure 2. The background curve is the black dashed line, which is also shown in Figure 3.6Di. Note that $V_{bias} = -V_{EFM}$.

E. Modelling of EFM

1. Plane Capacitor Model – Capacitive Force between Tip and FTO

The capacitance is dependent on the dielectric constant of the material separating two conductors and the geometry of the capacitor. Since the AFM probe is typically treated as a cone and the samples of interest have non-trivial geometries, modelling the results of EFM can be complicated. Martin *et al.* was the first to describe a tip-plane system as a simple parallel plate capacitor.[96] Its validity in comparison with other analytical models was further verified by Belaidi *et al.*[97] The capacitive force exerted on one plate is defined as:

$$\vec{F} = -q\vec{E} \tag{3.9}$$

where

$$\vec{E} = \frac{\sigma}{2\varepsilon_0} \tag{3.10}$$

σ is the surface charge density, defined as q/A. A is the surface area of the plates and ε_0 is the vacuum permittivity.

Lastly,

$$q = C V_{EFM} = (\frac{A \varepsilon_0}{z\prime}) V_{EFM} \tag{3.11}$$

where z is the separation distance (lift-height) between the two plates. By substitution of equations 3.9 into 3.11, the analytical expression for the capacitive force becomes:

$$\vec{F} = \frac{-A \varepsilon_0 V_{EFM}{}^2}{2 z^2} \tag{3.12}$$

It is important to note that this analytical expression only takes into account the capacitive force between the tip and the substrate (FTO). A model that includes the capacitive force due the polarizability of the membrane film and the Coulombic force due to the stored charge enclosed in individual channels must also be taken into account.

2. Capacitive Force Due to Polarization of the Membrane

The membrane creates an additional capacitive force that must be taken into account. The polarization of the film is due to the electric field, E, from the uniform parallel plate depiction given by:

$$\vec{P} = \alpha \vec{E} \tag{3.13}$$

where α is the polarizability. A schematic of the EFM-membrane system as a parallel-plate model is shown in Fig. 3.8.
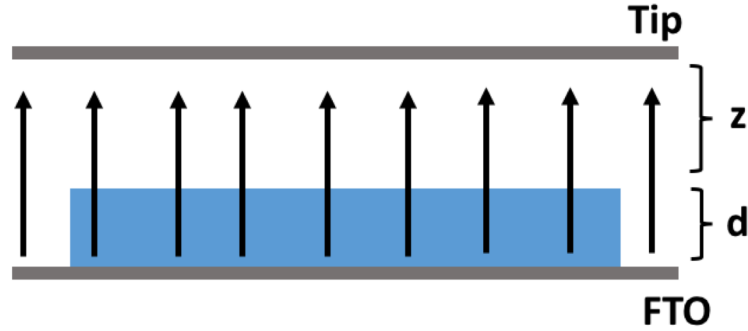
Figure 3.8: Cartoon of EFM-membrane system depicted as a parallel plate capacitor. The blue film represents the Nafion with a thickness, d. The arrows represent the electric field lines.

The capacitive force (F_c) due to polarization of the film, which can be derived from Gauss's law is:

$$\vec{F}_c = \alpha \vec{E} \frac{d\vec{E}}{dz} \tag{3.14}$$

E in terms of the potential difference is:

$$E = \left(\frac{V_{EFM} - V_S}{z+d} \right) \tag{3.15}$$

where z is the lift-height and d is the thickness of the film. By substitution, Eqn. 3.14 becomes:

$$F_c = \frac{-\alpha(V_{EFM}-V_S)^2}{(z+d)^3} \tag{3.16}$$

Therefore, the EFM phase shifts due to the polarization of the film becomes:

$$\Delta\Phi_c = \frac{3}{2} \frac{Q}{k} \frac{\alpha(V_{EFM}-V_S)^2}{(z+d)^4} \tag{3.17}$$

49

Eqn. 3.17 shows that the polarizability, α, and film thickness, d, contribute to the quadratic dependence of V_{EFM}.

3. Coulombic Force between Tip and Membrane

Lastly, the stored charge in the membrane is taken into account. The Coulombic force exerted on the tip by the film is:

$$\vec{F_q} = q \cdot \vec{E} = q \cdot \left(\frac{V_{EFM} - V_S}{z+d}\right) \tag{3.18}$$

The EFM phase shift as a function of V_{EFM} is:

$$\Delta\Phi_q = -\frac{Q}{2k} \frac{q \cdot (V_{EFM} - V_S)}{(z+d)^2} \tag{3.19}$$

Therefore, the Coulombic interactions, which depends linearly with V_{EFM} is contributed by the total stored charge, q, and the film thickness, d.

4. Isolated Cylinder Model vs. Embedded Cylinder Model

The parallel plate capacitor model is useful due to its simplicity and analytical expressions for the linear and quadratic dependence can be derived on V_{EFM}. However, deriving analytical expressions for tip-sample forces for more complicated tip and sample geometries are either difficult or impossible. Thus, numerical methods such as the finite element method[98] and surface charge method[96,99] are often employed to simulate the tip-sample forces. This discussion will focus on the finite element method.

In the context of EFM, the finite element method solves Poisson's equation by dividing an arbitrary domain (the entire tip-sample geometry) into smaller domains, thus creating a boundary "mesh". Briefly, the error from trial functions are minimized over finite elements and a global system of equations is generated from the elemental equations.

Melin and co-workers similarly derived analytical expressions as Eqns. 3.17 and 3.19 from the parallel plate model and compared the results to the numerical result using the finite element method of conical tip and a nano-cylinder sample.[100] They analyzed the ratio:

$$R = \Delta\Phi_q/\Delta\Phi_c \qquad (3.20)$$

They showed that the expression for the ratio was:

$$R = \frac{-g\,q\,z}{3\,\varepsilon\,\varepsilon_0 A(V_{EFM}-V_S)} \qquad (3.21)$$

The ratio for the conical tip and nano-cylinder was similar to the plane-shaped tip and nano-cylinder, but only differed by a correction factor, g. They showed g = 1/3 for the plane tip model and g = 2/3 for the conical tip model.

In contrast to the isolated cylinder model, a Nafion film is a complex material due to the phase separation, which results in aqueous channels of unknown morphology dispersed randomly in a fluorocarbon matrix. Nevertheless, if we assume that the aqueous domains are roughly cylindrical then we can utilize what we know from the EFM of the isolated cylinder model systems to help interpret our EFM data of Nafion. A schematic comparing these two models is shown in Fig. 3.9.
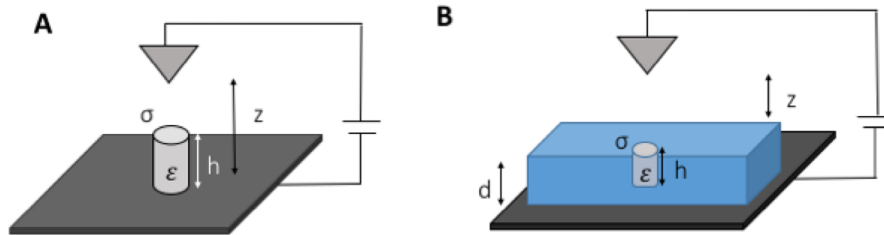
Figure 3.9: (A) Schematic of EFM plane capacitor influenced by a cylindrical nanostructure described by Melin *et. al.* (B) Similar description of cylindrical nano-channels embedded in a fluorocarbon matrix.

Fig. 3.9B illustrates a simple cylinder model for aqueous channels embedded in Nafion. Inspecting the cartoons of Fig. 3.9A and 3.9B it is easy to see the similarity between the isolated cylinder model and the Nafion film model. The dielectric cylinders of Fig. 3.9A are represented in Fig. 3.9B by the cylindrical aqueous channels surrounded by a fluorocarbon matrix. The main difference between the isolated cylinder model of Fig. 3.9A and the Nafion model of Fig. 3.9B is the dielectric constant of the surrounding medium, which is air in the case of Fig. 3.9A and fluorocarbon in the case of Fig. 3.9B. Thus, it should be possible to apply what is known from the isolated cylinder model to our Nafion film model. From Eqns. 3.17 and 3.19, we can define the linear and quadratic coefficients from Eqn. 3.8.

$$B = -\frac{Q}{2k}\left(\frac{3\epsilon_0 Sh}{z^4}\right) \tag{3.22}$$

$$A = \frac{Q}{2\,k\,\epsilon_R\,z^3}\,h\,q \tag{3.23}$$

q is the total charge enclosed and S is the surface area of the top face of the cylinder. B is only dependent on the cylinder volume and has no dependence on charge. The coefficient A, however, is dependent on the total charge enclosed, the cylinder length, and the relative permittivity.

5. Mathematica Simulations of an Embedded Channel

The tip-sample force as a function of applied bias was modeled as a parallel capacitor in which a channel of uniform charge is surrounded by a dielectric matrix. In Mathematica, the Poisson's equation was solved numerically using finite element method with Dirichlet boundary conditions. 3.10A shows the defined boundary mesh that schematically represents the tip-Nafion system in which a disconnected channel is shown. The relative permittivity was defined for different regions: air = 1, channel = 80, matrix = 2. Figure 3.10B shows the

result of numerically solving Poisson's equation showing a contour of the scalar potential over the boundary mesh for an FTO potential of 0. It is important to note that in this simulation, only the length of the channel was varied to analyze the effect of the force applied to the tip. The width and charge density were constants. The force applied to the tip was calculated for different FTO potentials by taking the gradient of potential to get the electric field. The force acting on the tip in a parallel capacitor is defined as:

$$F = \frac{\varepsilon_0}{2} \int E^2 \cdot n_y dl \qquad (3.24)$$
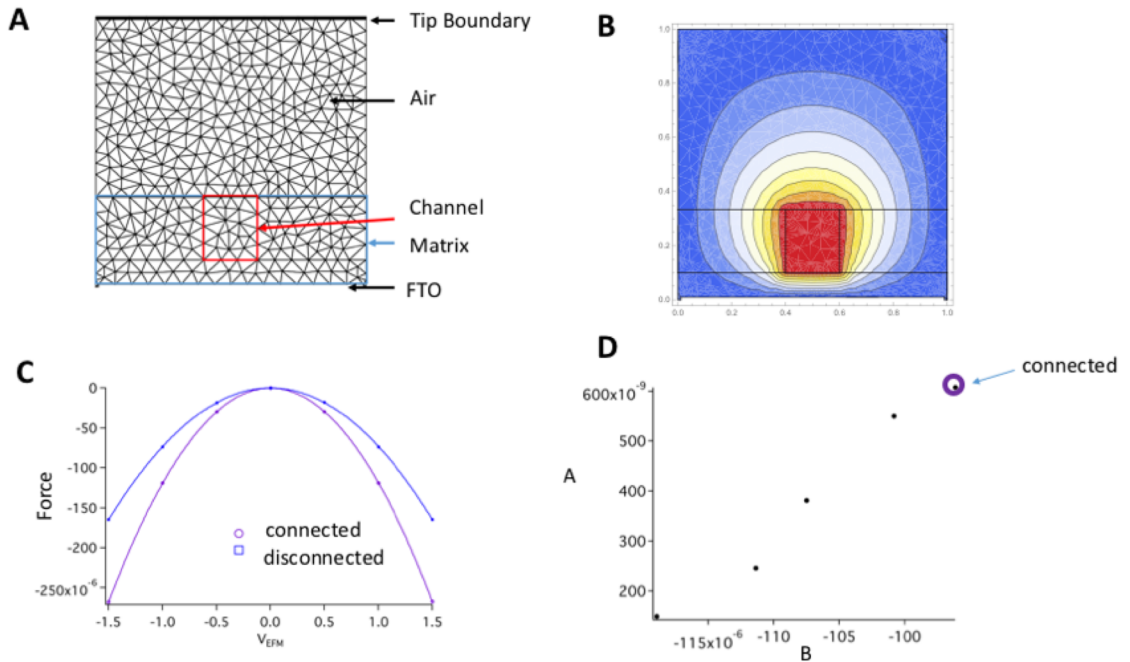
Figure 3.10: Finite element method simulations from Mathematica. (A) Boundary mesh for the EFM – Nafion system. (B) Scalar potential field resulting from solving Poisson's equation. (C) The force exerted on the tip by the sample as a function of V_{EFM}. Shown are two quadratic fits of two types of channels: a long connected channel and a short disconnected channel. (D) The linear term, A, is plotted vs. the quadratic term, B, for the two channel types.

In Mathematica, a finite sum of the normal components of the electric field were taken to solve for the total force. Figure 3.10C shows the relationship between the force applied to the tip vs. V_{EFM} for a connected channel and a disconnected channel and were fit to a parabola. The case shown in 3.10B represents a disconnected channel. The parabolic fit parameters were plotted, and a positive trend is shown between A and B for varying channel lengths shown in 3.10D. Long connected channels give rise to larger A with B approaching zero, while short disconnected channels give rise to lower A with more negative B. Thus, the influence of channel length agrees with our interpretation from the isolated cylinder model.[96] The Mathematica script can be found in the Appendix.

F. Assignment of EFM Phase Behavior with Channel Structure

Each domain is fit to a quadratic function, subtracted from the background, and classified as either linear (A>>B), quadratic (B>>A), and null (A≅0 and B≅0). Using our embedded cylinder model, we can understand how A and B are affected by channel length.
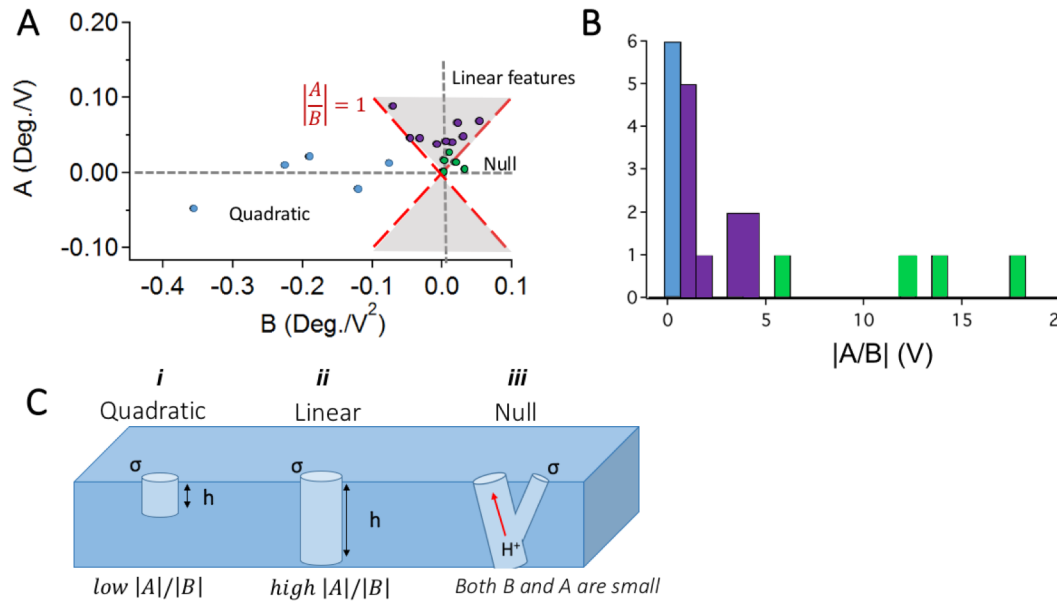
Figure 3.11: (A) Spectrum of quadratic and linear coefficients showing a positive trend from quadratic channels to linear and null channels. The dashed red line shows the $\left|\frac{A}{B}\right| = 1$ condition. The gray region shows which data points correspond to $\left|\frac{A}{B}\right| > 1$. (B) Color-coded histogram of |A/B| values in which blue corresponds to the quadratic channels, purple corresponds to linear, and green corresponds to null. (C) Model proposed illustrating how different channel structures give rise to quadratic, linear, and null phase shifts.

First, the A and B coefficients were plotted to evaluate their correlation. Figure 3.11A shows a scatter plot of the fit coefficients: the linear term, A, and the quadratic term, B. Using equations 3.21 and 3.22, the ratio A/B provides an expression that is dependent on both the shape and the dielectric properties of the channel:

$$\frac{|A|}{|B|} \propto \left(\frac{h}{\epsilon_R}\right)\left(\frac{q}{V}\right) \tag{3.25}$$

where h is the channel height, q is the total charge in the channel, ϵ_R is the relative dielectric constant and $V = S \cdot h$ is the volume of the channel. The quantity $\left(\frac{q}{V}\right)$ represents the charge density in the channel and is related to the spatial distribution of sulfonate groups that is assumed to be uniform.[96] Thus, comparing the ratio $\left|\frac{A}{B}\right|$ for different channels results in a comparison of $\left(\frac{h}{\epsilon_R}\right)$ for different channels assuming the charge density (i.e. the spatial distribution of the H^+ ions within the channel) is roughly constant. The dashed red line shows the $\left|\frac{A}{B}\right| = 1$ condition. Figure 3.11B shows the distribution of the ratio $\left|\frac{A}{B}\right|$ in which the color of each bin matches the color corresponding to data shown in 3.11A. EFM phase shifts that have quadratic dependence with V_{EFM}, the ratio of $\left|\frac{A}{B}\right|$ is small (< 1.0), which implies a small h and is indicative of a short, dead-end channel. These channels are depicted by the blue data points in the scatter plot of Fig. 3.11A and 3.11B. Using the isolated cylinder model[101] as a guide we can infer a short cylindrical channel structure as illustrated in Fig. 3.11C-i. Similarly, for EFM phase shifts that depend linearly with V_{EFM}, $\left|\frac{A}{B}\right|$ is large (> 1.0), which implies large h and is indicative of a long cylindrical channel. These channels are depicted by the purple data points in the scatter plot of Fig. 3.11A and 3.11B, and are represented in the structural model of Fig. 3.11C-ii. In 3.11A, the gray region shows which data points correspond to $\left|\frac{A}{B}\right| > 1$. EFM phase shifts that have no dependence on V_{EFM} are referred to by the "null" designation and are represented by the green dots in the scatter plot of Fig. 3.11A and 3.11B. 3.11A shows 4 green data points. One data point falls outside the

red dashed lines. Three other "null" points do not fall directly on the (0,0) origin, but are close given the measurement error of ~0.02°. These channels have $|A| \approx 0$ and $|B| \approx 0$, which was not predicted by the isolated cylinder model,[96] hence why $\left|\frac{A}{B}\right| \gg 1$ in 3.11B. We attribute the null dependence to branched channel as depicted in the structural model of Fig. 3.11C-iii. In the branched channel the charge is not influenced by the voltage bias due to the presence of a path of least resistance for the charge. This path is denoted by the red arrow in the structural model of Fig. 3.11C-iii. The modulation of charge would be dominated by this larger branch. If the tip is placed over the smaller branch then the observed EFM phase shift would be independent of V_{EFM}, which is consistent with our data.

It is important to note that the ratio $\left|\frac{A}{B}\right|$ is sensitive to $\left(\frac{h}{\epsilon_R}\right)$ for each channel. Until now we have assumed that the relative permittivity ϵ_R is the same for each channel. This approximation works well for channels with large surface area of the order of 50 nm^2. For narrow channels, however, this approximation breaks down. A radial-dependent permittivity has been shown using a Poisson-Boltzmann approach for cylindrical channels. A drop in the permittivity occurs at a distance of 3-6 Å from the sulfonic side chain boundary wall.[96] Thus, for very narrow channels both the length of the channel and the permittivity can influence $\left|\frac{A}{B}\right|$.

F. Conclusions

Using EFM we have shown that the pore structure in Nafion can be characterized by long connected channels that conduct protons from one side of the membrane to the other, short dead-end channels that are open to one side of the membrane but do not connect to the

opposite side of the membrane, and branched channels that have multiple paths from one side of the membrane to the other. The differences in the EFM phase dependence on applied voltage allows each channel to be assigned to a particular structural motif. With these imaging techniques, future comparative studies of thin films under humidity controlled conditions could provide an improved understanding of how channel connectivity is tied to membrane water content.

IV. Humidity-dependent Surface Structure and Hydroxide Conductance of a Model Quaternary Ammonium Anion Exchange Membrane

Portions of this chapter are reproduced from:

Austin M. Barnes, Brendan Liu, Steven K. Buratto. Humidity-dependent Surface Morphology and Hydroxide Conductance of a Model Quaternary Ammonium Anion Exchange Membrane. *Corrections re-submitted to Langmuir (8/29/19).*

A. Introduction

PEMs like Nafion, are typically perfluorosulfonic acid (PFSA) polymers consisting of a fluorocarbon backbone and a sulfonic acid side-chain. AEMs on the other hand commonly consist of a hydrocarbon backbone and a quaternary ammonium (QA) cation, which is water solvating and mobilizes the OH^-.[102] While there is still no benchmark AEM, FAA-3 by FuMA-Tech GmbH represents one of the few high performance and chemically stable AEMs that is also commercially available.[31] The complete chemical structure has not been published, but has been reported to be an aminated poly(phenylene oxide) (PPO) backbone[103,104] with QA functionality.[105] Its bulk properties including conductivity, mechanical strength, and morphology have been the subject of several recent reports.[34,106] Marino and co-workers have recently reported bulk conductivity and small angle x-ray scattering (SAXS) as a function of water content of FAA-3 in both the bromide and hydroxide form.[34,103,106–108] The water content is defined as λ=[mol H_2O]/[mol QA]. At sufficiently high water content ($\lambda > 20$) in the hydroxide form, a random phase separated

59

nano-morphology was inferred from SAXS giving rise to OH⁻ mobility comparable to Nafion.[34] What remains to be understood is how these bulk measurements are tied to the surface morphology and spatial distribution of hydroxide current through the membrane.

O'Dea *et al.* had previously compared the surface morphology of Nafion 212 by atomic force microscopy (AFM) to bulk morphologies inferred from SAXS across a wide range of relative RH.[34] At dry and ambient conditions (3-50% RH), the morphology resembles the cluster network[23] or the parallel cylinder model.[75] These models are inferred from the ionomer peak and matrix knee, corresponding to the higher scattering angle regime. Kusoglu *et al.* has measured the domain-spacing (i.e. d-spacing) of Nafion with grazing-incidence SAXS (GISAXS) and found the spacing of hydrophilic domains was 3-4.5 nm.[109] Bass *et al.* has also revealed by GISAXS that Nafion micelles orients parallel to the surface.[110] At 95% RH and higher, elongated worm-like features were observed that were ~40 nm in width and microns in length. This observation coincides with the rod-like model put forth by Rubatat and co-workers in which features 6-80 nm in length were reported by AFM and analysis of the SAXS intensity upturn (low scattering angle) of hydrated Nafion.[19] While this model suggests a semi-crystalline hydrophobic rod surrounded by ionic aggregates, conductive-probe AFM (cp-AFM) of hydrated Nafion revealed the elongated features were insulating, which suggests a ionic interior surrounded by a fluorocarbon shell.[13] Currently, the most accepted model is a locally flat hydrophilic domains, which was derived from the linear scaling in the d-spacing with hydration.[111]In work reported here, we combine phase imaging with cp-AFM to image the surface morphology and hydroxide conductance of FAA-3, which serves as our model QA-based AEM. We compared the differences in morphology between dry and humidified states in both the Br⁻ and OH⁻ forms.

Hydrocarbon-based AEMs exhibit higher water uptake percentages than fluoropolymer counterparts, which impacts the morphology of the AEM.[112] An increase in hydrophilic domain size was observed under increasing exposure time to humidified N_2, which is indicative of membrane swelling at the surface. In the Br^- form, randomly dispersed spherical clusters are visible at hydrated conditions. In the OH^- form, elongated worm-like features were observed under similar conditions. In both Br^- and OH^- forms at dehydrated conditions, no phase contrast could distinguish the hydrophilic domains. The current was imaged for a ½ MEA sample in which ultra-pure humidified H_2 and O_2 were supplied at the anode (beneath the GDE) and cathode (conductive tip), respectively. We suggest that these elongated worm-like features seed the formation of micellar non-conductive micellar surface structures, which indicates a high degree of swelling at the surface.

B. Experimental

Fumapem FAA-3-50 membranes by FuMA-Tech GmbH were purchased from FuelCellStore and delivered in the dry Br^- form. There was no pre-treatment step prior to hydrating or dehydrating the membrane in the Br^- form. The membranes were ~50 μm thick with an ion exchange capacity (IEC) of 2.02 meq/g. Fumion FAA-3-SOLUT-10 dispersion (10 wt% in NMP) was also purchased from FuelCellStore. A custom commercial gas diffusion electrode (GDE) (no Nafion post-coat) was purchased from FuelCellsEtc (0.5 mg/cm^2 Pt, 60% PtC).

Hydroxide exchange was performed by soaking the membrane in 1M KOH for 24 h at room temperature. Prior to phase imaging, the membranes were rinsed with deionized water, shaken off of excess water, then quickly mounted to a steel puck by a 10 μL drop of Fumion solution. The sample was placed in a modified closed fluid cell (modified Polyheater,

Asylum Research). Dry or humidified N_2 was supplied to the cell at 0.03 L/min achieving a relative humidity (RH) of 3% or 80% at room temperature, respectively. The RH was measured using an external humidity sensor (Honeywell).

Small patches of GDEs (0.25 cm^2) were first pretreated with ethanol to improve the wettability of the GDEs with Fumion dispersion solution. Fumion solution (2x20 µL drops) was applied to the catalyst layer. A Q-tip was used to gently brush the solution uniformly over the surface. The GDEs were then placed in a vacuum oven for 2 h at 50 ºC. The ½ membrane electrode assembly (MEA) was prepared by placing a Fumapem membrane in the hydroxide form over the impregnated GDE. The membrane adhered to the steel puck by Fumion solution. The sample was quickly sandwiched by 2 Teflon sheets and stored in a fabricated steel clamshell with a 4.5 kg weight plate centered over the ½ MEA for an effective pressure of ~18 kg/cm^2 (256 PSI) for 24 h. The ½ MEAs were then dried in a vacuum oven at 50 ºC for 24 h. The ½ MEAs were quickly placed in the closed fluid cell and allowed to equilibrate under humidified N_2 for several hours prior to current imaging.

Phase images were collected in tapping mode using an atomic force microscope (Asylum Research MFP-3D). Standard silicon probes (HQ:XSC11, Mikromasch) with a nominal resonant frequency of ~300 kHz and spring constant 40 N/m were used. Prior to collecting phase images of hydrated FAA-3-OH⁻, the cell was flushed with humidified N_2 for several hours in order to avoid CO_2 contamination. Similarly, dry N_2 was applied for dehydrated FAA-3-OH⁻. Current images were collected using a standard ORCA module with 500 MΩ sensitivity. Platinum coated tips (HQ:XSC11/Pt, Mikromasch) with a nominal resonant frequency of ~80 kHz and spring constant of ~2.7 N/m were used. Images were acquired in contact mode with a typical contact force of ~20 nN. After equilibration in

humidified N_2, humidified high purity H_2 and O_2 were supplied via gas flow channels (Scribner model 850 C fuel cell test system) at 0.03 L/min underneath and over the ½ MEA in the closed fluid cell, respectively. A +1V sample bias was typically applied to the carbon electrode to improve signal. Common in cp-AFM measurements due to the electrical impedance of the instrument, 5pA offset was applied. The average diameter of the domains from Fig. 4.1B was analyzed using a particle analysis algorithm in Igor Pro. The average length and width of the domains from Fig. 4.1E were measured by taking line profiles. The power spectral densities (PSDs) were computed in Gwyddion and plotted in Igor Pro. The position of the peak indicates the maximum spatial frequency of the AFM phase images. We identify the first peak (q) in the PSD. The d-spacing is defined as $\frac{2\pi}{q}$.

C. Results and Discussion

The surface morphology was observed in the Br^- and OH^- form under dry (18% RH) and hydrated (80% RH) conditions using the phase in tapping-mode AFM shown in Figure 4.1. Phase deviations depend on whether the tip-sample interactions are attractive (>90°) or repulsive (<90°). Tip-sample power dissipation is related to the sine of the phase angle, hence phase deviations toward 90° imply maximum power dissipation.[23] Under dehydrated conditions, the phase was in repulsive-mode due to the increased rigidity of the membrane. Little phase contrast was observed under 18% RH for both Br^- and OH^- shown in Fig. 4.1A and 4.1C, respectively. This indicates that FAA-3 does not form a phase-separated channel morphology on the surface under dehydrated conditions, which agrees with SAXS.[24] Furthermore, the water content (λ=[mol H_2O]/[mol QA]) of the membranes is low at such dry conditions ($\lambda \cong 0.5$ for FAA-3-Br^- and $\lambda \cong 5$ for FAA-3-OH^-) which is not a sufficient

number of water molecules to dissociate the counter ion in these hydrocarbon-based AEMs, and the conductance of OH⁻ goes to zero.[34]
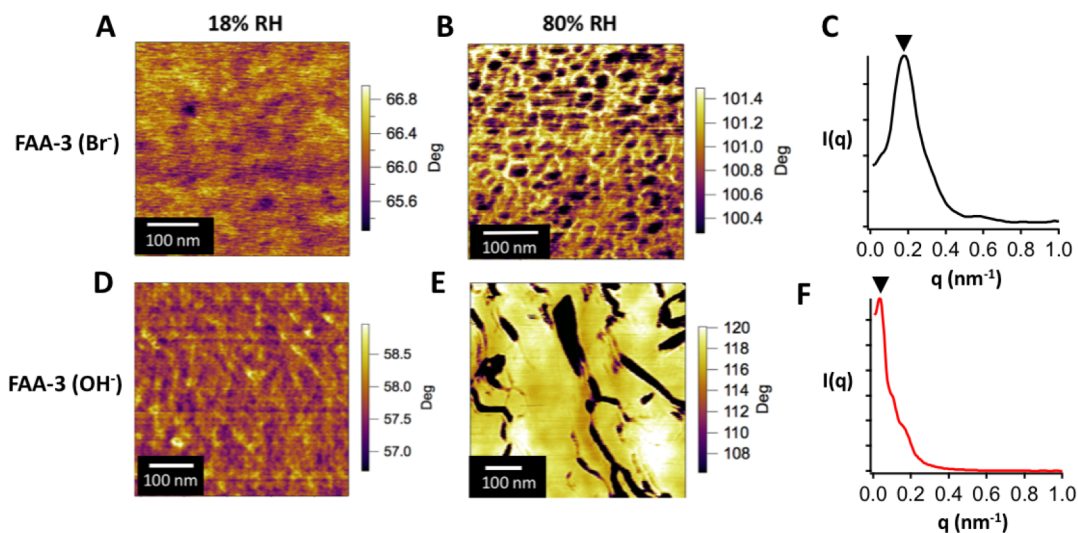
Figure 4.1: Tapping-mode phase images of FAA-3 in the bromide form (A,B) and hydroxide form (D,E) under 24 h exposure to 18% (A,D) and 80% RH (B,E). Power spectral density plots (C,F) from the images 4.1B and 4.1E.

At 80% RH, attractive-mode phase was achieved due to the increased compliance of the membrane and increased water uptake ($\lambda \cong 3$ at 80% RH in the bromide form).[34] For FAA-3-Br⁻ under hydrated conditions, a random pore morphology was observed, which was qualitatively similar to the surface morphology of Nafion.[34] This is contrary to bulk scattering observations in which only a diffuse ionomer peak was shown in the Br⁻ form even at high water contents.[23,24] We suggest that the increased chain flexibility near the surface can accommodate larger degree of surface rearrangement than in the bulk. In attractive-mode, dark contrast implies maximum power dissipation, which we infer as the hydrophilic domains.[34] The domains cover approximately 17% of the surface with an

64

average diameter of 15.4 nm. Power spectral density (PSD) plots were used to analyze the

spatial frequencies of AFM images.[23,24] The PSD plots shown in Fig. 4.1C and 4.1F were

measured from images shown in 4.1B and 4.1E, respectively. The radially-averaged

correlation length ($d_{spacing}$) between two hydrophilic domains was determined by the relation

$d_{spacing} = \frac{2\pi}{q}$. q is the position of the primary peak labelled by the black triangle. From

image 5.1B, the $d_{spacing}$ was 37 nm.
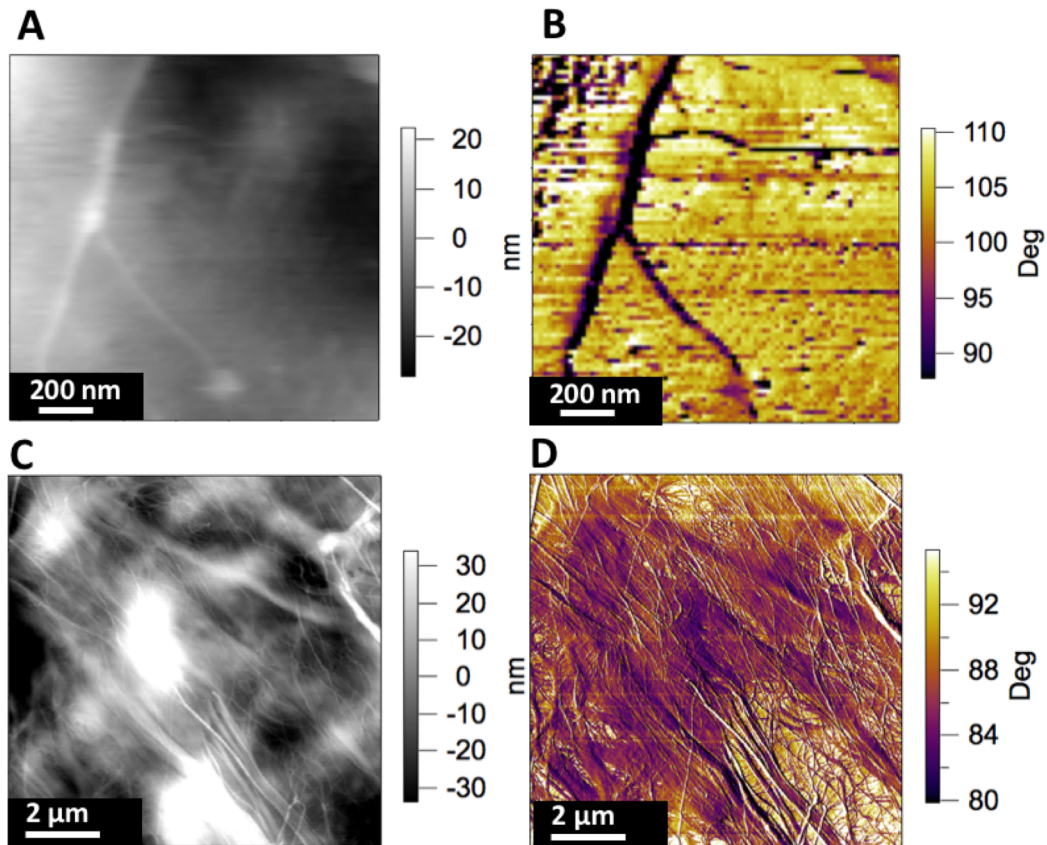
Figure 4.2: (A,C) Height and (B,C) phase images of hydrated FAA-3-OH⁻ of a 1.5 x 1.5 μm scan and a 10 x 10 μm scan. Elongated fibrillar structures can be observed in both sets of images.

Under hydrated conditions in the hydroxide form (FAA-3-OH⁻), elongated fiber-like

domains were observed as shown in Fig. 4.1D. In the hydroxide form, the water uptake

increases significantly; $\lambda = 60$ when submerged under water.[69,113] In the bulk, a random pore network morphology was inferred from SAXS. An intense ionomer peak provided measurement of the d-spacing, which is defined as the correlation length between scattering objects. At $\lambda = 60$, the d-spacing was ~ 6 nm.[34] Our results show a significant change in the morphology that occurs at the surface in the hydroxide form. Features shown in 4.1D were measured to have an average width of 34 nm and an average length of 230 nm. The $d_{spacing}$ determined from the PSD plot from image 4.1D was 203 nm. From this analysis, the coalescence of surface domains gives rise to significantly larger domains and further spaced apart than results inferred from SAXS.[34] These distinct differences in the morphology and the sizes of the hydrophilic domains at the surface from the bulk has been observed in other AFM investigations of Nafion and similar perfluorosulfonic acids. [23,114,115] Aleksandrova *et al.* has reported the size of the conductive regions of Nafion to range 9-25 nm by cp-AFM.[68] He *et al.* has also shown the surface of Nafion has higher conductivity than the bulk at higher water content.[67] All of these reports indicate a rearrangement of the domains at the surface in order to minimize the surface free energy of the membrane.

Larger scans of these elongated features extend microns in length over the membrane's surface as shown in Figure 4.2. An isolated feature is shown in Figure 4.2A and 4.2B. The phase contrast in 4.2B reveals the feature is hydrophilic. Figure 4.2C and 4.2D shows a larger scan in which these features dominate the surface. While we found no correlation between the height and the phase images of Figure 4.1D, we found that topographic changes in the height to be associated with changes in the phase over prolonged exposure to high RH. Since the topography influences the phase in both of these sets of images, we cannot discern the chemical composition of these regions of the surface. During our preparation of

FAA-3-OH$^-$, the membrane was exposed to air for ~ 5 min. This could lead to an increase in domain size at the surface and bulk as a result of CO_2 reacting with OH$^-$ to form HCO_3^- or CO_3^{2-}. Divekar *et al.* measured SAXS of a perfluorinated AEM under CO_2 exposure and observed a ~2 nm shift in the d-spacing over 2 hours.[116] Therefore, conductive-probe AFM (cp-AFM) was used to visualize how such surface rearrangement influences the hydroxide conductivity through the membrane.

In cp-AFM, a Pt coated tip scans in constant contact with a ½ MEA sample. A schematic is shown in Figure 4.3. Humidified O_2 is supplied to the tip while H_2 is supplied beneath the gas diffusion layer. In recent cp-AFM measurements, only humidified O_2 was used.[34] Therefore, current signal originates from large tip biases (+2V) that split water into OH$^-$ and H_2 at the tip-membrane interface. This methodology may cause drift or unexpected spikes in current signal as a result of potential carbonate displacement.[117,118]
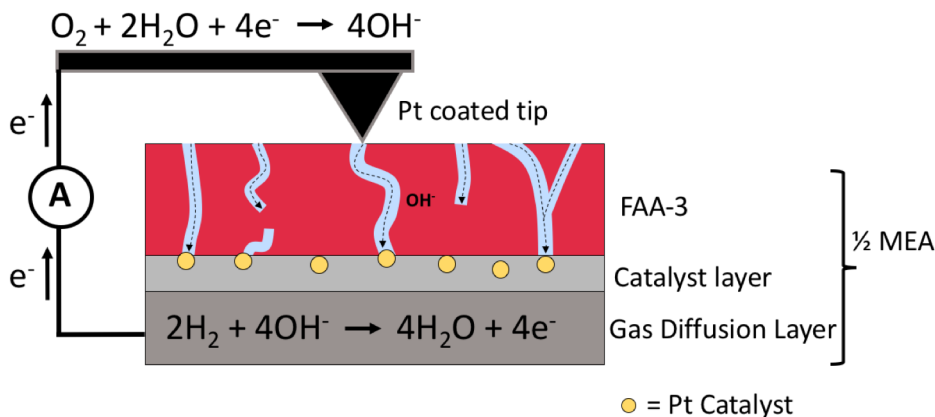
Figure 4.3: Schematic of cp-AFM experiment.

We have also observed a non-zero current signal with no fuel running, yet significantly higher current signal with fuel on. In both image sets, a +1V sample bias was applied. Both scans are of the same image area. Both scans start from the top of the image and scan down. It is important to note that the current is higher in this data than that from Figure 4.4 due to

higher contact force – 50 nN of force was used in this scan vs. 20 nN used in the manuscript. Distributions of the current from the current images is shown. The average current shifts by ~50 pA when fuel is turned on. A narrow distribution was observed when the fuel was off, while a broader distribution is shown with fuel on.
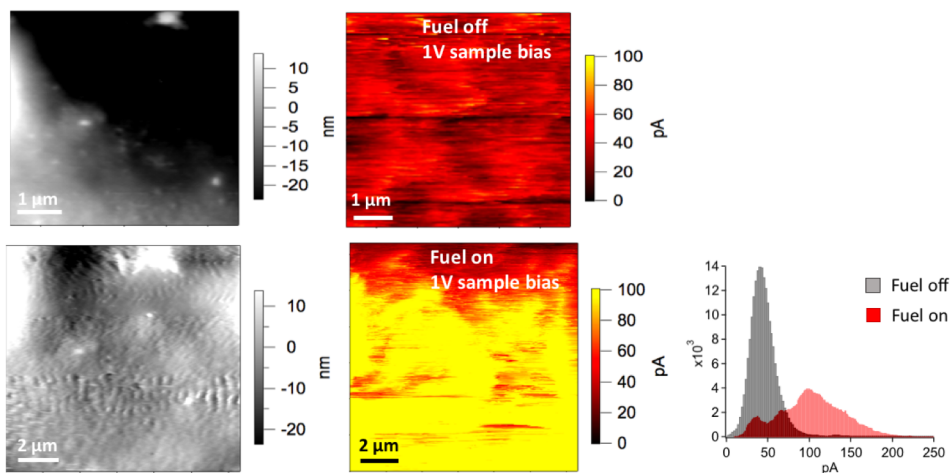
Figure 4.4: Comparison of height and current images with fuel off (top row) and on (bottom row). Distribution of current for fuel off (gray) and fuel on (red).

Furthermore, CO_2 contamination makes current imaging of AEMs difficult. While it has been reported that exposure to ambient air for 5 minutes leads to a 50% conversion of OH^- to CO_3^{2-},[119] our experience indicates that current images could still be readily achieved

even after 5-10 minute air exposure during sample preparation.
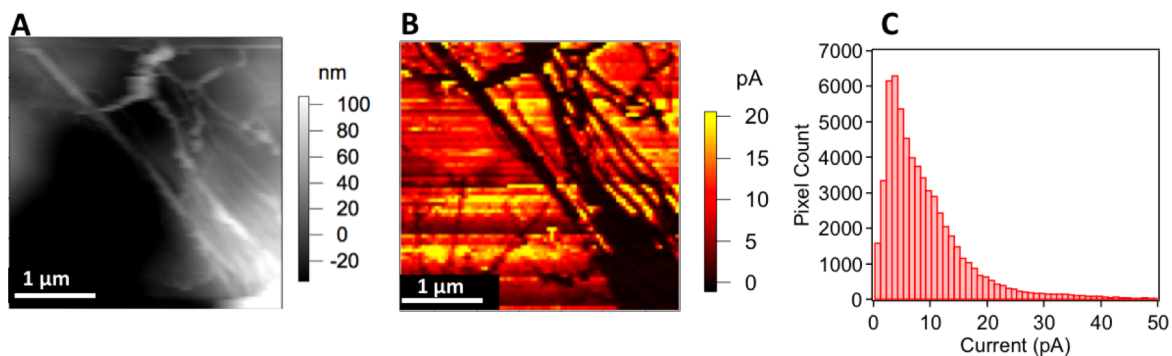
Figure 4.5: (A) 3x3 µm height and (B) current images of hydrated FAA-3-OH⁻ with +1V sample bias. (C) Current distribution from image B.

Figure 4.5A and 4.5B shows a representative height image and its corresponding current image, respectively. The current image shows elongated fibrillar regions with little to no hydroxide current while in between these regions show high current. Regions of poor conductance is likely due to the morphological structure of these regions correlated with the results inferred from phase imaging. We suggest the elongated hydrophilic domains observed in the images of Fig. 4.1D and Fig. 4.2 consist of a hydrophobic PPO shell with a QA interior. The morphology resembles the "worm-like" structures for both Nafion and the 3M membranes under hydrated conditions illustrated in Figure 2.6.[34] Interfacial effects strongly influence the surface rearrangement – the surface ionic sites orient internal to the membrane, increasing the hydrophobicity of the surface and minimizing the surface free energy.[23] While our observations pertain only to the cathode side in which water management in AEMFC operation is improved, the anode interface produces water, which could also induce similar swelling behavior observed here.

Regions of positive current exists between the insulating regions, which results from oxygen reduction between the hydroxide-rich domains and the Pt-coated tip. A distribution

of the current from 4.5B is shown in Fig. 4.5C. A large peak can be seen at ~5 pA indicates

the average current over the insulating regions while a broad tail extending greater than 30

pA indicates the distribution of conductive regions. We associate this distribution to a

heterogeneity in channel connectivity, catalyst activity, or a combination of the

two.[23,67,110,120] The through-plane conductivity by cp-AFM can be defined as $\sigma_{T-P} = \frac{d}{A \cdot R}$

where d is the membrane thickness (~50 µm). A is the surface area of the tip apex, which

can be modelled as a sphere. Given the radius of curvature of the Pt-coated tip to be 10 nm

and an average current of 5 pA, the through-plane conductivity is approximately 2 mS/cm.

This is in close agreement with recently reported bulk values of 7 mS/cm at 80% RH and

40° C,[26,121] although this discrepancy can be influenced by air exposure and tip-sample

contact force. It is important to note that increased current is typically observed as the tip

scans over larger topographic features due to greater tip-surface contact area. We did not see

this artifact in our scans. Furthermore, we saw no dependence on scan direction comparing

the trace and retrace images, which is shown in Figure 4.6.
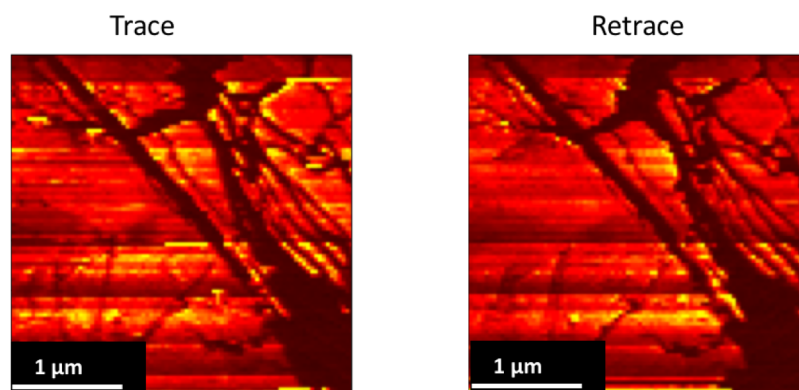
Figure 4.6: Trace and retrace scans of the current image shown in Figure 5.5B.

D. Conclusions

Hydroxide ion conductivity and water diffusion require transport across the ionic domains of the surface, therefore the surface morphology and hydroxide conductance of a model QA AEM was investigated by conductive-probe AFM. These results served to complement bulk-average scattering measurements.[108] At dehydrated conditions, our phase images indicate that no hydrophilic domains were observed in either the bromide or hydroxide form, owing to the lack of water retention and hydrophilicity of FAA-3. However, under hydrated conditions, the phase images showed a distinct morphology of the surface than the bulk. At 80% RH, the membrane in the bromide form showed randomly dispersed and isolated hydrophilic domains with an average diameter of ~15 nm. In the hydroxide form, elongated fibrillar structures were observed extending microns in length. SAXS indicates a locally flat nano-morphology with d-spacing (3-6 nm) scaling linearly with hydration level.[34] While these results have guided the understanding of the bulk morphology on the nanometer scale, it does not capture the long-range length scale (several microns) required for hydroxide conduction. Current imaging of hydrated FAA-3 in the hydroxide form revealed these elongated structures were insulating, suggesting that the high water content of the membrane induces surface rearrangement and excessive swelling. Such rearrangement impedes the transport of hydroxide from one end of the AEM to the other, but could also contribute to hysteresis of humidity cycling[34] as well as CO_2 adsorption. These queries can be addressed with techniques such as AFM that allow for environmental control. Given our recent findings and previous knowledge on the surface swelling behavior of PEM materials like Nafion, lightly crosslinked AEMs[108] or polymer/inorganic

composites[122,123] may provide an alternative to reduce swelling without sacrificing

hydroxide conductivity.

V. Phosphonium-Containing Block Copolymer AEMs: Effect of Quaternization Level on Bulk and Surface Morphology at Hydrated and Dehydrated States

Portions of this chapter were reproduced from:

A. Introduction

The most commonly characterized AEMs are quaternary ammonium based polymers, such as the FAA-3 AEM by Fumatech, because of the facile synthesis routes established in the literature.[124] However, QA polymers lack long term stability in alkaline environment.[31] One method to improve stability is by utilizing bulky quaternary phosphonium cations. These larger functional groups provide steric hindrance, which inhibits degradation.[125–128] In addition, phosphonium based polymers are solvent processable, showing solubility in DMF, alcohols, toluene, dichloromethane and chloroform, which makes them a promising candidate for not only fuel cell membrane, but also the ionomeric binder material at the catalyst layer.[42,129,130] Furthermore, the basicity of phosphonium hydroxide was higher than the ammonium counterpart, which contributes to

higher hydroxide conductivity. Although these findings have established important design principles for AEM materials, structural characterization revealing the impact of chemical modifications on size, shape, and connectivity of the ionic domains still needs further investigation.

Zhang *et al.* synthesized block copolymers of polyisoprene and quaternary phosphonium containing block (PIp-P(R$_3$P$^+$)MS).[128] Membranes with a range of IECs were prepared. Lamellar and hexagonal morphologies were observed from small angle X-ray scattering (SAXS) and cross-sectional transmission electron microscopy (TEM), at low to moderate IEC. Bulk chloride ion conductivities were then correlated with the morphology. Higher conductivity was achieved for a hexagonal morphology over lamellar morphology at similar IECs, likely a result of improved channel connectivity. We expanded on this work by developing a new synthetic strategy to achieve higher IEC (0.87-2.35 mmol/g) phosphonium diblock copolymers by utilizing NMP polymerization and implementing a smaller phosphonium quaternization agent. The synthesis and bulk characterization were carried out by Prof. Coughlin's group at University of Massachusetts, Amherst. The bulk and surface phase behaviors of neutral block copolymers have been well studied, but detailed understanding of charged block copolymers is still incomplete. Experimental and computational analysis have shown charge cohesion effects can induce the formation of nanostructures that are inaccessible to conventional uncharged block copolymers, thus shifting the phase diagram depending on the degree of quaternization.[131] Hybrid self-consistent field theory and liquid state theory (SCFT-LS) models have recently shown that chain length, charge fraction, charge size, and the strength of Coulombic interactions can lead to drastic morphology shifts.[40,132–135] What remains to be addressed is a comprehensive

comparison between the bulk and surface morphology as a function of charge fraction. In our study, bulk and surface morphologies of PIp-P(R$_3$P$^+$)MS membranes were investigated and their dependence on IEC, type of pendant phosphonium ion, the degree of quaternization and relative humidity were discussed. From the results, connectivity of ion exchange channels throughout the membrane can be revealed, which ultimately evaluates their capabilities of ion and water transportation as promising AEM materials.

B. Experimental

1. Synthesis

Isoprene was distilled and stored under −20 °C before use. CMS (mixture of *para-* and *meta-* isomers) were passed through basic alumina and stored at −20 °C before use. All other chemicals were used as received.

In a typical procedure, SG1 (38.14 mg, 0.1 mmol) was added to a Teflon sealed Schlenk flask containing isoprene (4 g, 5.87 ml, 58.7 mmol) and pyridine (5.87 ml) with equal volume fraction. Three cycles of freeze−pump−thaw were applied to degas the mixture, then the flask was backfilled with nitrogen and placed in an oil bath at 115 ^{o}C. After the polymerization, the reaction was quenched by immersing the flask into an ice bath for 10 min. The contents were transferred to a pre-weighed vial. Solvent and unreacted isoprene were removed by purging with dry nitrogen overnight then kept in vacuum oven for 24h. The viscous light-yellow liquid was obtained and weighed.

In a typical procedure, PIp-SG1 (1 g,Mn 9.3 kg/mol, Đ 1.16), CMS (3.22 g, 3 ml, 21.1 mmol) and *o*-xylene (6ml) were added to a Schlenk flask. Three cycles of freeze−pump−thaw were applied to degas the mixture, then the flask was backfilled with

74

nitrogen and placed in an oil bath at 105 ^{o}C for 12h. The chain extension was quenched by

immersing the flask into an ice bath for 10 min, and then precipitated into hexane for three

times to remove excess monomer CMS and dormant PIp homopolymer without chain

extension. A white powder was obtained.

2. Polymer Quaternization

A typical quaternization procedure consisted of dissolving PIp-PCMS (AEM 17*, 100

mg, with CMS moieties 0.55 mmol) and tris(2,4,6-trimethoxyphenyl)phosphine

($P(Ph(OMe)_3)_3$, 445 mg, 0.84 mmol) in 5 mL of DCM. The solution was purged with dry

nitrogen for 10 min before placing into 40°C oil bath while stirred for 3 days. After the

quaternization, the solution was precipitated into methanol to remove the excess

$P(Ph(OMe)_3)_3$and $P(R_3P^+)MS$ homopolymer (PCMS homopolymer, the side product during

chain extension of PIp-SG1, after quaternization). A white powder was obtained and dried in

vacuum oven overnight. PIp-PCMS (AEM 17, 20 mg, with CMS moieties 0.11 mmol) and

triphenylphosphine ($P(Ph)_3$) with reaction stoichiometries of 0.25, 0.5, 0.75 and 1 (7.28,

14.56, 21.85, 29.13 mg) were dissolved in 2 mL of chloroform, respectively. The solutions

with different $P(Ph)_3$ feeding ratios were purged with dry nitrogen for 10 min before placing

into an oil bath at 40°C for 3 days. After the quaternization, the solutions were precipitated

into methanol to remove the excess $P(Ph)_3$ and $P(R_3P^+)MS$ homopolymer. A white powder

was obtained and dried in vacuum oven overnight.

From chloroform solution, an aliquot of the quaternized membrane was drop-cast onto a

clean polytetrafluorethylene sheet and slowly dried overnight. Then the membranes were

annealed by saturated THF vapor for 24 h and dried in vacuum oven overnight before peeled

off the substrate and stored in a vial prior to bulk and surface characterization. The

thicknesses of the membranes were measured by AFM to be ~ 5 μm.

3. Bulk Characterization

GPC was performed in THF at a flow rate of 1.0 mL/min using a refractive index

detector on a Polymer Laboratories PL-GPC 50 Integrated GPC system.

NMR spectroscopy was performed in 5mm diameter tubes in deuterated chloroform

($CDCl_3$) at 25 $^{\circ}$C. ^{1}H and ^{31}P NMR spectroscopy was performed on a Bruker 500

spectrometer at 500 MHz (^{1}H) and 202 MHz (^{31}P).

SAXS measurements were performed using a GANESHA 300 XL SAXS. Humidity-

dependent SAXS measurements were performed at The Basic Energy Sciences Synchrotron

Radiation Center (BESSRC) at the Advanced Photon Source at Argonne National Lab on

beamline 12 ID-B. A Pliatus 2M SAXS detector was used to collect scattering data with an

exposure time of 1 s. The X-ray beam had a wavelength of 1 Å and power of 12 keV. The

intensity (I) is a radial integration of the 2D scattering pattern with respect to the scattering

vector (q). Temperature and relative humidity (RH) were controlled within a custom sample

oven. Typical experiments studied three membrane samples and one empty window so a

background spectrum of the scattering through the Kapton windows and nitrogen

environment could be obtained for each experimental condition. The RH of the sample

environment was controlled by mixing heated streams of saturated and dry nitrogen. Sample

holders were inserted into an oven environment of 40 °C and <10% RH. The samples were

allowed to dry for 40 min before X-ray test started. RH was then increased to 95% while the

temperature was maintained at 40 °C. X-ray spectrum was taken after one-hour

equilibration. Similarly, for drying process, RH was set to 0% while the temperature was maintained, and X-ray spectrum was taken after one-hour equilibration.

The TEM specimens were prepared by Leica CryoUltramicrotome. The microtome chamber was cooled down to -100 ^{o}C by liquid nitrogen, where the bulk sample was microtomed with a diamond knife to a thickness around 40 nm. The cutting sections were then collected by 400 mesh copper support grids and stained by OsO_4 vapor for 20 min at room temperature. TEM characterization was performed on a JEOL 2000FX TEM operated at an accelerating voltage of 200 kV.

4. Surface Characterization by AFM

Height and phase images were acquired in tapping mode using an atomic force microscope (Asylum Research MFP3D). Standard silicon probes (XSC11, Mikromasch) with resonant frequency (~300 kHz) and spring constant (40 N/m) were used. A closed fluid cell (modified Polyheater, Asylum Research) was used to control the relative humidity (RH). Membranes were mounted by epoxy resin to a metal puck, which could be screwed in place inside the closed fluid cell. Membranes were hydrated by equilibrating at 80% RH for 2 hours. Humidified nitrogen was supplied to the cell at 100 mL/min. Humidity was measured in the cell using an external humidity sensor (Honeywell). Membranes were dehydrated in a vacuum oven at 70 °C for 24 h, then imaged in N_2 environment at 18% RH. The sizes of the hydrophilic and hydrophobic domains were measured using the particle analysis tool in Igor Pro by applying a threshold to the sample using the iterative method.[135–142] The spacing between the cylindrical aggregates (d-spacing) of the lamellar surfaces were measured by measuring both line profiles and the radially averaged 1-D power spectral

density (PSD). The phase images were used for analyses because the phase offered greater contrast than topography. The PSDs were computed in Gwyddion and plotted in Igor Pro. The position of the peak indicates the maximum spatial frequency of the AFM phase images. The first peak in the PSD is taken as (q_1). The d-spacing is defined as $\frac{2\pi}{q_1}$, which was measured and averaged over 5 different images for AEM 13 at the 3 RH levels.

C. Synthesis of PIp-P(R$_3$P$^+$)MS

Previously, phosphonium-pendant diblock and triblock copolymers were synthesized by reversible addition-fragmentation chain transfer (RAFT) polymerization.[143] Chloromethylstyrene (CMS) was polymerized first, and then chain extended with isoprene (Ip). The benzylic position on CMS is electrophilic for subsequent quaternization by nucleophilic attack. Polyisoprene (PIp) was chosen because of its low glass-transition temperature (T_g) and attendant flexibility.

In this study, NMP was chosen for block copolymer synthesis due to its fast propagation rate at high temperature (120 °C). The use of *N-tert*-butyl-*N*-[1-diethylphosphono-(2,2-dimethylpropyl)] nitroxide (SG1) to mediate the polymerization of Ip provides living character. By using pyridine, a polar solvent, intramolecular hydrogen-bonding is disrupted, therefore, the polar SG1 initiator was stabilized, providing further control over polymerization.[131] By modulating the feeding ratio of Ip and initiator SG1, molecular weights of ~9 and 62 kg/mol PIp were successfully synthesized with narrow

Scheme 1. NMP synthesis route
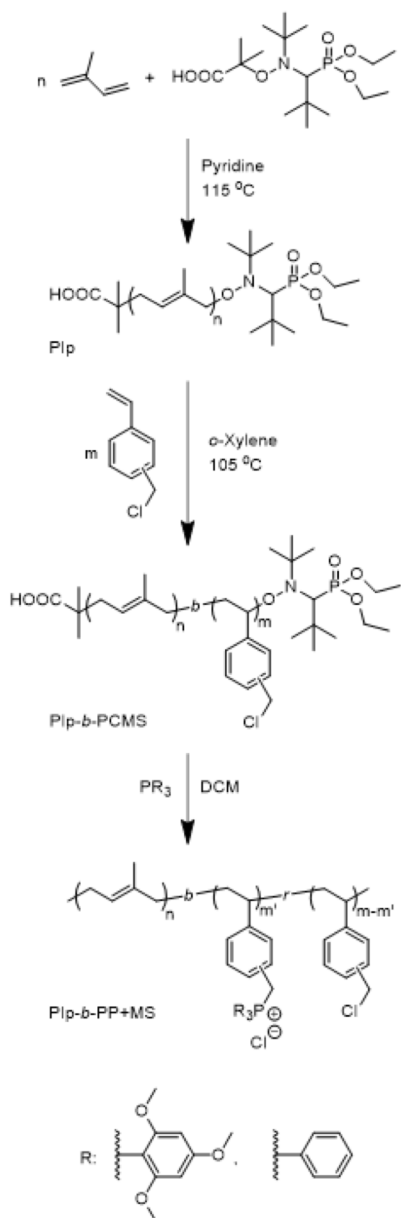
dispersity ($Đ_{PIp}$ < 1.2), as shown in Table 1. The conversion can also be calculated from ^{1}H

NMR to be ~50% after 14 hours of reaction time. Molecular weights were determined by

GPC using THF as solvent against polystyrene standards.

The macro-initiator, PIp-SG1, was then chain extended with CMS in *o*-xylene. By

changing the feeding ratio of CMS and PIp-SG1, molecular weight of the second block,

PCMS, could be tuned. From ^{1}H NMR, the integration of the alkene peak from PIp (δ: 4.9-

5.1 ppm, CDCl$_3$) was normalized to 1, while peaks from the aromatic ring (δ: 6.1-6.6, 6.6-

7.1 ppm, CDCl$_3$) and benzylic position (δ: 4.2-4.5 ppm, CDCl$_3$) were integrated and

averaged to calculate the DP ratio between PCMS and PIp. Due to fast propagation rate of

NMP, ~80% conversion of CMS was achieved within short reaction time (10 h) and high

degree of polymerization (DP) of CMS was easily obtained. GPC traces were analyzed

using the same polystyrene standards. The benzylic site of CMS is prone to transfer

reactions because of possible conjugation with the aromatic ring.[144] Thus, side reactions

could result in increased dispersity.

Block copolymer PIp-PCMS was then quaternized by P(Ph(OMe)$_3$)$_3$ or P(Ph)$_3$, using

DCM as solvent. The solution was purged by nitrogen in advance to inhibit the oxidation of

phosphine during quaternization. The reaction was conducted at 50 ℃ for three days, then

quenched by precipitation in methanol. From ^{31}P NMR, peaks from phosphine oxide or

excess quaternization agent were not observed. From our previous study, the quaternization

efficiency for the traditional quaternization agents, P(Ph(OMe)$_3$)$_3$, was ~30%.[145] Whereas

the quaternization efficiency of P(Ph)$_3$ is close to 100%, indicated by full disappearance of

the peak from PCMS benzylic position in ^{1}H NMR (Figure 5.1). Thus, quaternization

efficiency of 30% and 100% were used to calculate the theoretical IEC for P(Ph(OMe)$_3$)$_3$

and P(Ph)$_3$, respectively.
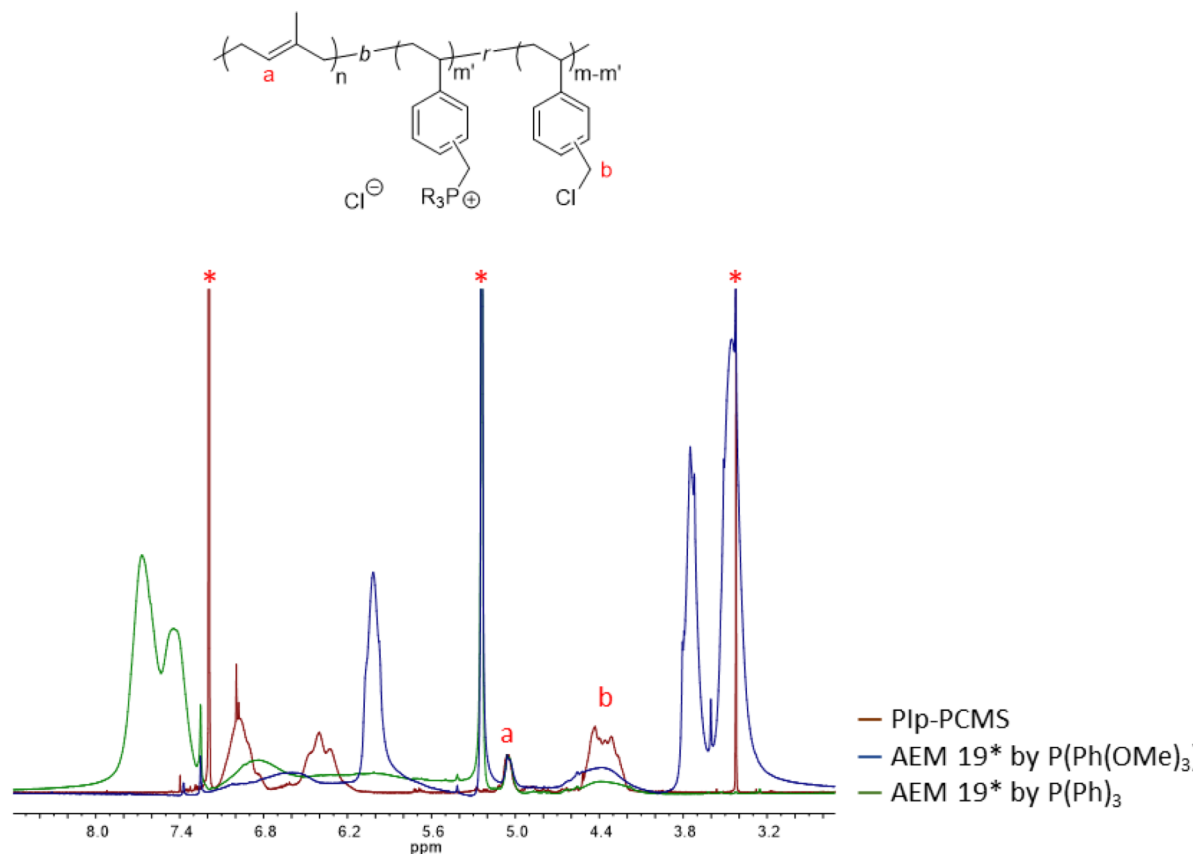
Figure 5.1: ^{1}H NMR spectra of precursor neutral block copolymer PIp-PCMS and neutral-charged block copolymer AEM 19* PIp-P(R$_3$P$^+$)MS, quaternized by P(Ph(OMe)$_3$)$_3$ and P(Ph)$_3$ respectively.

After quaternization, the polymer solution was drop cast from chloroform solution onto a clean polytetrafluoroethylene sheet and left to dry. The membranes were then exposed to saturated THF vapor for solvent annealing for 24 hours, resulting in transparent and uniform films ~5 μm thick.

Table 5.1: Chemical composition and bulk morphology of PIp-P(R$_3$P$^+$)MS synthesized by NMP

AEM	PIp		PIp-PCMS			PIp-P(R$_3$P$^+$)MS, R = Ph(OMe)$_3$			PIp-P(R$_3$P$^+$)MS, R = Ph		
	$M_w{}^a$ (g/mol)	$Đ^a$	$M_w{}^a$ (g/mol)	$Đ^a$	f (%)^b	IEC^c (mmol/g)	d-spacing^d (nm)	M^d	IEC^c (mmol/g)	d-spacing^d (nm)	M^d
16	62,000	1.15	89,000	1.35	80	0.87	20	C	2.24	22	C
17			110,000	1.34	82	0.88	23	C	2.26	24	C
18	9,400	1.14	28,000	1.89	88	0.91	41	S	2.31	43	S
19			29,000	1.84	92	0.93	70	S	2.35	72	S

^{a}Weight-average molecular weight (M_w) and dispersity ($Đ$) of the polymers from THF GPC.

^{b}Volume fraction of PCMS block, calculated by DP from ^{1}H NMR and the densities of homopolymers.

^{c}Theoretical ion exchange capacity (IEC) of the copolymer PIp-P(R$_3$P$^+$)MS, calculated from ^{1}H NMR.

^{d}D-spacing and morphology inferred from SAXS, where C denotes cylinder and S denotes sphere.

D. Quaternization Agent Size Effect on Morphology

The influence on bulk and surface morphologies were investigated by SAXS and AFM for comparison of the two quaternization agents. As discussed above, P(Ph(OMe)$_3$)$_3$ has a lower quaternization efficiency, due to the steric hindrance of nine methoxy groups on the benzene rings, while P(Ph)$_3$, a less bulky counterpart, has a higher quaternization efficiency for the same reaction time. The quaternization efficiency difference directly results in a two-fold increase in IEC, as shown in Table 3.1. In terms of their morphological effect, the SAXS profiles of AEM 16 quaternized by P(Ph)$_3$ and P(Ph(OMe)$_3$)$_3$ are shown in Figure 1A as an

example, where the primary peak position allows us to determine the d-spacing and peak positions of higher order peaks relative to the primary peak indicates bulk morphology. Figure 5.2B shows the repulsive-mode phase images of the two membranes by AFM, which reveals surface morphology. Bright contrast in the phase images is assigned to the hydrophilic domains. Despite such a large difference in IEC, membranes from both quaternization agents show cylindrical morphology. A small shift towards ~2nm larger d-spacing was observed in P(Ph)$_3$ from SAXS, as well as larger cluster size in AFM, than those of P(Ph(OMe)$_3$)$_3$.
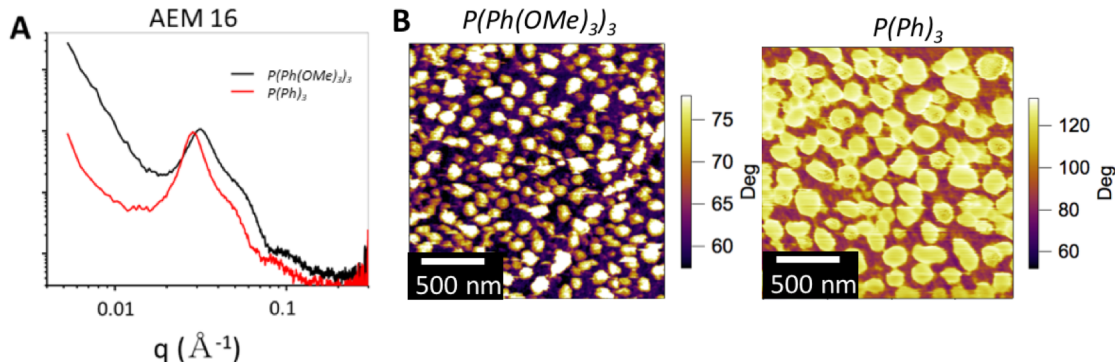
Figure 5.2: (A) SAXS comparison of AEM 16 as-received and quaternized by P(Ph(OMe)$_3$)$_3$ in black trace and P(Ph)$_3$ in red trace. (B) Phase images of P(Ph(OMe)$_3$)$_3$ and P(Ph)$_3$, respectively. Bright phase contrast is assigned to the hydrophilic domains. The phase contrast is discussed in the Experimental section.

E. Quaternization Level and Morphology

In order to evaluate the impact of quaternization level (QL) on phase behavior of PIp-P(R$_3$P$^+$)MS, a range of QL was achieved by partial quaternization of AEM 17 with P(Ph)$_3$. The QL was altered by adjusting the reaction stoichiometries of P(Ph)$_3$ to PIp-PCMS. Quaternization were performed with ratios of P(Ph)$_3$ to PIp-PCMS of 1:4, 2:4, 3:4 and 4:4, as well as with a two-fold excess of P(Ph)$_3$ to ensure the highest QL. They are noted as *0.25_P, 0.5_P, 0.75_P, 1_P* and *full_P,* respectively, while the un-quaternized membrane of

AEM 17* was denoted as *0_P*, as listed in Figure 5.3A. The QL gradient was confirmed by ^{1}H NMR. The peak from PIp was normalized by area, gradual decrease of the peak from benzyl chloride positions on PCMS and increase of the peaks from phosphonium phenyl positions were observed. For *full_P* sample, the complete absence of the benzyl chloride peak indicates the QL is close to 100%.
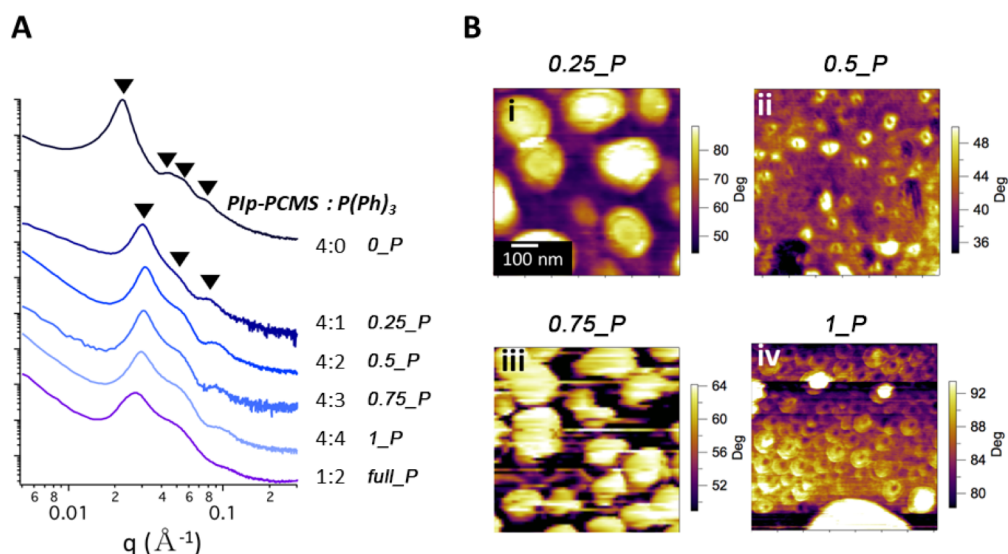
Figure 5.3: (A) SAXS of un-quaternized and partially quaternized AEM 17. (B) Phase images of AEM 17 (i) *0.25_P*, (ii) *0.5_P*, (iii) *0.75_P*, and (iv) *1_P*.

With an increase in QL, cylinder morphology was maintained throughout all membranes with peaks located at q, $2q$, $\sqrt{7}q$, and $3q$ for *0_P* and q, $\sqrt{3}q$ and $\sqrt{7}q$, for *0.25_P - full_P*. The absence of $\sqrt{3}q$ in *0_P* followed by its appearance after quaternization might indicate some degree of morphology change. The attenuation of the 2q peak in cylinder morphologies for PIp-P(R_3P^+)MS is typical and likely due to the form factor cancelling out the structure factor.[131]

A decrease followed by a subsequent increase in d-spacing was observed with increasing QL. The trend was supported by the repulsive mode phase images of *0.25_P, 0.5_P, 0.75_P,* and *1_P* shown in Figure 5.3B, with domain size changing accordingly.

A small loading of charges in *0.25_P* resulted in a drastic d-spacing decrease from 28 nm in *0_P* to 21 nm. The onset of electrostatic cohesion lowers the separation distance between PCMS chains, illustrated by the cartoon in Figure 5.4. D-spacing further decreased to 20 nm in *0.5_P*, which is likely due to the two reasons: first, the Columbic cohesion between the chloride counterions and phosphonium cations drives the ionic phase tightly packed, while the distance between two phosphonium cations is sufficiently far apart to avoid repulsion. Second, the QL could also affect the separation distance in a way similar to triblock architectures. At low QL, the quaternized $P(R_3P^+)MS$ would behave as a third block with high χ_N. This pseudo triblock copolymer, *0.5_P,* can undergo chain frustration, as the ionic block tend to form continuous phase while the two other neutral moieties, PIp and PCMS, were forced to mix.

Upon further increasing QL from *0.5_P* to *full_P*, a monotonic increase in d-spacing was observed, shown both in SAXS and AFM in Figure 5.3. It is likely due to following reasons: first, steric repulsion from bulky phosphonium ions leads to the size increase of the ionic domains, as depicted in Figure 5.4. Second, as more charges were installed onto polymer backbone, the distance between two phosphonium cations greatly decreased. Due to the Columbic repulsion between adjacent charges, polymer chains were more extended, resembling the behavior of rod-like polyelectrolyte, which resulted in d-spacing increase.
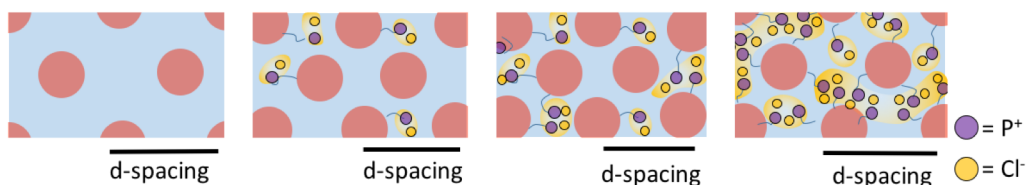
Figure 5.4: Cartoon illustration of d-spacing vs. QL dependency.

Similar electrostatic interaction induced non-monotonic change was predicted in a computational study of lamellar block polyelectrolyte by Sing *et al.*, where the dependence of lamellar d-spacing on charge fraction was investigated via SCFT-LS calculation. For weak Coulombic interactions, the introduction of charge decreases d-spacing; while for stronger Coulombic interactions, charge introduced into the block polyelectrolyte has the opposite effect of increasing d-spacing.[131]

F. Bulk vs. Surface Morphology

Representative membranes of low (AEM 13), moderate (AEM 17) and high (AEM 18) IECs, quaternized by $P(Ph(OMe)_3)_3$, were investigated by SAXS, TEM and AFM for bulk and surface morphology characterization. AEM 13 was a previously synthesized diblock copolymer with IEC of 0.44 mmol/g,[138] while AEM 17 and 18 were synthesized in this study with IEC of 0.88 and 0.91 mmol/g, respectively. Bulk morphologies were inferred from SAXS (Figure 5.5A-C), further confirmed by cross-sectional TEM (Figure 5.5D-F). Prior to TEM, membranes were microtomed and stained by OsO_4, which selectively stain olefin.[131] Thus, dark contrast in Figure 5.5D-F corresponds to the PIp and bright corresponds to the ionic $P(R_3P^+)MS$ block.

For AEM 13, the d-spacing was 42 nm and shows peak positions at q, $\sqrt{3q}$, $\sqrt{7q}$,

indicating cylinder morphology (Figure 5.5A). Both short-range parallel and perpendicular

cylinders were observed (Figure 5.5D). The cylinder morphology was also observed for

AEM 17*, with d-spacing of 23 nm. The decrease in d-spacing is supported by TEM in

Figure 5.5E, where smaller and more tightly packed hydrophobic cylinders were observed.

An average diameter of the hydrophobic aggregates in TEM of AEM 17 was measured to be

~20 nm. Upon further increase in IEC, AEM 18 exhibits a spherical body-centered cubic

(BCC) morphology with d-spacing of 41 nm, indicated by peak positions of q and $\sqrt{6q}$.

Less ordered morphology was observed in Figure 5.5F, where hydrophobic domains were

loosely packed. Despite the increase in IEC, the hydrophobic domains increased in size. The

average diameter of the hydrophobic domains was 30 nm, which is in agreement with the d-

spacing. Modelling of neutral polyisoprene-polystyrene diblock (PIp-PS) copolymer

($\chi_N \gg 10$) has shown that a spherical morphology is expected for polystyrene volume

fractions > 0.77.[146,147] Zhang *et al.* has suggested that a large χ_N exists in our PIp-

$P(R_3P^+)MS$ membranes given that well-ordered morphologies were achieved despite low

degree of polymerization.[148]

Surface morphology and relevant sizes of the hydrophilic and hydrophobic surface

domains were revealed by AFM (Figure 5.5G-I). AFM images were gathered in tapping-

mode. The phase images, shown in 5.5G-I, were used for our analyses because the contrast

provides a chemical map of the ionic and hydrophobic domains.[131] Phase deviations depend

on whether the tip-sample interactions are attractive (>90°) or repulsive (<90°).[23,24] All of

our phase images were gathered in repulsive mode. Tip-sample power dissipation is related

to the sine of the phase angle, hence phase deviations toward 90° in both attractive and

repulsive-mode imply maximum power dissipation.[24] In Nafion, the hydrophilic domains are more compliant than the semi-crystalline Teflon-like matrix, hence assigning phase contrast to the ionic domains is apparent.[25] In this investigation, however, the hydrophobic PIp block has a low T_g and is more compliant than the $P(R_3P^+)MS$ hydrophilic block, thus complicating interpretations. Nevertheless, through careful analysis of the size and frequency of the bright clusters in repulsive mode phase images upon increasing quaternization (shown in Figure 5.3B), we have assigned the bright contrast to be the hydrophilic domains.
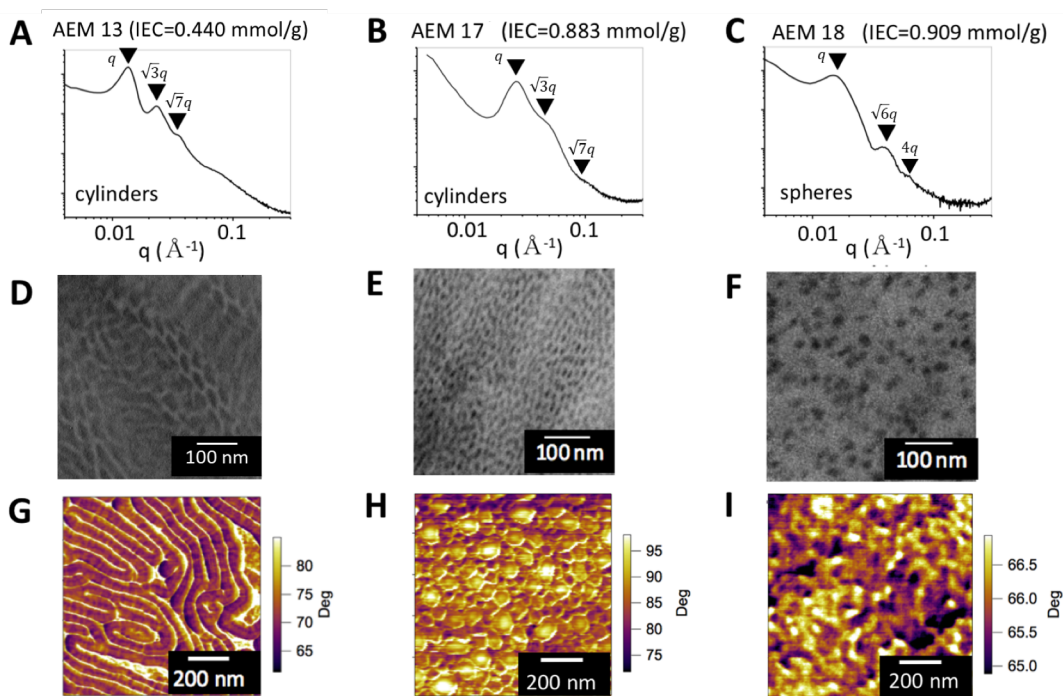
Figure 5.5: (A-C) SAXS, (D-F) TEM, and (G-I) AFM phase of AEM 13 (A, D, G), AEM 17 (B,E,H), AEM 18 (C,F,I). Dark contrast in TEM and AFM is the hydrophobic domains.

Interestingly, different surface alignments were observed for our two cylinder-morphology membranes, AEM 13 and 17. For AEM 13, cylinders were observed to align parallel to the surface of the membrane (Figure 5.5G), despite perpendicular bulk alignment

shown by TEM. Nevertheless, perpendicularly aligned domains are observed in AEM 17 with moderate IEC (Figure 5.5H), resembling the cylinder morphology in TEM. Similar phenomenon for PS-PIp diblock copolymer with a PS volume fraction of 52% was observed by Hasegawa et al.,[24] where PIp block tends to cover the surface regardless of microdomains aligned in bulk. Cross-sectional AFM imaging was used by Komura et al. to show the difference in surface alignment of cylinders of PEO-PMA(Az) membranes.[149] In addition, Khanna et al. observed parallel alignment of lamellar sheets for polycyclohexylethylene-polyethylene (PCHE-PE) diblock polymer films and the author noted that PE, with lower surface tension, preferred to orient toward surface and lay parallel.[143,150] Furthermore, upon increasing the volume fraction of PCHE, the surface domains formed perpendicular to the surface. Although the Coulombic interactions can influence the morphology in charged block copolymers,[151] we suggest that a similar phenomenon is taking place for our PIp-$P(R_3P^+)MS$ membranes in which the volume fraction of PIp plays an important role for the alignment of domains and difference in surface tension between the PIp and $P(R_3P^+)MS$ blocks can account for the surface alignment.

In terms of domain size and spacing, larger domains on the surface were observed than in the bulk for both AEM 13 and 17. By taking line profiles perpendicular to the cylinder, cylinder width of AEM 13 is measured to be ~40 nm and spacing between cylinders was ~17 nm (Figure 5.5D). The d-spacing measured by the power spectral density (PSD) was 72.5 nm, shown in the Figure 5.6A. As for AEM 17, the bright clusters, interpreted as the ionic domains, are 50-70 nm in diameter, nearly twice as large as domains in the bulk. The d-spacing by PSD analysis was 126.0 nm. Size discrepancy of ionic domains between the surface and bulk can be resulted from phase rearrangement occurred at the air-membrane

interface during membrane casting process. In Nafion, ionic domains are ~4 nm in diameter in the bulk[135] while ~10 nm in diameter on the surface.[19] Similarly, a combination of water adsorption by the ionic domains and the segmental motion of the PIp block can account for such a rearrangement.

1. Mathematical Background of Power Spectral Density Analysis

The power spectral density (PSD) is a statistical method that determines the distribution of frequencies from a time-varying signal. This method is significant because the frequencies of the signal are distinguished from the background noise.
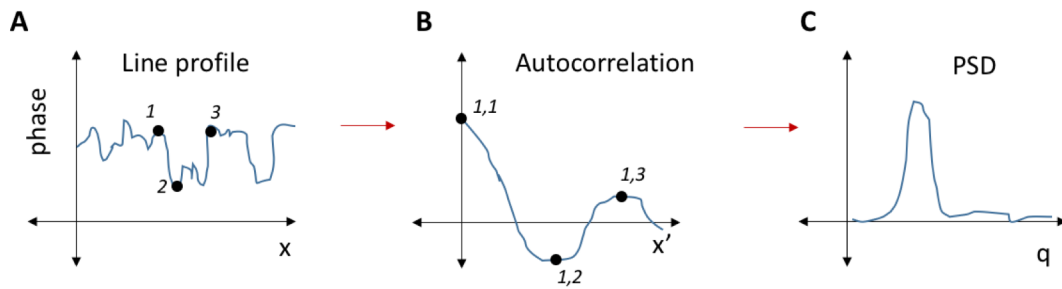
Figure 5.6: Sketched 1-D (A) line profile from AFM phase image, (B) autocorrelation function (ACF) and (C) the power spectral density (PSD) of the 1-D line profile. 3 example points are highlighted in Figure 5.6A. In Figure 5.6B, (1,1) represents the autocorrelation between the phase at point #1 and point #1, (1,2) represents the autocorrelation between the phase at point #1 and point #2, (1,3) represents the autocorrelation between the phase at point #1 and point #3.

Figure 5.6 illustrates a 1-dimensional case of a line profile of an AFM phase image and shows how the line profile and the PSD are related. According to Wiener-Khinchin theorem, the PSD is a Fourier transform of the autocorrelation function (ACF) of the line profile. The 1D discrete autocorrelation function is defined as:

$$r_{xx}(x') = E(x_n \overline{x_{n+x'}}) \tag{5.1}$$

Where x_n is a phase value along the line profile. $x_{n+x'}$ is another phase value on the line profile with a "lag" of x'. The PSD is then defined as:

$$S(f) = \sum_{x'=-\infty}^{\infty} r_{xx}(x')e^{-i(2\pi f)x'} \tag{5.2}$$

The ACF describes the correlation between two values of the line profile as a function of the length between them. In Figure 5.6A, 3 points are shown on the line profile graph. 3 corresponding points are shown in the ACF of Figure 5.6B. Point (1,1) in 5.6B shows the autocorrelation between point #1 and itself on 5.6A. Point (1,2) in 5.6B shows how the autocorrelation would appear negative between point #1 and point #2. The phase values between these points are significantly different and hence anti-correlated (or negative). Point (1,3) shows the autocorrelation between point #1 and point #3. These phase values are similar and positively correlated. This distance between point #1 and point #3 is also called the correlation length.

While this is a relatively simple example, our AFM images often show periodicity on multiple length scales. Additionally, it can useful to distinguish the correlation in the fast scan direction (x-direction) vs. the slow scan direction (y-direction). For example, if there are streaks in the image, one might detect a shorter range correlation in the x-direction than the y-direction. Therefore, taking the Fourier transform of the ACF provides a distribution of frequencies. In the illustrated example of 5.6, the ACF is periodic so there exists only 1 peak, where the peak position corresponds to the average separation distance between two features in the line profile.

The same mathematical procedure can be applied to 2-dimensional AFM images. An example phase image of a Fumatech AEM is shown in Figure 5.7A. The white line shows the average distance between two hydrophilic domains. The radially-averaged PSD in 5.7B.

91

The PSD were measured in Gwyddion, although one could easily write their own code, which does the same thing. I chose this software because it is free, user friendly, and is specifically designed to analyze AFM images for this purpose.
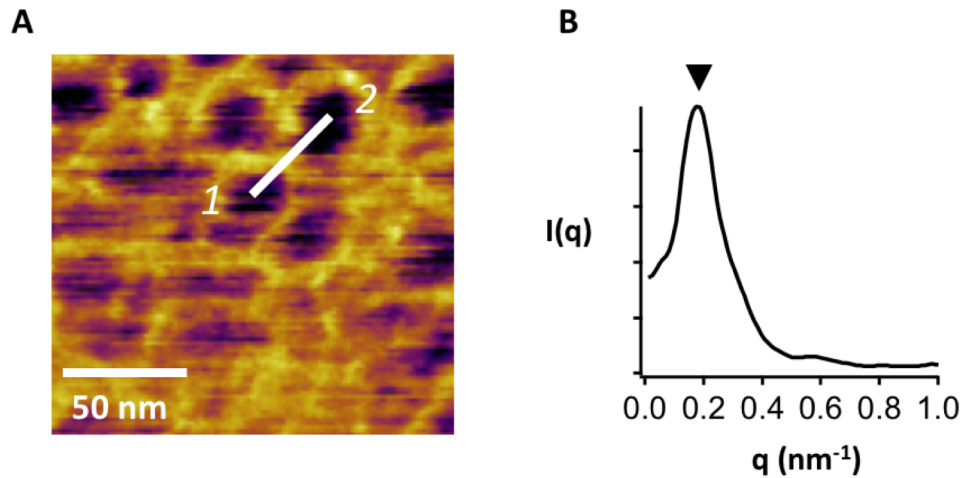
Figure 5.7: (A) An attractive-mode phase image of a Fumatech AEM and (B) its radially-averaged PSD. The most intense peak in the PSD represents the average separation distance between two neighboring domains.

Figure 5.8 shows PSDs of AEM 13, AEM 17, and AEM 18. The primary and higher order peak positions are labelled. The position of the higher order peaks relative to the primary peak indicates the morphology. The magnitude of the reciprocal lattice vectors can be derived for lamellar and hexagonal close packed (HCP) unit cells. For lamellar unit cell:

$$q = \frac{2\pi}{d_{hkl}} \tag{5.3}$$

While for an HCP unit cell:

$$q = \frac{4\pi}{d_{hkl}\sqrt{3}} \tag{5.4}$$

The d-spacing for a lamellar unit cell:

$$d_{hkl} = \frac{a}{\sqrt{h^2+k^2+l^2}} \tag{5.5}$$

and hexagonal is defined as:

$$d_{hkl} = \frac{1}{\sqrt{\frac{4h^2+hk+k^2}{3a^2}+\frac{l^2}{c^2}}}$$ (5.6)

a is defined as the lattice spacing parameter and c is the height of the cylinder. In a lamellar

(one-dimensional) lattice, (hkl)=(100), (200), (300),… are the allowed miller indices,

therefore relative Bragg peaks of 1, 2, 3… would be observed. In hexagonal, the allowed

(hkl) are when $h + 2k \neq 3n$ and when l is even, therefore relative Bragg peaks of 1, $\sqrt{3}$,

$\sqrt{4}$, $\sqrt{7}$, $\sqrt{9}$, $\sqrt{12}$.
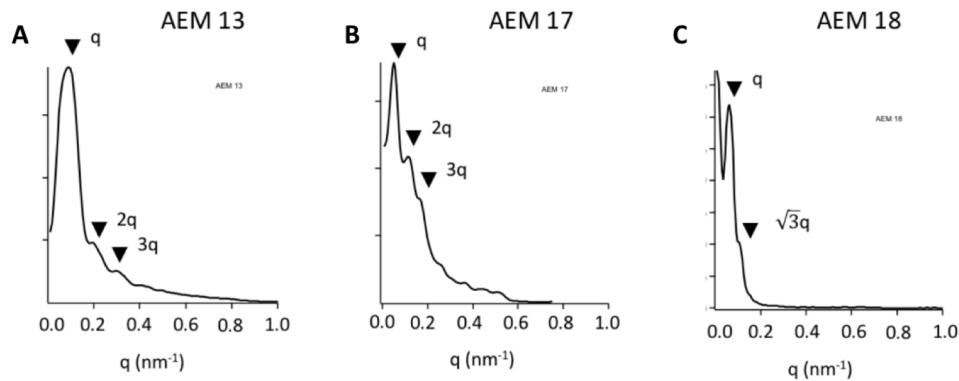
Figure 5.8: PSDs of AEM 13, AEM 17, and AEM 18 of the phase images from Figure 5.5G-I.

In both AEM 13 and AEM 17, the higher order peaks signify lamellar periodicity. In

AEM 18, the higher order peak signifies a hexagonal morphology, however this peak is less

pronounced, which explains why the image appears disordered.

For AEM 18, poorly ordered morphology was observed, where spheres were loosely

packed (Figure 5.5I), resembling the TEM. The disagreement between the results inferred

from SAXS and TEM of AEM 18 (Figure 5.5C and 5.5F) while qualitative similarities

between the AFM and TEM images (Figure 3.5F and 3.5H) is peculiar. Typically, BCC forming membranes exhibit diffraction peaks at $1q$, $\sqrt{2q}$, $\sqrt{3q}$, $\sqrt{4}q$, … The broad higher order peak at $\sqrt{6}q$ could infer a liquid-like short range order with lack of true long range order of BCC membranes.[24] Average diameter of bright ionic domains was measured to be ~25 nm and that of dark hydrophobic domains was ~40 nm. The d-spacing by PSD was 100.1 nm.

The higher order peaks of the PSDs were used to investigate the ordering behavior at the surface of the membrane. These peaks are much lower in intensity than the primary peak, which implies a loosely ordered surface structure. In AEM 13 and 17, the higher order peaks are positioned q, 2q, and 3q, which signifies lamellar ordering. AEM 18 has higher order peaks positioned at q, and $\sqrt{3}$q, which signifies hexagonal ordering.

G. Humidity-Dependent Morphology in Bulk

In the membrane, the ionic phase is hydrophilic and PIp phase is hydrophobic. The hydrophilicity of the membranes can lead to humidity responsive phase behavior. Thus, the humidity-dependent bulk morphologies of two membranes with different morphologies and IECs were investigated by SAXS.

Prior to the SAXS measurement, AEM 13 and AEM 19, quaternized by P(Ph(OMe)$_3$)$_3$, were equilibrated in a RH-controlled environment for 1h. SAXS was first collected under dry conditions (<5% RH, black trace), then 95% RH (red trace). As shown in Figure 5.9A and 5.9B, the presence of higher order peaks under both RH conditions indicates that the ordered morphologies were maintained throughout dry to humid conditions for both AEMs. Nevertheless, d-spacing shift of ~0.6 nm was observed in AEM 13, between

dry and 95% RH, whereas a larger shift in d-spacing of ~8.0 nm for AEM 19 was observed.

The minimal morphological change in AEM 13 with lower IEC could be due to low degree

of water uptake inherent to bulky QP pendant polymers.[152,153] Although AEM 13 has a lower

IEC than AEM 19, the difference in orientation of the surface domains could also influence

the swelling behavior. For example, the surface of AEM 13 consists of parallel hydrophobic

PIp cylinders, which could shield more water from adsorbing than domains that would be

perpendicularly aligned.
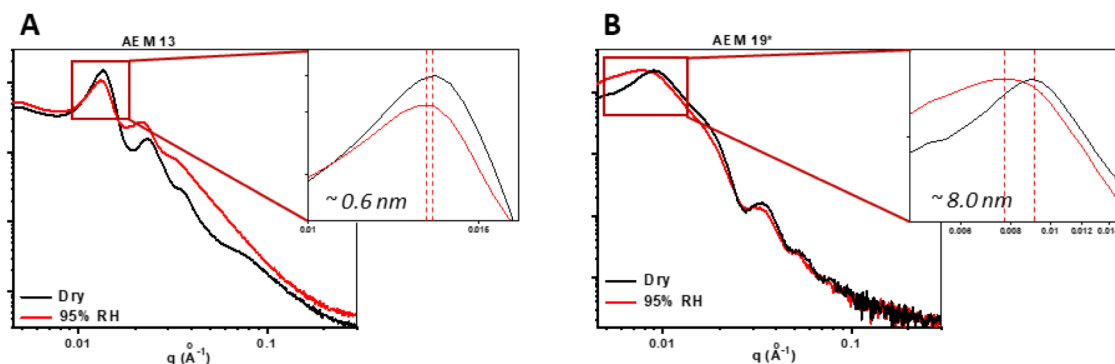
Figure 5.9: SAXS of (A) AEM 13 and (B) AEM 19 under dry (black trace) and 95% RH (red trace). The dashed red lines mark the peak position shift between dry and 95% RH.

Control experiments were performed on of two partially quaternized AEM 17

membranes with different QL (*0.25_ P* and *1_P*) at dry and 95% RH shown in Fig. 5.10.

Both membranes consist of perpendicularly aligned cylinders. SAXS of (A) AEM 17 *0.25-P*

and (B) AEM 17 *1-P* after 3 humidity cycles. The intensity on y-axes has been manually

offset for clarity. First of all, similar to IEC dependent d-spacing change observed in AEM

13 and AEM 19, AEM 17-*0.25P*, with lower QL and IEC, received a constant d-spacing

shift of 0.6 nm in each cycle, whereas *1-P* showed a shift of 1.3 nm. Thus, IEC-dependent d-

spacing change applies to either fully or partially charged polymer as well as both

quaternization agents. Second, higher order peaks were still visible under 95% RH, which

means phase separation was maintained. And both *0.25-P* and *1-P* show that the shift in d-

spacing between each humidity cycle was constant, marked by the dashed red lines in Fig.

5.10, indicating good reversibility of both membranes. Although higher IEC leads to more

drastic morphology change, but water uptake and loss are hydrodynamic reversible process,

independent of IEC.
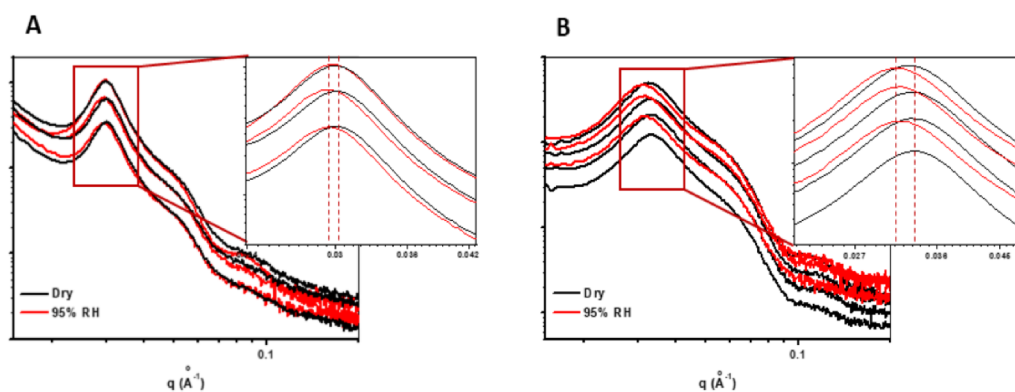
Figure 5.10: SAXS for AEM 17 (A) *0.25-P* and (B) *1-P* for 3 humidity cycles for dry-95% RH.

H. Humidity-Dependent Surface Morphology

Phase imaging of ion exchange membranes at controlled environmental conditions is a

useful tool in observing changes in surface morphology as a result of changes in RH.[42,129]

Figure 5.11 provides a comparison of repulsive mode phase images of AEM 13, AEM 16,

and AEM 19, quaternized by $P(Ph(OMe)_3)_3$, at a wide range of RH.

With the lowest IEC (0.44 mmol/g), AEM 13 showed no significant change in

morphology, only differences in spacing. The spacing between cylindrical aggregates

measured by line profiles from Figure 3.8A-C was 14 nm at 18% RH, 17 nm at 50% RH, and 23 nm at 80% RH. The d-spacing was calculated by measuring the peak position in the power spectral density (PSD) of images 3.8A-C. An increase in d-spacing with increasing RH was observed: 31 nm at 18% RH, 61 nm at 50% RH, and 65 nm at 80% RH.

Followed by AEM 16 with cylinder morphology at an IEC of 0.87 mmol/g, under dry conditions (Figure 5.11D), the absence of bright ionic domains indicates a less ordered morphology. The phase image in 5.11E at 50% RH resembled a similar morphology of that shown in 5.5H.
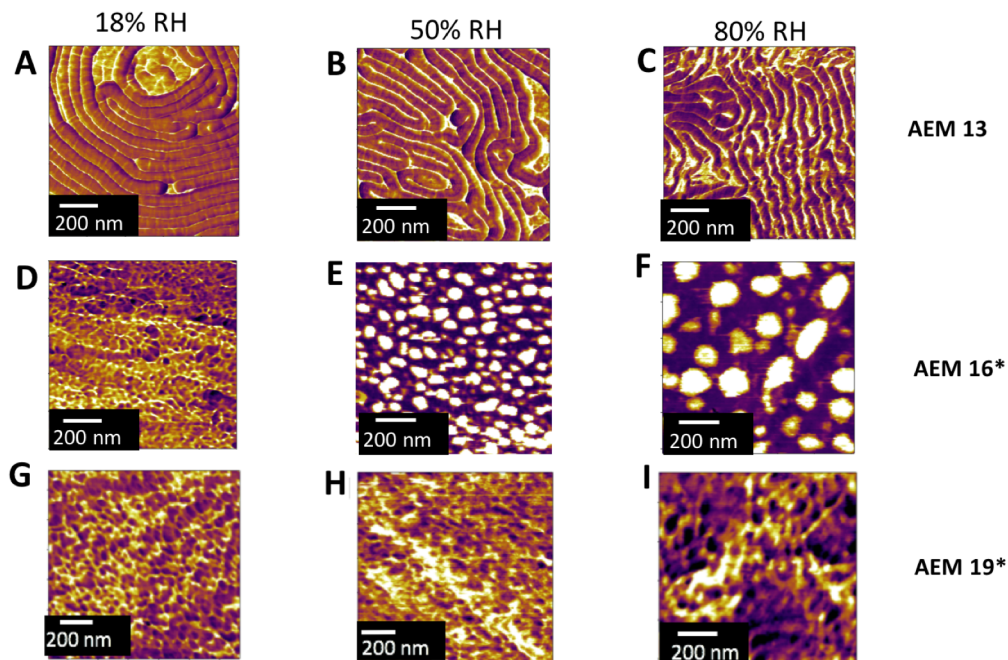
Figure 5.11: (A-I) Repulsive mode phase images of AEM 13 (A-C), AEM 16 (D-F), and AEM 19 (G-I) under 18% (A,D,G), 50% (B,E,H), and 80% RH (C,F,I).

The bright ionic domains were not as closely packed as AEM 17 likely due to the difference in IEC. The average diameter of the domains in 5.11E are 42 nm with 16%

coverage. At 80% RH, domain size increased in which the average diameter is 59 nm with 10% coverage (Figure 5.11F).

Upon further increasing IEC, AEM 19 showed a similar disordered morphology as AEM 18 in 5.5I. We've interpreted regions of dark contrast as the hydrophobic domains given the striking qualitative similarity with TEM. Control experiments in which un-quaternized AEM 19 was imaged under ambient conditions and showed a similar morphology as shown in 5.5I. Under ambient conditions, the average diameter of the hydrophobic domain was 20 nm at 26% coverage. At hydrated conditions, phase contrast increased, indicating increasing water uptake by the continuous ionic phase. The hydrophobic domains increased in size to 38 nm with 30% coverage. The increasing size, although at a similar area coverage, can be due to stretching of the PIp block to accommodate increase in water uptake. At dehydrated conditions, the phase contrast between the hydrophilic and hydrophobic domains was lower. There was no change in size of the hydrophobic domains between ambient and dehydrated conditions, but the area coverage decreased to 20%. The surface, which displays a different morphology-humidity behavior than bulk, could be explained by increased chain flexibility near the surface that can more easily release internal stress.

I. Morphology Reversibility by Humidity Cycling

The morphological reversibility after cycling the RH was analyzed for AEM 13 by both AFM and SAXS. Small, but detectable changes in size and spacing of domains under dry and humidified conditions were observed as shown in Figure 5.12A-C. Excessive swelling was avoided in AEM 13, thus tip-sample contact could be maintained for a long period of time.
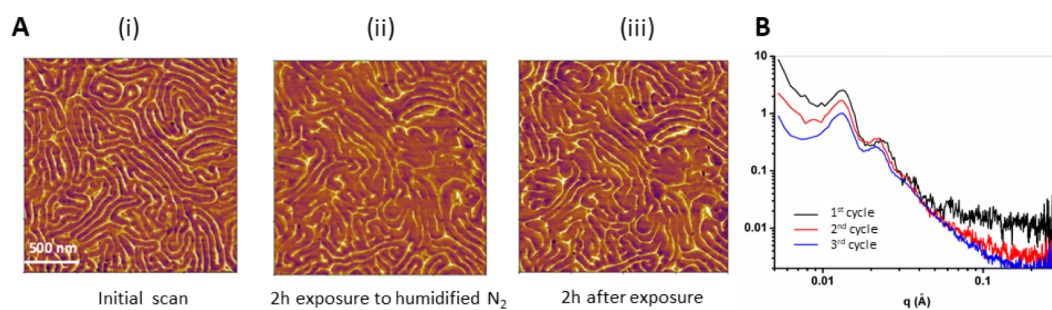
Figure 5.12: (A) SAXS of AEM 13 for 3 humidity cycles for dry-95% RH. (B) Repulsive mode phase images of AEM 13 at a fixed scan area for 1 humidity cycle ranging from 50 – 80% RH. (B-i) the first scan at 50% RH. (B-ii) after 2 h exposure at 80% RH. (B-iii) after 2 h drying and equilibrated at 50% RH.

Repulsive mode phase images of AEM 13 throughout one humidity cycle between ambient (50% RH) and humidified (80% RH) were collected in Figure 5.12A. The experiment was conducted in a closed humidity-controlled fluid cell. The first scan, shown in 5.12A-i, was conducted under ambient conditions. The parallel-aligned cylinder morphology is clearly shown, similar to 5.5G. Humidified N_2 was supplied to the fluid cell. After 2 h, equilibrium was reached and a second image, shown in 5.12A-ii, was collected. A decrease in the connectivity of the bright ionic regions was observed, which was a result of the swelling behavior. The humidified N_2 was then turned off. After 2 h, a third image, shown in 5.12A-iii was collected, where a gradual restoration of the initial scan can be observed. The d-spacing was also measured by taking the PSD of the images. The spacing showed an increase from 66 nm in 3.9A-i to 74 nm in 5.12A-ii and a subsequent decrease to 71 nm in 5.12A-iii.

In addition, Figure 5.12B shows SAXS of AEM 13 for three humidity cycles. Before the initial shot, AEM 13 was equilibrated in a humidity chamber with 95% RH over night at 40° C. The membrane was then dried under vacuum overnight before SAXS profile was

collected (first cycle in Figure 5.12B). This process was repeated for one/two times to obtain

SAXS after second/third cycles in Figure 5.12B. Although a shift in d-spacing of ~0.6 nm

was observed between dry and 95% RH cycles (Figure 5.9A), 5.12B shows no drift in d-

spacing between cycles, which indicates that the expansion and contraction of channels

between the humidified and dry conditions are thermodynamically reversible states.

J. Morphology of a Random Statistical Copolymer AEM

Nafion is the benchmark PEM because of its high conductivity and mechanical strength,

however, due to the random statistical nature, its morphology has been heavily debated.

Block copolymer architectures are intriguing because the morphology can be tailored.

Therefore, the transport properties can be studied in a reliable fashion. A question we were

interested in addressing was: Do ordered block copolymer AEMs given rise to improved

ionic connectivity over random copolymer AEMs at similar IEC? Elabd *et al.* showed

improvements in proton conductivity of sulfonated triblock copolymer PEM over Nafion, as

well as highlighted the impact of morphological transitions on conductivity.[154] Tanaka *et al.*

investigated a quaternized multiblock poly(arylene ether) and showed improved hydroxide

conductivity over the random copolymer at similar IEC.[155] To our knowledge, there has

been no reports investigating the comparison of phosphonium-containing AEMs, thus we

turned our attention to investigate the morphology of a random statistical copolymer PIp-

P(R_3P^+)MS (AEM-*r*) in comparison to our previously studied diblock copolymer AEMs. It

should be noted that the following data is preliminary and random copolymer AEMs with a

range of IECs should be investigated in the future.

AEM-*r* was synthesized by a random copolymerization of PIp and PCMS via NMP then quaternized by P(Ph(OMe)$_3$)$_3$. The IEC of AEM-*r* was determined theoretically from NMR to be 0.35 mmol/g, which has a comparable IEC to AEM 13. The membrane was cast from CHCl$_3$ onto a clean PTFE sheet for 24 hours, then peeled off prior to SAXS and AFM.
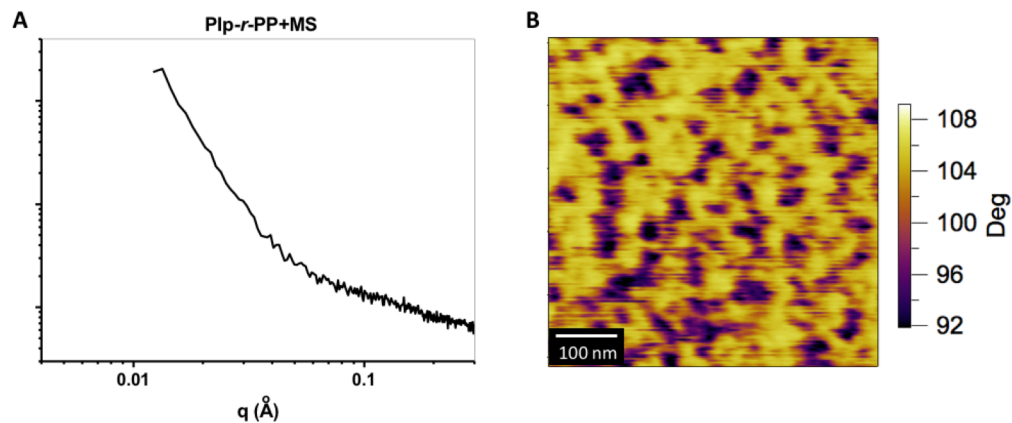
Figure 5.13: (A) SAXS and (B) AFM phase image of a random statistical copolymer AEM.

Interestingly, SAXS revealed no apparent peaks shown in Figure 5.13A. This indicates the absence of phase-separated morphology. It is possible that a higher IEC is needed in order to observe the ionomer peak in our random copolymer systems. However, in AFM, large randomly dispersed hydrophilic domains (~30 nm in diameter) were observed. Due to these inconsistencies, other random copolymer AEMs with a range IECs should be synthesized and characterized. Furthermore, we also found the surface of AEM-*r* to be sticky during imaging, which led to streaks in the scan and frequent jumps between attractive and repulsive-mode.

K. Morphology of Triblock Copolymer AEMs

We then turned our investigation to phosphonium-containing triblock copolymer AEMs. Triblock chain architecture could have advantages over diblock in some cases as it allows for a higher IEC at the same morphology.[38] This could lead to improvements in conductivity without sacrificing the mechanical strength of the membrane. In a previous investigation by Zhang *et al.*, phosphonium low IEC triblock AEMs were synthesized.[38] The polymers consisted of PIp end-blocks with the quaternizable PCMS mid-block. SAXS revealed lamellar and hexagonal morphologies.
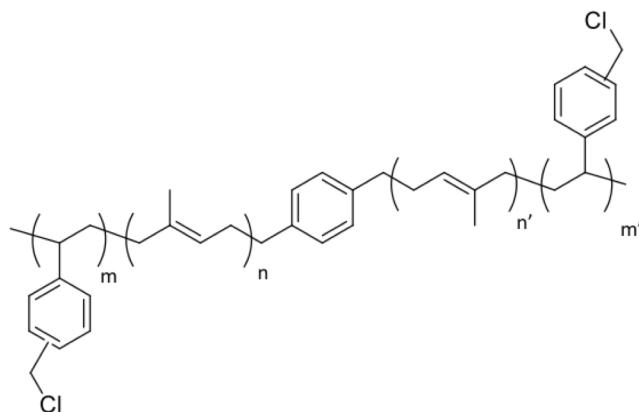
Figure 5.14: Chemical structure of an un-quaternized triblock copolymer AEM consisting of PCMS as the end-blocks and PIp as the midblock.

In this work, inverted triblock copolymers were synthesized consisting of PCMS end-blocks and a PIp mid-block. The polymers were synthesized via RAFT. Figure 5.14 shows the chemical structure of the un-quaternized polymer. We conducted SAXS and AFM of un-

quaternized AEMs. Future work detailing the change in morphology of the AEMs after quaternization still needs to be carried out.
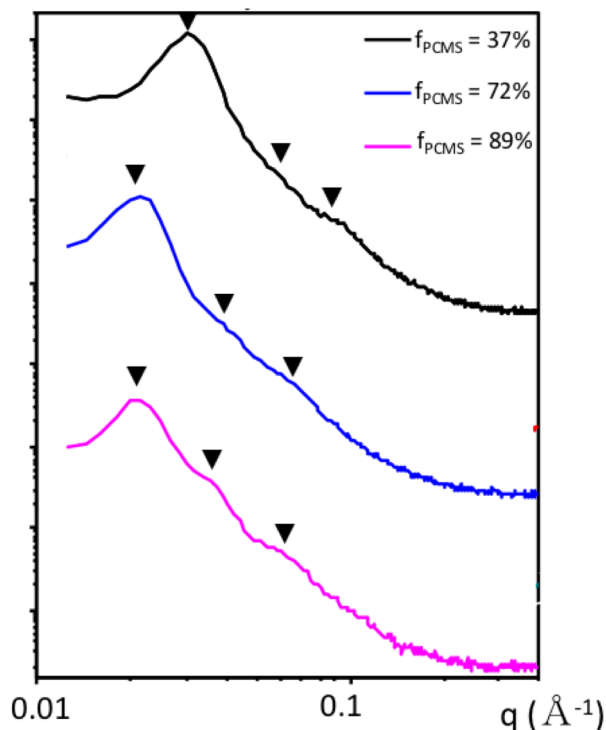
Figure 5.15: SAXS of 3 un-quaternized triblock copolymer AEMs at different volume fraction of the PCMS block (f_{PCMS}): 37% (black), 72% (blue), and 89% (magenta). The higher order peaks are labelled by black triangles. The positions of the peaks indicate a lamellar morphology for the black and blue curves, while they indicate a hexagonal morphology for the magenta curve.

SAXS of un-quaternized triblock copolymer AEMs at 3 different volume fractions of the PCMS block (f_{PCMS}) were measured shown in Figure 5.15. The black triangles indicate the positions of the higher order peaks. For $f_{PCMS} = 37\%$ (black) and $f_{PCMS} = 72\%$ (blue), the relative peak positions are q, $2q$, and $3q$, which indicates a lamellar morphology. For $f_{PCMS} = 89\%$, the relative peaks positions are q, $\sqrt{3}q$, and $\sqrt{7}q$, which indicates a hexagonal morphology. This data shows a similar trend with previous diblock copolymer AEMS in

which an increase in f_{PCMS} leads to a shift from lamellar morphologies to inverse

hexagonally packed PIp cylinders. However, a higher f_{PCMS} is needed for the transition from

lamellar to hexagonal morphologies in triblock membranes than the diblock membranes. It

was found previously that only a f_{PCMS} of ~22% for diblock membranes was needed

compared to ~72% for the triblock membranes. This signifies that the triblock membranes

could effectively triple the IEC at a lamellar morphology. On the other hand, this lowers the

PIp component, which lowers the flexibility and durability of the membrane.
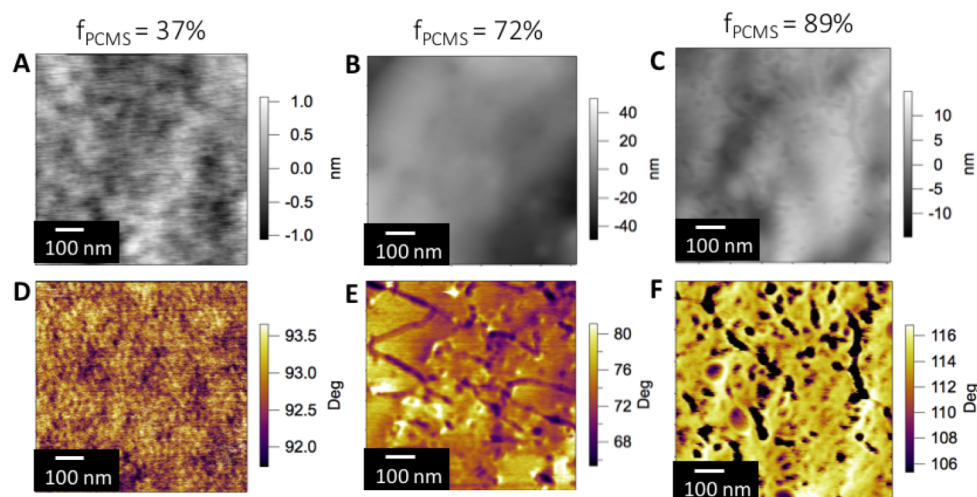
Figure 5.16: (A-C) Height and (D-F) phase images of un-quaternized triblock copolymer AEMs at (A,D) f_{PCMS} = 37%, (B,E) f_{PCMS} = 72%, and (C,F) f_{PCMS} = 89%.

We then compared these bulk scattering results with AFM to understand how the surface

morphology changes with respect to change in f_{PCMS}. Figure 5.16 shows height (top row)

and phase (bottom row). For volume fraction of 37%, a relatively flat surface was observed

in Figure 5.16A. We observed very little phase contrast in its corresponding phase image in

5.16D. It is likely that the PIp midblock is completely dominating the surface revealing none

of the PCMS component. We see an increase in the surface roughness for higher PCMS

volume fractions, possibly owing to the increased brittleness of the surface. At 72%, we found that we could not get the tip to engage in attractive-mode. Figure 5.16E shows a phase image in repulsive-mode. At 89%, however, we found that we could readily engage in attractive-mode as shown in Figure 5.16F. In both 5.16E and 5.16F, we found phase-separated domains consisting of a mixture of isolated circular domains and elongated domains. Give our previous knowledge on AEM 13, it is likely that we could be observing PIp domains laying parallel to the surface. However, there does not appear to be any ordering behavior on the surface as observed with the diblock AEMs. Furthermore, we were not able to assign the contrast of these phase images. It is likely that the dark contrast represents the PIp phase in un-quaternized membranes given that there is no hydrophilic component. Future experiments investigating the effect of partial quaternization could help assign the contrast in the phase images. In addition, future experiments are need to study the effect of spin-casting and solvent vapor annealing on the surface ordering of the triblock copolymers.

L. Conclusions

In summary, diblock copolymers PIp-PCMS were synthesized by NMP and quaternized by a tertiary phosphine. Membranes with a range of IECs were prepared and their morphologies were analyzed by SAXS, TEM, and AFM. Hexagonal cylinder and BCC morphologies were observed in PIp-P(R_3P^+)MS membranes, where the ionic block formed the continuous phase. Due to the difference in surface energy between two blocks, moderate IEC membranes showed parallel aligned channels on surface, while IEC increase induced perpendicular alignment, despite little difference in their bulk morphologies. The P(Ph)$_3$

exhibits higher quaternization efficiency, which leads to higher d-spacing and larger size of the ionic domains. By partial quaternization, the impact of QL on phase behavior of PIp-P(R$_3$P$^+$)MS was investigated. The Coulombic interactions and steric repulsion are collectively involved in accounting for the d-spacing change with increasing QL. The bulk and surface morphologies of PIp-P(R$_3$P$^+$)MS as a function of RH was studied, where IEC-dependent change in d-spacing and domain size has been established between dry and humid conditions. More significant change in the domain spacing on the surface was observed than bulk. Morphological reversibility of PIp-P(R$_3$P$^+$)MS membranes was examined by humidity cycling. Full morphology recovery was achieved after cycles of hydration and dehydration processes, which indicates that the expansion and contraction of channels as a function of RH is a reversible hydrodynamic process. From a fuel cell device point of view, the membrane-electrode interface has a significant impact on fuel cell overall performance. Detailed understanding of the correlations between the surface and bulk morphologies can shed light on developing important design principles for future AEM fuel cell membranes.

VI. Effect of Surface Alignment on Connectivity in Phosphonium Diblock Copolymer AEMs

Portions of this chapter are reproduced from:

A. Introduction

In this follow-up investigation from the previous chapter, we investigate how the alignment of the surface domains of the quaternary phosphonium-containing diblock copolymers influence the channel connectivity. Although it has been hypothesized that parallel alignment can impede charge transport at the membrane-electrode interface,[28] there has so far been no direct supporting evidence.

The connectivity of AEM 13 and 16, with different surface morphologies, were investigated by EFM. As a tapping-mode AFM based technique, EFM probes the electrostatic force gradient based on two-pass interleave scan. In the first pass, phase deviations depend on whether the tip-sample interactions are attractive (>90°) or repulsive (<90°).[40] Tip-sample power dissipation is related to the sine of the phase angle, hence phase deviations toward 90° in both attractive and repulsive-mode imply maximum power dissipation.[24] All of our phase images were gathered in repulsive mode. In the second pass, phase deviations are influenced by the electrostatic force gradient, which is attributed to surface charge, dielectric permittivity, and film capacitance. EFM has been used to

investigate the surface charge characteristics of isolated nanostructures[25] and structures embedded in thin films.[88,89,156,157] In Chapter 3, we demonstrated EFM to be a useful tool to study Nafion in which the disconnected dead-end channels embedded in fluorocarbon matrix were analyzed.[91,158] In this work, however, the EFM versus voltage bias response was analyzed of the conductive regions that represent the continuous surrounding phase with PIp cylinders embedded. The EFM versus voltage bias was compared between parallel-aligned PIp cylinders and perpendicularly-aligned ones. Supported by previously established models of isolated structures,[121] variation in EFM phase with respect to change in bias voltage is indicative of regions where charge is trapped due to discontinuity in the ionic phase. Thus, from different EFM responses as a function of bias voltage, the surface structures and connectivity can be evaluated. These findings provide direct evidence of the relationship between membrane preparation methods, morphology and channel connectivity, which in turn helps direct the synthesis and processing methods of these promising AEM materials.

B. Experimental

For drop-cast membranes, a solution of quaternized diblock copolymer, PIp-P(R_3P^+)MS, in chloroform (~50 mg/ml, 1ml) was drop-cast onto a clean polytetrafluorethylene sheet and allowed to dry slowly overnight. The membranes were then solvent-annealed by THF vapor for 24 h before being peeled off the substrate and dried under vacuum. The thicknesses of the membranes, measured by AFM, were ~ 6 μm. For spun-cast membranes, the solution of quaternized diblock copolymer was spun-cast on a conductive fluorine-doped tin oxide (FTO) substrate. Only AEM 16 was spun-cast. FTO was cut into 2x2 cm squares. The substrates were cleaned by sonicating in a 1:1 EtOH/DI bath for 15 minutes followed by a DI bath for 15 minutes. FTO was then air-dried in petri-dish. As-received membranes were

re-cast from tetrahydrofuran (THF). A 5% wt. solution was sonicated for 5 minutes and spun-cast on clean FTO at 3000 rpm. The thicknesses of the membrane were measured by AFM to be ~ 40 nm.

SAXS measurements were performed using a GANESHA 300 XL SAXS. Humidity-dependent SAXS measurements were performed at The Basic Energy Sciences Synchrotron Radiation Center (BESSRC) at the Advanced Photon Source at Argonne National Lab on beamline 12 ID-B. A Pliatus 2M SAXS detector was used to collect scattering data with an exposure time of 1 s. The X-ray beam had a wavelength of 1 Å and power of 12 keV. The intensity (I) is a radial integration of the 2D scattering pattern with respect to the scattering vector (q).

The specimens were prepared by Leica CryoUltramicrotome. The microtome chamber was cooled down to -100 ^{o}C by liquid nitrogen, where the bulk sample was microtomed with a diamond knife to a thickness around 40 nm. The cutting sections were then collected on 400 mesh copper support grids and stained by OsO_4 vapor for 20 minutes at room temperature. Characterization was performed on a JEOL 2000FX TEM operated at an accelerating voltage of 200 kV.

Height and phase images were acquired in tapping mode using an atomic force microscope (Asylum Research MFP3D). Standard silicon probes (XSC11, Mikromasch) with resonant frequency (~300 kHz) and spring constant (40 N/m) were used. The power spectral densities (PSDs) were computed in Gwyddion and plotted in Igor Pro. The PSDs were collected over 5 different regions corresponding to a different image. The position of the peak indicates the maximum spatial frequency of the AFM phase images. We identify the first peak (q) in the PSD. The d-spacing is defined as $\frac{2\pi}{q}$.

EFM is an amplitude contrast tapping mode AFM technique based on two-pass interleave scan in which height and phase are measured in the first pass and a lift height of 20 nm is applied to the tip in the second pass. A constant DC bias is applied to the electrode substrate while the tip is held at ground. A platinum-coated tip provided by Micromasch (model HQ:XSC11/Pt) with a resonant frequency of ~325 kHz, and tip radius of curvature < 27 nm was used. The same region was scanned with different voltage biases applied to the substrate from the microscope controller. We applied 0V, +/-1V, +/-3V, and +/- 5V. The measurements were done under ambient conditions (30-50% RH) and at room temperature. All the images were acquired using the retrace image. The (x,y) position of the domains in the phase image were marked by a cursor which highlights the (x,y) position in the EFM images. Domains that appeared to be influenced by roughness in the height image were neglected. A more detailed description of how height-artifacts are neglected are described in a previous report. The EFM phase as a function of V_{EFM} ($V_{EFM} = V_{tip} - V_{substrate}$) was plotted for each domain and was fit to a 3rd order polynomial.

C. Bulk and Surface Morphology of AEM 13 and AEM 16
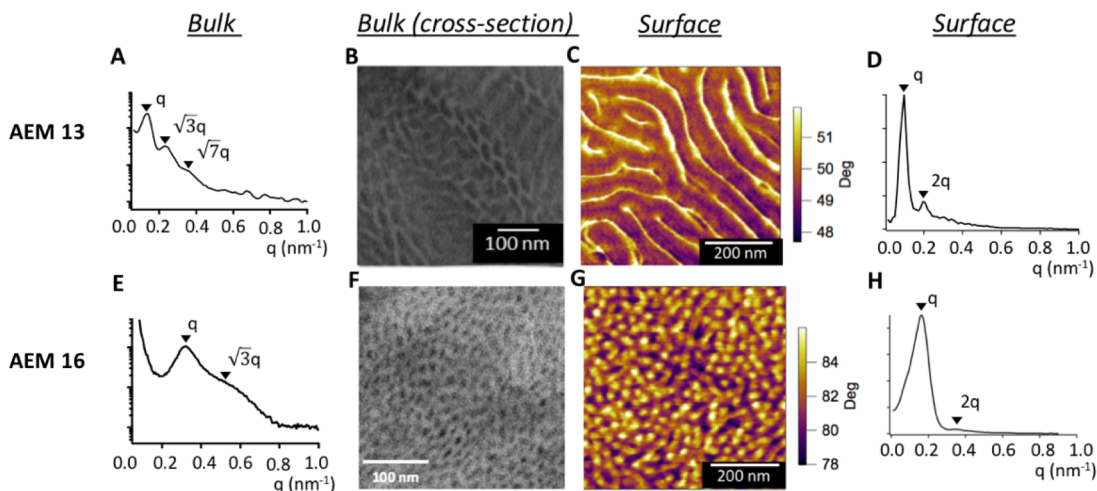
Figure 6.1: Comparison of the bulk (internal) structure and surface structure of AEM 13 and AEM 16. SAXS of (A) AEM 13 and (E) AEM 16, with peak labeled, both indicating hexagonal morphology. Cross-sectional TEM of (B) AEM 13 and (F) AEM 16, where dark contrast corresponds to PIp domains. Repulsive mode phase images of (C) AEM 13 and (G) C, where dark contrast corresponds to PIp domains. Radially-averaged power spectral density (PSD) of phase images of (D) AEM 13 and (H) AEM 16, with higher order peak at 2q labelled.

The following investigation involves specifically with AEM 13 (IEC = 0.44 mmol/g) and AEM 16 (IEC = 0.87 mmol/g). Bulk morphologies were investigated by SAXS and TEM, as shown in Figure 6.1. SAXS profiles of the AEM 13 and 16 are shown in Figure 6.1A and 6.1E, respectively. Figure 6.1A (AEM 13) shows scattering peak positions at q, $\sqrt{3}$q, and $\sqrt{7}$q, while Figure 6.1E (AEM 16) shows peak positions at q and $\sqrt{3}$q. Both peak positions are indicative of hexagonal cylinder morphology. The orientation of the cylindrical domains was assessed by cross-sectional TEM. Figure 4.1B and 4.1F show cross-sectional TEM of the bulk structure of AEM 13 and AEM 16, respectively. Prior to TEM, the membranes were microtomed to ~40 nm thick slices and stained by OsO_4, which selectively stains olefin. Therefore, the dark contrast indicates the hydrophobic PIp domains.

In Figure 4.1B, a mixture of perpendicular and parallel aligned cylinders were observed. The surface morphology was revealed by AFM. The phase images were collected in repulsive mode. We have interpreted the bright contrast as the ionic $P(R_3P^+)MS$ domains and the dark contrast as the hydrophobic PIp domains. By imaging partially quaternized membranes, we have indicated that the bright regions are associated with the ionic domains, as shown in Figure 5.3B. Figure 6.1C and 6.1G are phase images of AEM 13 and spun-cast AEM 16, respectively. The images show stark differences between the surface alignment. Figure 6.1C shows cylinders forming parallel to the surface, while Figure 6.1G indicates perpendicularly aligned cylinders. This implies that in AEM 13, perpendicular channels convert to parallel channels at the surface during membrane fabrication. In AEM 16, on the other hand, shows perpendicular alignment of the channels. By spin-casting AEM 16, it was possible to preserve the bulk morphology at the surface. This provides a means of comparing the conductive properties of two different surface morphologies for AEMs having similar bulk morphologies. Surface alignment was further confirmed by PSD analysis for both AFM phase images, as shown in Figure 4.1D and 4.1H, respectively. The PSD is useful in analyzing spatial frequencies of AFM images. Surface ordering information of block copolymer membrane films through analysis of peak positions of higher order peaks relative to the primary peak.[96] In Figure 6.1C, the peaks are positioned at q and 2q, which signifies regular periodic order typically observed in lamellar phases. In Figure 6.1H, the peak positions for AEM 16 are also at q and 2q with the higher order peak is much less intense, signifying short-range order.

Domain sizes and spacing can be measured from the bulk and surface, respectively. For AEM 13, the average diameter of the PIp domains within the bulk was measured by TEM to

be 40 nm, in agreement with the d-spacing ~42 nm calculated from SAXS. On the surface, the cylinders were 60 nm in width by measuring several line profiles from AFM. The surface d-spacing can also be calculated from the PSD of the phase images, defined as d = $\frac{2\pi}{q}$, where q is the primary peak. From Figure 6.1D, the d-spacing was 61 nm, corresponding approximately to the widths of the cylinders measured by line profiles. In AEM 16, however, similar domain sizes were observed from both the bulk and the surface. From the TEM image in 6.1F, the average diameter was 20 nm. This is comparable with the d-spacing from SAXS shown in Figure 6.1E, which was 23 nm. On the surface, the average diameter of the bright and dark domains in Figure 6.1G was 17 nm and 19.8 nm, respectively. The d-spacing from the PSD shown in Figure 6.1H is 36.7 nm, which indicates close agreement of surface d-spacing with that in bulk.

The surface free energy difference between two blocks in block copolymers influences the alignment of domains at the air-membrane interface.[69,113] A cartoon illustration of the proposed channel structures due to alignment difference is shown in Figure 6.2. Mixed alignment of PIp cylinders in the bulk with parallel alignment on surface for AEM 13 is shown in Figure 6.2A. It is possible that these misalignments between the surface and bulk, or transition zone, can result in discontinuities of the ionic phase and prevent charges from reaching the air-membrane interface. Discontinuities can be readily seen within the 2-dimensional plane of the surface of AEM 13 shown in Figure 1C. Therefore, it is likely these discontinuities would extend within the bulk. Additionally, the expanded diameters of the PIp cylinders of AEM 13 cover most of the surface of the membrane, which can lead to lower connectivity. This case results in continuous ionic regions that allow charges to migrate contiguously throughout the entire membrane. Thus, the conductivity of block

copolymer AEMs is dependent on channel alignment at the surface.[148,149,151] Figure 6.2B

illustrates that at high volume fraction of the $P(R_3P^+)MS$ block, the cylinders only align

perpendicular to the air-membrane interface throughout the membrane, leading solely to

connected paths. Additionally, AEM 16 exposes significantly more of the conductive blue

region on the surface, which can lead to better connectivity through the membrane and

hence better conductivity.
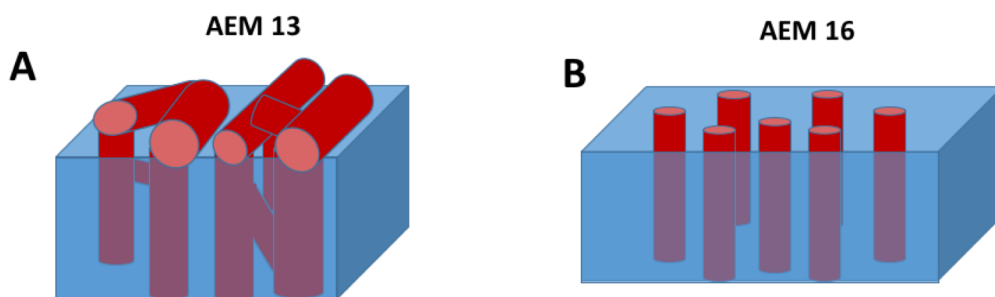
Figure 6.2: Cartoons illustrating the proposed structure leading to variation in channel connectivity. The red cylinders represent the PIp phase while blue represents the continuous ionic phase. (A) Low volume fraction of the ionic block gives rise to parallel aligned cylinders. This orientation can either block surface charge migration, or provide a connected path. (B) At high volume fraction, cylinders are aligned perpendicularly, which gives rise to only connected paths.

Different sample preparation methods play a significant role in affecting bulk and

surface morphologies, via different membrane formation kinetics.[40] AEM 13 was prepared

by drop-casting from $CHCl_3$ solution onto a PTFE sheet. AEM 16 was spun-cast from THF

solution onto a fluorine doped tin oxide (FTO) substrate. Drop-cast membranes were ~6 μm

thick while spun-cast membranes were ~40 nm thick. It has been demonstrated that

membrane deposition by fast solvent extraction via spin-casting or solvent vapor annealing

can trap the block copolymer in a non-equilibrium morphology.[159,160] In drop-cast

membranes, the solvent evaporates slowly (over 6 h) under ambient RH, which favors the

formation of larger ionic domains on the surface than bulk. In spun-cast membranes, the

bulk structure is trapped at the surface because the membrane is not given enough time to reach equilibrium at ambient RH, thus giving rise to smaller ionic domains distributed on surface. Since the alignment, ordering, and size of domains at the surface of spun-cast AEM 16 are commensurate with bulk measurements of drop-cast AEM 16, we use AEM 16 as a benchmark hexagonal membrane with a well-connected ionic phase to compare with AEM 13. Furthermore, the similarities in bulk morphologies of AEM 13 and AEM 16 make them good candidates for comparing the influence of different surface alignments on charge migration and connectivity of the ionic phase.
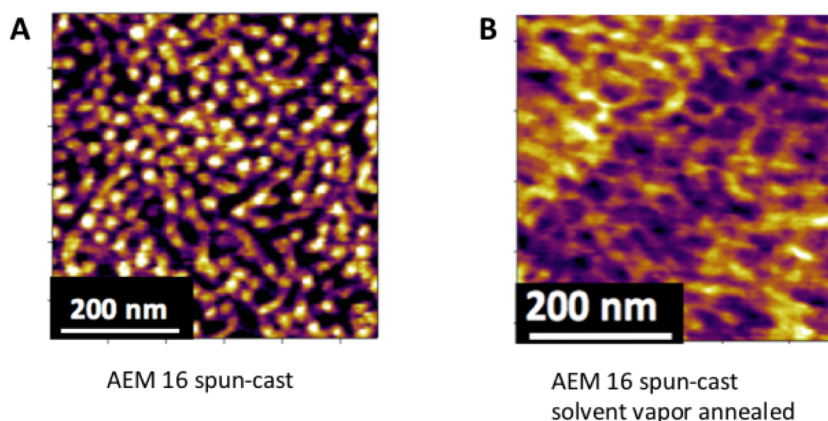
Figure 6.3: Phase images of (A) spun-cast AEM 16 and (B) spun-cast and solvent vapor annealed AEM 16.

In addition to spin-casting, we have also made attempts to solvent vapor anneal our spun-cast membranes. After spin-casting from THF, the membrane was annealed with THF vapor. In the annealing process, the FTO-membrane sample was placed in a Pyrex petri dish. 4 THF droplets were pipetted into the dish surrounding the sample. The dish was then covered and left to anneal over-night. Figure 6.3 shows the difference in morphology

between spin-casting and spin-casting with solvent vapor annealing. Figure 6.3A shows a typical well-order surface morphology with the bright regions mostly isolated at the surface. After annealing, the surface becomes more disordered with the bright regions becoming more connected, which is shown in Figure 6.3B. In our experiments, we decided to choose spin-casting over solvent vapor annealing because of the extent of the ordering at the surface. However, future experiments should investigate the effect of solvent vapor annealing on the connectivity of the ionic domains by EFM or cp-AFM.
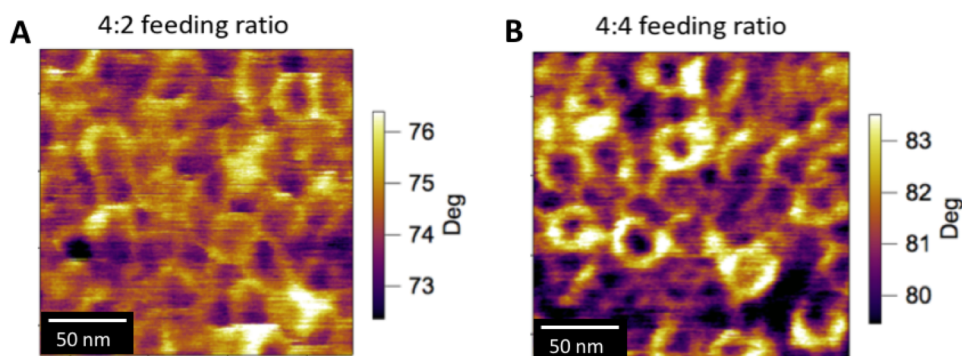
Figure 6.4: Phase images of spun-cast AEM 16 at different QL or feeding ratios: (A) _0.5_P_ and (B) _1_P_.

Control experiments were conducted on partially quaternized spun-cast membranes to further understand if the regions of bright contrast were the ionic component in the repulsive-mode phase images. In Chapter 5, we observed an increase in the frequency of bright regions with increasing QL of thick as-received membranes. We compared two partially quaternized spun-cast membranes of 4:2 feeding ratio (_0.5_P_) and a 4:4 feeding ratio (_1_P_) of AEM 16 shown in Figure 6.4. Although the AEMs were quaternized by a smaller agent, triphenyl phospine (P(Ph)$_3$) we showed previously the morphology was

similar to our traditional quaternization agent.[161] The QL was achieved by using reaction stoichiometries, or 'feeding ratios' of PIp-PCMS to $P(Ph)_3$. The two images shown in Figure 6.4 show a similar morphology; however, we see higher contrast between domains for higher QL. Therefore, we continue to assign the bright regions as the ionic domains.

D. Membrane Thickness Measurement of AEM 13 and AEM 16
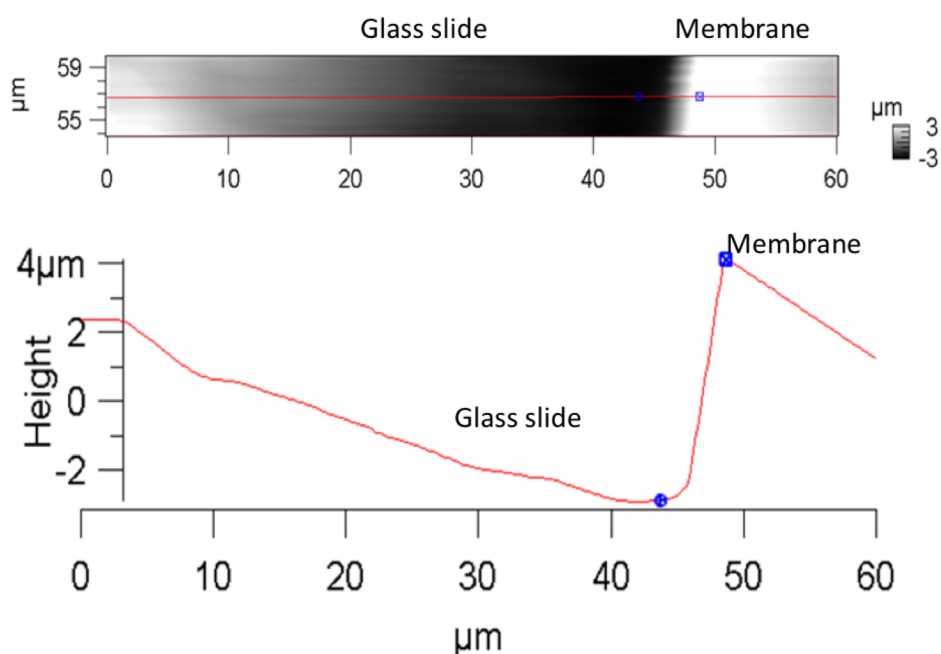
Figure 6.5: (Top) Partial scan of an AFM height image (4 µm x 60 µm) and (bottom) a line profile from the height image. The blue markers indicate where a height measurement was made.

The thickness of AEM 13 was measured by imaging the edge of the membrane. The membrane was mounted by epoxy onto a glass slide. Figure 6.5 shows a partial scan of a height image with a corresponding line profile. The blue markers indicate where the difference in height was measured. For this data, we found the membrane to be 6 µm thick.

117
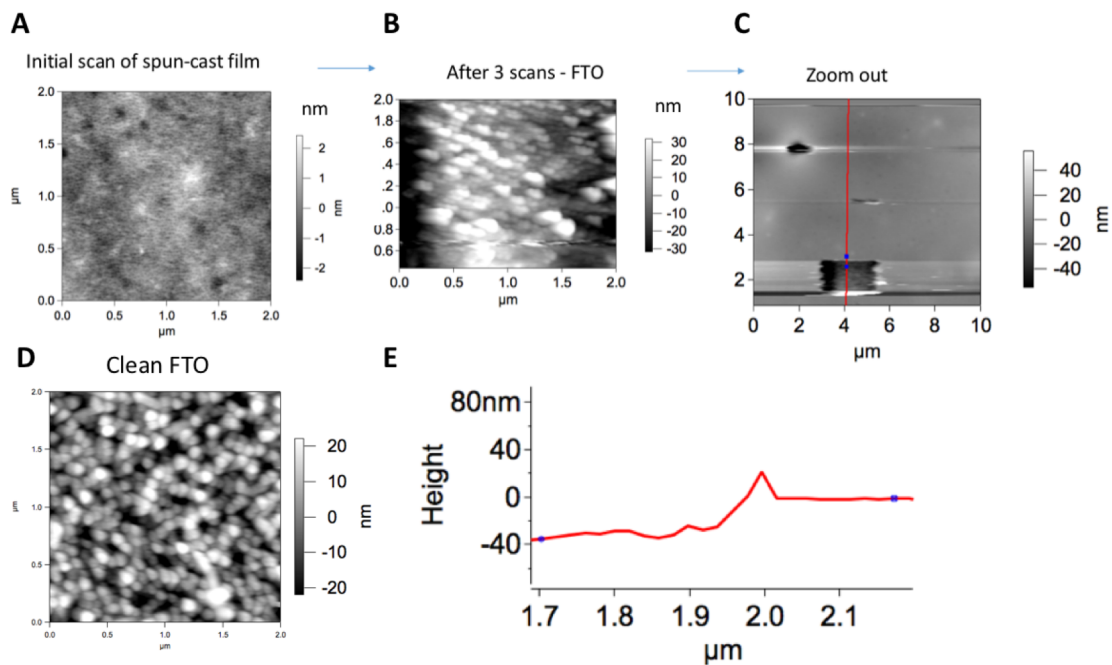
Figure 6.6: Tip-scratching method for determining thickness of AEM 16. (A) Initial scan of the spun-cast membrane. (B) After 3 scans, the surface resembled FTO. (C) Zoom out image of membrane showing a depression where the previous scan occurred. (D) Clean FTO scan for comparison. (E) Line profile from (C) to measure membrane thickness.

The tip-scratching method was carried out in contact-mode. In contact-mode, the tip is in constant contact with the surface. Due to the softness of the membrane and large contact force (20 nN), this method was useful in determining the membrane thickness of our spun-cast samples. After 3 scans of a 2x2 µm region, the FTO morphology was revealed as shown in 6.6B. A clean FTO scan was taken in tapping mode as a point of comparison shown in Figure 6.6D. Zooming out to a 10x10 µm region, we found a square depression from the original scan location. The membrane thickness was measured by taking a line profile across the depression and was ~40 nm. The blue cursors on the red line profile show where the measurements were made.

E. EFM Results

EFM is a tapping-mode AFM based technique that probes the electrostatic force gradient. EFM is based on two-pass interleave scan. In the first pass, the height and phase are gathered. In the second pass, phase deviations are influenced by the electrostatic force gradient, which is attributed to surface charge, dielectric permittivity, and film capacitance. The conductive tip is raised above the surface by 20 nm. A constant DC bias is applied to the electrode FTO sample substrate (V_{sample}) while the platinum-coated tip is held at ground ($V_{tip} = 0$). Conventionally, the bias voltage is defined as $V_{EFM} = V_{tip} - V_{sample}$. Hence, $V_{EFM} = -V_{sample}$. The ions migrate depending on the sign of the bias voltage, for example, a $V_{EFM} = +5V$ implies a negative sample voltage and would bias the ions toward the surface. Figure 6.7A and 6.7D shows first pass phase images of AEM 13 and AEM 16 showing the same morphologies from images shown in Figure 1. Figure 6.7B and 6.7C shows EFM images of AEM 13 at -5V and +5V FTO sample bias, respectively.
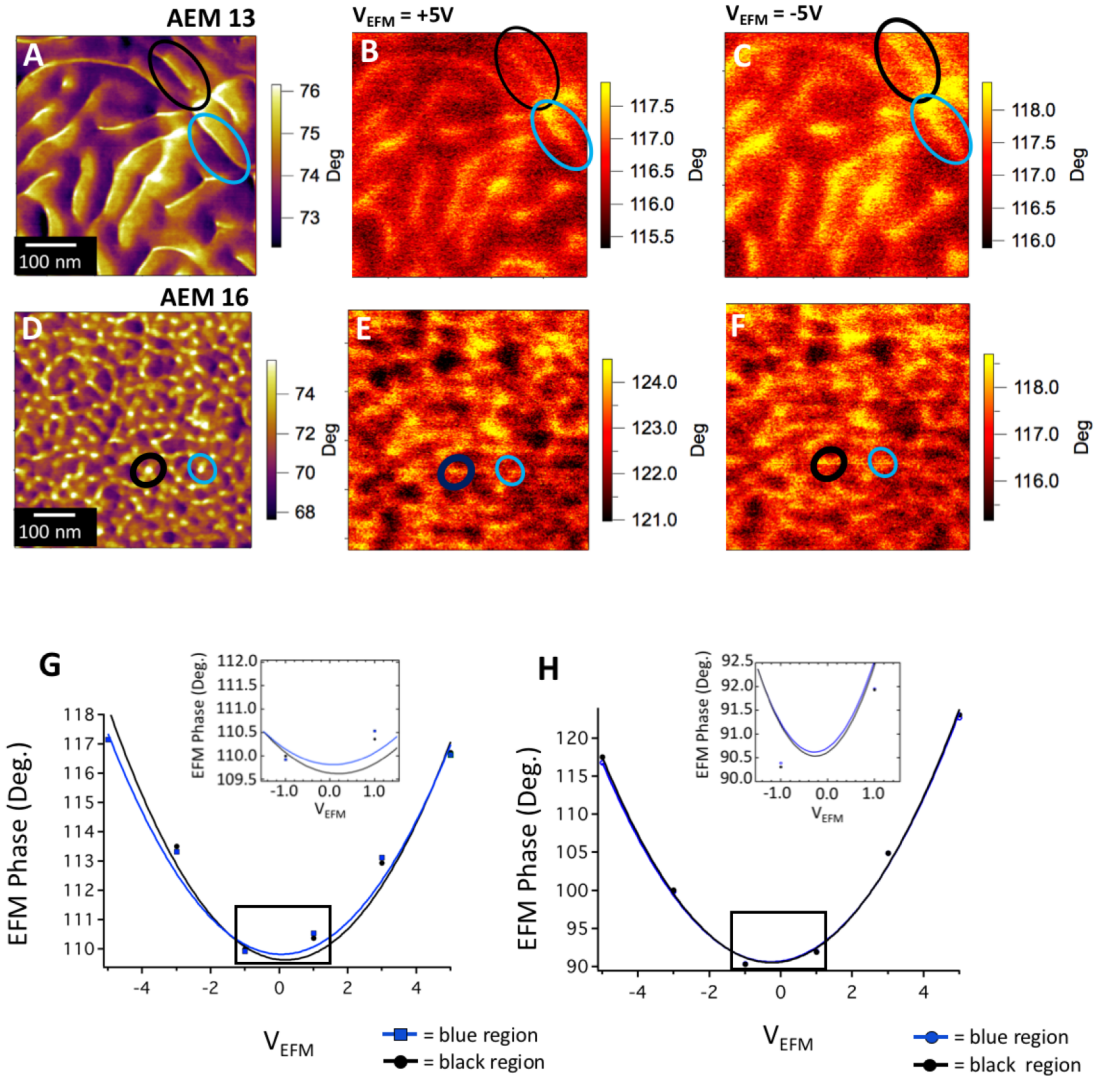
Figure 6.7: (A) First pass repulsive-mode phase image of as-received AEM 13. EFM images taken in the second pass at (B) V_{EFM} = +5V and (C) V_{EFM} = -5V sample bias. (D) Repulsive-mode phase image of AEM 16 taken in the first pass. EFM images taken in the second pass at (E) -5V sample bias and (F) +5V sample bias. Parabolic response of EFM phase as a function of V_{EFM} (V_{EFM} = V_{tip}-V_{sample}) for two regions highlighted (G) in 6.7A-C of AEM 13 and (H) in 6.7D-F of AEM 16.

Two representative ionic regions of AEM 13 are highlighted in Figure 6.7A-C. The EFM phase was determined by drawing a square box (20 nm × 20 nm) over the ionic region of interest in the first pass phase image in Igor Pro. The (X,Y) spatial coordinates in the first pass correspond to the same coordinates in the second pass EFM phase image, and therefore the square box can be copied onto the second pass EFM image. The statistical average was measured over ~100 pixels contained in the square box. This method was applied to the same ionic region of interest for each voltage bias. For example, the blue highlighted region shows a small uniform shift (-0.5°) in EFM phase between the +5V and -5V image while the black region shows a larger and more negative shift (-1.5°) between the two images. A different EFM phase response as a function of voltage bias was observed for AEM 16. Figure 6.7D shows a repulsive mode phase image of AEM 16. Similar EFM phase contrast can be seen in blue and black highlighted regions at both voltage biases (Figure 6.7E and 6.7F), showing a uniform shift in the EFM phase (+5.9°) with respect to voltage bias for both regions. Besides, a higher EFM phase shift was observed as expected, since AEM 16 has larger IEC, allowing larger population of charges to be biased towards the surface, which leads to a larger positive shift. Heterogeneity in the EFM phase of AEM 13 can be attributed to "dead-end" pathways within the ionic phase due to the parallel hydrophobic cylinders that block the chloride from reaching the surface, while homogeneity for AEM 16 can be attributed to identical channel morphology throughout the membrane.

It is important to note that the sign of the shift does not provide adequate information on the channel structure, thus the parabolic EFM behavior of the ionic domains must be analyzed. EFM phase shifts as a function of the bias voltage and can be described mathematically via Eq. 6.1.[159]

$$\Delta\Phi = -\frac{Q}{2k}\frac{d^2C}{dz^2}[(V_{EFM} - V_s)^2 - 2(V_{EFM} - V_s)V_q + V_q{}^2] \qquad (6.1)$$

where Q is the quality factor of the cantilever, k is the spring constant of the cantilever, C is

the capacitance of the tip-sample system, z is the height above the surface. V_{EFM} is the bias

voltage ($V_{EFM} = V_{tip} - V_{sample}$). V_s is the surface potential, which is related to the work

function difference between the tip and the sample and is independent of the lift height. We

consider V_s to be a constant offset potential and is independent of V_{EFM}. V_q is the potential

related to the charge enclosed and is dependent on the lift height. The first term in Eq. (6.1)

is related to the tip-sample capacitance and induced polarization of the film, which is always

an attractive force. The middle term in Eq. (6.1) is related to the interaction between the

stored charge, q and the EFM tip apex. The third term is related to the image charge effects,

since this is independent of V_{EFM}, we have ignored this interaction from analysis. We can

simplify the expression for Eq. (6.1) into two terms: a charge force gradient ($\Delta\Phi_q$) that has

a linear dependence on V_{EFM} and a capacitive force gradient ($\Delta\Phi_C$) that has a quadratic

dependence with V_{EFM}.

$$\Delta\Phi = \Delta\Phi_q + \Delta\Phi_C = AV_{EFM} + BV_{EFM}{}^2 \qquad (6.2)$$

A and B are fitting parameters to the linear and quadratic terms, respectively. For a charged

dielectric film placed in a uniform electric field, the quadratic and linear terms are derived

analytically.

$$B = \frac{Q}{2k}\left(\frac{3\alpha}{(z+d)^4}\right) \qquad (6.3)$$

$$A = \frac{-Q\,q}{2\,k\,\,(z+d)^3} \qquad (6.4)$$

where α is the electric polarizability, d is the film thickness, and q is the stored charge.

For the blue region highlighted in AEM 13, the average EFM phase was measured for each voltage bias and plotted as blue squares shown in 6.7G. The method of measuring the EFM phase was the same method previously described.[94] The data was fit to a quadratic function and the fit curve is shown as the blue line. Similarly, the black region in AEM 13 was plotted as black circles and fit to a quadratic function shown as the black line. In 6.7G, there are noticeable differences between the blue and black fits. The insets show a close-up of the differences. Furthermore, the analytical expressions shown in Eq. (6.3) and (6.4) can be simplified by taking the ratio of A and B, which is dependent on stored charge (q), membrane thickness (d), and polarizability (α).

$$\frac{A}{B} = \frac{-q(z+d)}{3\alpha} \qquad (6.5)$$

Note Eq. (6.5) is similar for the ratio expression derived for EFM studies of Nafion[®].[121] The EFM phase of Nafion[®] was background subtracted and assumptions regarding the relative permittivity and the charge density of the ionic domains allowed for simplified expressions. Heterogeneity in the A and B fits were due to differences in channel length or geometry. These AEM materials represent an inverse of the morphology of Nafion[®]. As

opposed to a proton conducting cylindrical channel surrounded by a Teflon-like matrix, we are investigating membranes in which the conductive ionic phase is the surrounding medium and PIp cylinders are embedded. In this investigation, we can draw similar conclusions, however, we are comparing two membranes of different charge density (IEC) and membrane thickness. Therefore, the EFM phase was not background subtracted and the membrane thickness (d) is included in the expression, which represents a pocket of charge or a connected channel plus the remaining thickness of the membrane. The relative permittivity of the ionic domains is also not known. Hence, B was expressed in terms of the polarizability of the membrane.

For the blue curve, the fitting parameters were $A = -0.036°/V$ and $B = 0.294°/V^2$. Thus, A/B is calculated to be -0.122 V. For the black curve in 6.7G, $A = -0.118°/V$, $B = 0.321°/V^2$, and A/B = -0.368 V. The differences in A/B between these two regions supports our qualitative depictions shown in 6.2A. The black region in AEM 13 shows a large negative A/B which signifies a "dead-end" pathway for charges, while the blue region shifts to less negative, signifying a well-connected pathway. Both A/B values are negative, which could be due to a negative surface potential, V_s, the potential in the absence of stored charge shown in Eq. (6.1). The same analysis was performed on AEM 16. First, smaller deviation was observed in 6.5H between quadratic fits for blue and black regions highlighted in images 6.7D-F. For region 1, $A = 0.632°/V$ and $B = 1.201°/V^2$. For region 2, $A = 0.661°/V$ and $B = 1.176°/V^2$. A/B for these regions are 0.525 V and 0.562 V, respectively.
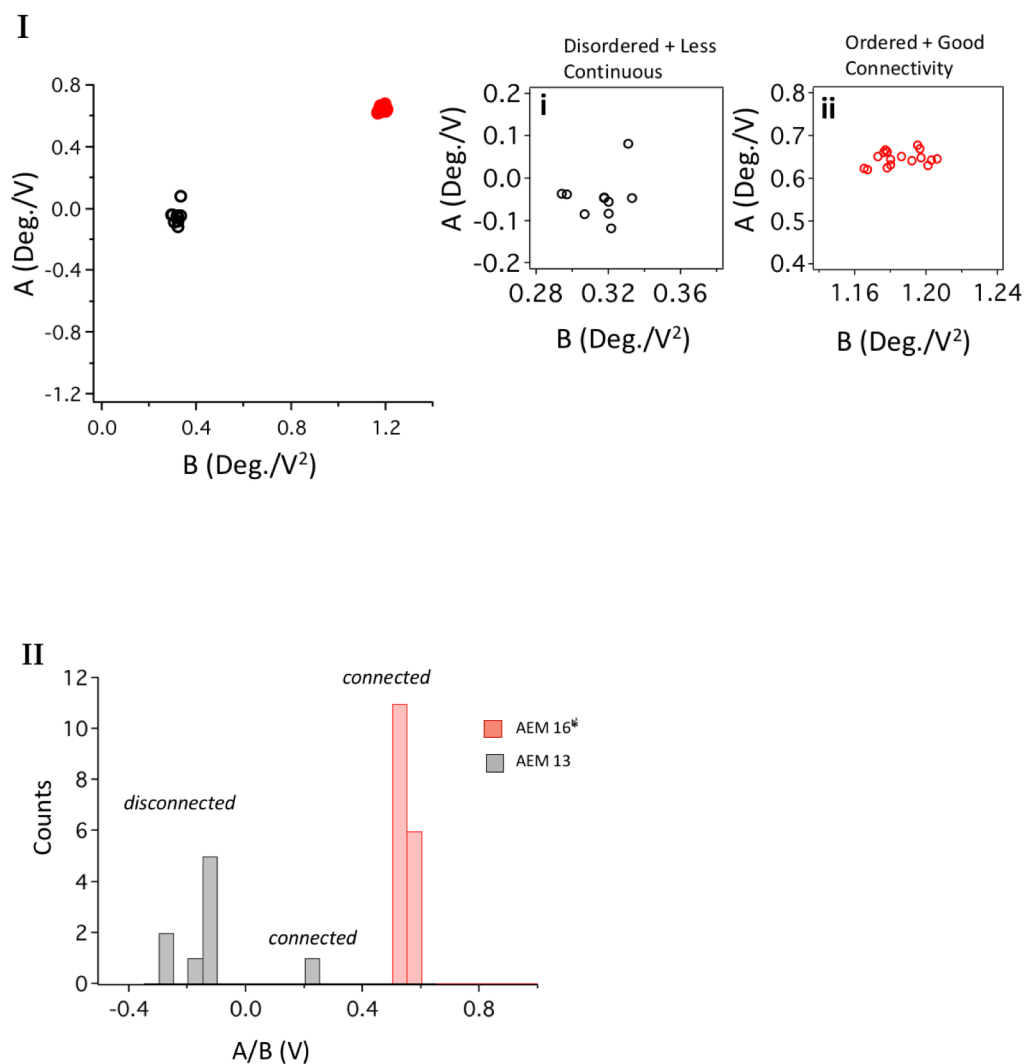
Figure 6.8: (I) Scatter plot of the linear fit term A vs. quadratic fit term B for several features of AEM 13 in black circles and AEM 16 in red circles. Inset shows a close-up of the scatter plot (I-i) AEM 13 and (I-ii) AEM 16. (II) Histogram of A/B data from (6.8-I) for AEM 13 (gray) and AEM 16 (red).

We continued our investigation of the distribution and parabolic EFM behavior of several ionic domains on AEM 13 and 16. It is important to note that not all ionic domains were able to be analyzed due to topographic artifacts. These topographical artifacts can contribute to the EFM phase and were thus avoided. A detailed discussion about how we

discriminated these channels has been described previously.[121] In the EFM images that correspond to Figure 6.7A-C, 10 regions of interest were analyzed, while 17 regions of interest were analyzed for 6.7D-F. Figure 6.6I shows scatter plots of fit parameter A vs. B for all ionic regions analyzed for AEM 13 and AEM 16, respectively. The inset scatter plots show a close-up of the data highlighting the difference in variance of AEM 13 (6.6I-i) and AEM 16 (6.8I-ii). For AEM 13, points distribute near $A = 0°/V$ and $B = 0.31°/V^2$, while for AEM 16 the fit parameters can be seen near $A = 0.65°/V$ and $B = 1.18°/V^2$. The increase in both fit parameters A and B from AEM 13 to AEM 16 is due to increased IEC. A larger IEC would increase the total amount of stored charge of the membrane and thus increase A, according to Eq. (6.4). An increase in the IEC would also make the membrane more polarizable, which would lead to an increase in B according to Eq. (6.3).

Figure 6.8II shows a histogram of A/B for AEM 13 and AEM 16 regions. AEM 13 shows a broad distribution with a cluster of points below A/B = 0, while AEM 16 shows a narrow distribution of A/B > 0. The variance in the distribution of A/B is attributed to the variation in ionic connectivity. We have recently made a similar analysis to investigate the channel connectivity of Nafion®.[121] Since the shape of the hydrophilic channels can be approximated as cylinders,[121] we could use the isolated cylinder model to interpret our EFM data. In the isolated cylinder model, A is proportional to the channel length.[14] Assuming that charge density is uniform, the variation in A/B is due to variations in channel length. Furthermore, the same model can be applied depending on whether cylinders lay parallel[96] or perpendicular.[89] Thus, we were able to conclude that only 1 out of 10 regions of AEM 13 led to a connected path, while the rest were dead-end paths, and for AEM 16, all regions analyzed led to connected paths, as expected for perpendicular aligned channels.

F. Control EFM Measurements of an Un-quaternized AEM

It is important to note that Eqns. 6.3-5 also indicate a dependency on the membrane thickness. Control experiments in which the A and B values were measured of thick drop-cast and thin spun-cast membrane of un-quaternized AEM 19 (AEM 19*) are shown Figure 6.9. The un-quaternized membranes merely consist of PIp-PCMS. The membrane has an IEC of 0 mmol/g and contain no mobile charge.
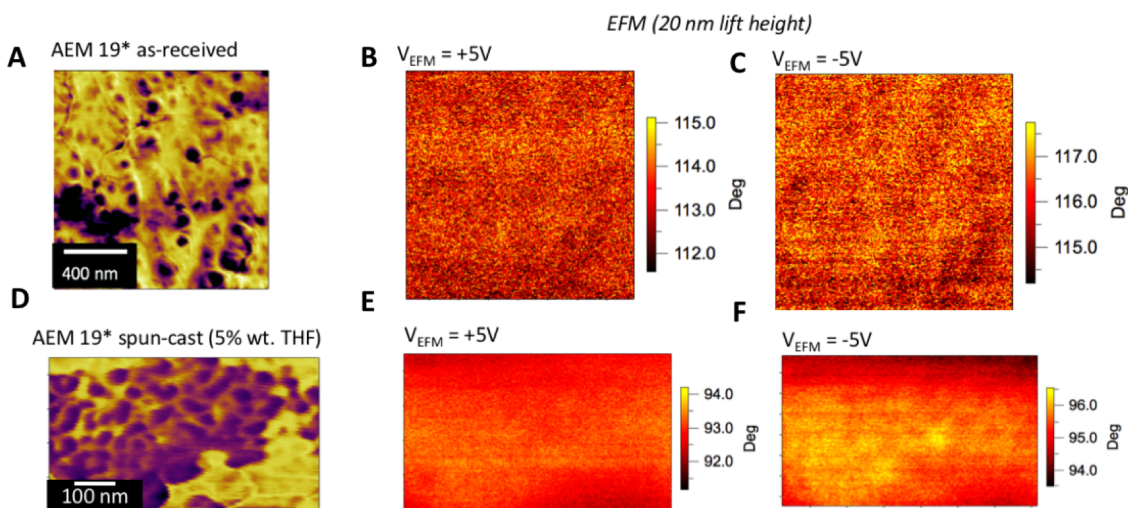
Figure 6.9: (A,D) First pass attractive mode phase and (B,C,E,F) second pass EFM images of (A-C) un-quaternized AEM 19 as-received and (D-F) spun-cast.

From Table 5.1, AEM 19 has a molecular weight of 29 kg/mol. The volume fraction of the PCMS block is 92%. It was found that the morphology gives rise to loosely ordered BCC packing of PIp spheres. A similar surface morphology can be seen in images 6.9A and 6.9B. While the majority of our phase images have been collected in repulsive mode in which regions of bright contrast correspond to the ionic domains, these images were taken in attractive-mode. From equation 1.1, this implies that the contrast flips and dark contrast

corresponds to the ionic domains. It is also important to note that AEM 19* as-received membrane was prepared in the same manner as AEM 13 as received and AEM 19* spun-cast was prepared in the same manner as AEM 16.

The same lift height (20 nm) was applied in the control EFM measurements. For both AEM 19 as-received and AEM 19 spun-cast, very little change in EFM phase contrast was observed at +5V and -5V. The same image area was collected in 1V intervals from -5V to +5V. The average EFM phase for each image was measured, plotted as a function of V_{EFM}, and fit to a quadratic to determine the A and B fitting parameters.
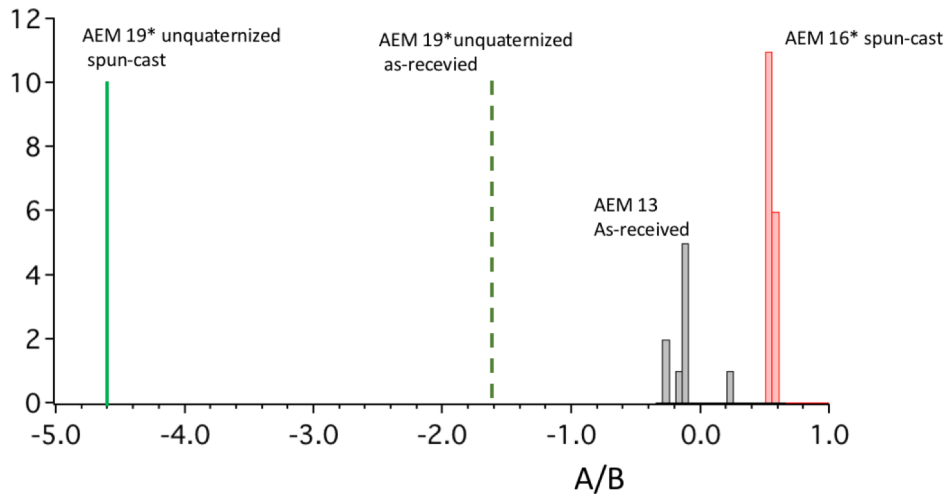
Figure 6.10: Distribution of A/B from Figure 4.6II with the average A/B of AEM 19* as-received and spun-cast represented as a single line.

From the dataset in Figure 6.9, the A/B value for the as-received and spun-cast membrane were plotted next to the A/B distribution data from Figure 6.6II. AEM 19* has the lowest A/B of -4.8 V, while AEM 19* as-received shifts towards higher A/B in accordance with Eqn. 6.5. Since the increase in A/B from AEM 13 (thick membrane) and

AEM 16 (thin membrane) is due to the increase in IEC, the IEC plays a more significant role in the measurement of A/B than membrane thickness.

G. Conclusions

Two AEMs with different IEC were investigated. AEM 13 with low IEC showed a mixture of parallel and perpendicular alignment of PIp cylinders in the bulk though only parallel alignment on the surface. By contrast, for AEM 16 with higher IEC, perpendicularly aligned PIp cylinders were observed throughout the bulk and surface. From EFM phase images of both membranes, the EFM phase shift as a function of voltage bias was measured over the ionic domains. From the investigation on the parabolic EFM behavior as a function of voltage bias for the two membranes, variation was observed in the parabolic response of AEM 13 while very little variation was shown in AEM 16. These results suggest that there are a significant number of disconnected paths for charge to migrate to the surface as a result of the parallel alignment observed in AEM 13, while for AEM 16, highly ordered structure of perpendicular channel alignment leads to a dominant population of connected paths.

VII. Conclusions and Future Directions

The performance of proton exchange membrane (PEM) fuel cells relies on the membrane's ability to conduct protons contiguously from one end of the membrane to the other. Channels that are not connected do not participate in the overall performance of the fuel cell. Cp-AFM has greatly contributed to our understanding of the channel connectivity of Nafion, ~50% of the channels are electrochemically active and are thus connected. However, cp-AFM does not provide information on the channels with zero current. It has been suggested that this could either be due to disconnected channels, inactive catalyst, or a combination of the two. We were interested in investigating this further and implemented EFM to discern the connected channels from the short "dead-end" channels of Nafion.

EFM is an interleaved two pass scanning method. This was advantageous for us since the hydrophilic domains could be mapped in the first pass while surface charge and channel capacitance could be analyzed in the second pass. We imaged the same scan area multiple times at different sample voltages. We analyzed the parabolic EFM response as a function of voltage bias for several channels. The data was plotted, fit to a quadratic, and the linear (A) and quadratic (B) fitting terms were collected. After background subtraction we found 3 classes of channels: A>>B (linear), A<<B (quadratic), and A=B $\approx$ 0 (null). While these measurements are relatively straightforward to carry out, interpretations of the results can be complex. We applied a simple parallel plate capacitor model for a cylindrical channel embedded in a dielectric matrix, which allowed us to assign the differences in EFM phase vs. bias voltage dependences with differences in channel length and structure.

Anion exchange membrane (AEM) fuel cells have attracted significant research interest due to the potential implementation of non-Earth metal catalysts, which would bring down cost of production. Recent advancement in design rationale has guided improved chemical stability of AEMS; however, there has been little to no information regarding how these chemical modifications impact the morphology. Additionally, the early stage development of AEMs necessitates a clear understanding of the ties between morphology and conductivity.

We first used tapping mode phase and cp-AFM to observe the surface morphology and hydroxide conductivity of a commercially available AEM by FumaTech. We compared the morphology of the membrane in both its Br^- and OH^- form. Under dehydrated conditions (18%RH) we found no phase contrast indicating low phase separation and low water retention. Under hydrated conditions (80%RH) in the Br^- form, the phase images revealed randomly dispersed isolated hydrophilic domains while in the OH^- form elongated "worm-like" domains dominated the surface. We attributed these differences in morphology to the differences in water content of the Br^- and OH^- forms. Cp-AFM of the hydrated FumaTech AEM in the hydroxide form revealed these "worm-like" features were insulating, which indicates these features consist of an ionic interior with a hydrophobic shell.

We then turned our investigation toward block copolymer electrolyte AEMs because they form well-ordered continuous channel morphologies. In collaboration with Prof. Coughlin's group we studied phosphonium-containing diblock copolymer AEMs consisting a hydrophobic polyisoprene (PIp) block and a quaternizable polychloromethylstyrene block. The ionic moiety consists of a phosphonium ion quaternized by 3 large methoxy groups, which provide steric hindrance and prevent nucleophilic attack.

We investigated the morphology of AEMs ranging in ion exchange capacity (IEC). We compared our tapping mode phase images with cross-sectional TEM and SAXS. At low IEC, we observed a hexagonally packed PIp cylinders with a continuous ionic phase. While cylinders were mostly aligned perpendicular to the plane of the membrane through the bulk, we found the cylinders to lay parallel on the surface. We suggested that this effect is driven by the lower surface free energy of the PIp block. At moderate IEC, perpendicular aligned cylinders were observed through the bulk and surface. At high IEC, we observed loosely ordered BCC packing of PIp spheres with a continuous ionic phase. We found the PIp domains were larger on the surface than in the bulk, which is due to the low surface free energy of PIp and the long exposure to humidified air during the membrane formation. We also observed the change in domain size and spacing during dehydrated and hydrated conditions, which depends on the IEC. Furthermore, the change in domain size and spacing was reversible between humidity cycles, which was supported by both SAXS and AFM.

We investigated the effect of surface alignment on the channel connectivity of two phosphonium block copolymer AEMs. These AEMs were also good candidates for our EFM methodology; no assumptions were needed regarding the channel shape or structure through the bulk. We compared EFM images of AEM 13 and AEM 16. Applying the same model from our Nafion investigation, we found a significant number of disconnected channels in AEM 13 while AEM 16 was entirely connected.

Improving the chemical stability of AEMs still remains a major research challenge. The FumaTech AEMs, for example, are temperature sensitive; a significant drop in fuel cell performance occurs when the cell temperature surpasses 60 ºC.[96,157] Both chemical and mechanical degradation is accelerated at high temperatures. Mechanical degradation

experiments typically involve heating the membrane in a high pH solution and observing if the membrane is still in one piece.[103] Whereas chemical degradation experiments, which results in the decrease of the IEC, involves titrations. Our closed imaging cell has the capabilities to increase the temperature as high as 140 ºC. One could monitor microscopic changes in the morphology of FumaTech in the hydroxide form as temperature is increased beyond 60 ºC. These AFM experiments could also offer insight toward the kinetics and morphological reversibility between low and high temperatures. Loss in membrane conductivity could also be monitored through cp-AFM; however, one must carefully monitor RH vs. temperature. The RH decreases when the cell temperature increases, which could result in a complete loss of current signal.[162]

Another facet that remains to be explored is how the membrane's surface morphology would change during CO_2 contamination. It is well established that all of the hydroxide ions in an AEM forms carbonate within 1 hour of exposure to CO_2. Recently, Divekar *et al.* conducted SAXS as a function of CO_2 exposure time and saw a shift towards larger d-spacing over 2 hours.[28] Phase images tracking the change in domain size during CO_2 exposure may indicate a difference in the kinetics. Equilibrium would be established faster since CO_2 contaminates the surface prior to the bulk.

A key result from the FumaTech investigation from Chapter 4 was the excessive surface swelling of FAA-3-OH⁻ under 80% RH, which we attribute to the intrinsically high water uptake of the hydrocarbon-based polymer. Swelling can be mitigated with the implementation of fluorocarbon-based AEMs. Park *et al.* has recently synthesized a sulfonylamide-linked quaternary ammonium perfluorinated AEM (PFAEM).[116] Due to the chemical similarities of the PFAEM and Nafion, an understanding of the similarities in the

133

humidity-dependent surface morphology still need to be made. Water uptake ($\lambda = 3$ at 50% RH) and bulk morphology (d-spacing = 4 nm) has already been shown to be similar as Nafion.[163] Any differences in surface morphology is likely due to the longer side-chain of the PFAEM. Differences in morphology as a result of side-chain length has already been shown between Nafion and Hyflon (short side-chain).[116]

A promising research direction is toward vanadium redox flow batteries (VRFBs). PEMs, like Nafion, are commonly employed as the separator between the anolyte (V^{2+}/V^{3+}) and the catholyte (V^{4+}/V^{5+}). Proton conduction balances the charge between the vanadium redox couples. However, Nafion exhibits high vanadium crossover.[74] This has sparked interest in AEM development due to the positively charged quaternary ammonium, which repels vanadium ions and sulfate becomes the carrier. The morphological insight gained from both PEMs and AEMs throughout the above AFM experiments can help guide the design rationale for VRFB membranes. However, these measurements are *ex-situ*. To our knowledge, there has been little to no experiments that study the morphology of VRFB membranes *in-operando*. Tapping-mode imaging under liquid is possible with a modified closed cell that contains fluid ports for the anolyte and catholyte. Any changes in topography of the membrane and its morphological reversibility between charged and discharged states would provide meaningful information regarding vanadium crossover.

Both AEMFCs and VRFBs are promising alternative energy sources that are on the cusp of becoming economically viable. It is hoped that the experimental results presented in this thesis will be built upon and aid the development of AEMs in the future.

Appendix 1: Finite Element Method Calculations in Mathematica

```
Needs["NDSolve`FEM`"];

d = 100;

w1 = .4;

w2 = .6;

sw1 = w1 + .001;

sw2 = w2 - .001;

sy1 = 1 / d + .001;
```

1/3 - 1/d is the channel length. d=100 is a connected channel. w1 and w2 define the width of the channel

▪ Finite Element Method - Create a boundary mesh

```
bmesh1 = ToBoundaryMesh[
    "Coordinates" → {{0, 0}, {1 / 100, 0}, {1 / 100, 1 / 100}, {99 / 100, 1 / 100},
      {99 / 100, 0}, {1, 0}, {1, 1 / d}, {1, 1 / 3}, {1, 1}, {0, 1}, {0, 1 / 3}, {0, 1 / d},
      {w1, 1 / d}, {w2, 1 / d}, {w1, 1 / 3}, {w2, 1 / 3}}, "BoundaryElements" →
    {LineElement[{{1, 2}, {2, 3}, {3, 4}, {4, 5}, {5, 6}, {6, 7}, {7, 8}, {8, 9},
      {9, 10}, {10, 11}, {11, 12}, {12, 1}, {11, 8}, {12, 7}, {13, 15}, {14, 16}}]}];
```

```
mesh1 = ToElementMesh[bmesh1, "BoundaryMeshGenerator" → {"Continuation"},
    MaxCellMeasure → 0.002, "MaxBoundaryCellMeasure" → 0.01, "MeshOrder" → 1]
mesh1["Wireframe"]

ElementMesh[{{0., 1.}, {0., 1.}}, {TriangleElement[<800>]}]
```
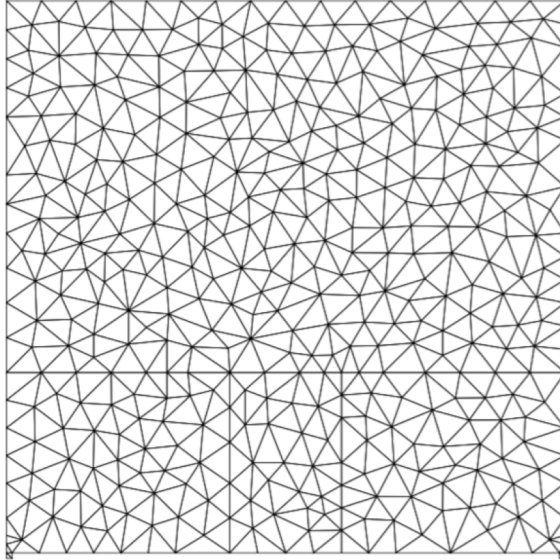


```
er = Which[1 / 100 < y < 1 / d, {{2, 0}, {0, 2}},
    1 / d ≤ y ≤ 1 / 3 && w1 ≤ x ≤ w2, {{70, 0}, {0, 70}}, 1 / 3 < y ≤ 1,
    {{1, 0}, {0, 1}}, x < w1, {{2, 0}, {0, 2}}, x > w2, {{2, 0}, {0, 2}}];
```

This is the relative permittivity. I define the relative permittivity of the channel as bulk water (80), the matrix as 2, and air (1).

```
ρc = If[1 / d ≤ y ≤ 1 / 3 && w1 ≤ x ≤ w2 , 10^-8, 0];
```

The charge density needs to be defined as a conditional expression. Charge only exists within the channel, all other regions have zero charge.

■ Solve the Poisson equation over the element mesh

```
ε0 = 8.86*^-12;
```

```
op = Inactive[Div][-er.Inactive[Grad][u[x, y], {x, y}], {x, y}] - ρc / ε0;
```

```
Subscript[Γ, D] = {DirichletCondition[u[x, y] == 0, x == 0 || x == 1 || y == 1],
    DirichletCondition[u[x, y] == 0, y == 1 / 100]};

kpfmconditions = {DirichletCondition[u[x, y] == 0, x == 0 || x == 1],
    DirichletCondition[u[x, y] == 00, y == 1 / 100]};
```

These are the boundary conditions I've defined. I don't think these define the complete Cauchy conditions for this system, but correctly defines the boundary potential for the sample substrate and the tip.

```
ufun = NDSolveValue[{op == 0, Subscript[Γ, D]}, u, {x, y} ∈ mesh1]
```

InterpolatingFunction[⊞ 〰 Domain: {{0., 1.}, {0., 1.}}
                              Output: scalar]

```
Show[ContourPlot[ufun[x, y], {x, y} ∈ mesh1,
    ColorFunction → "Temperature", PlotLegends → Automatic], bmesh1["Wireframe"]]
```
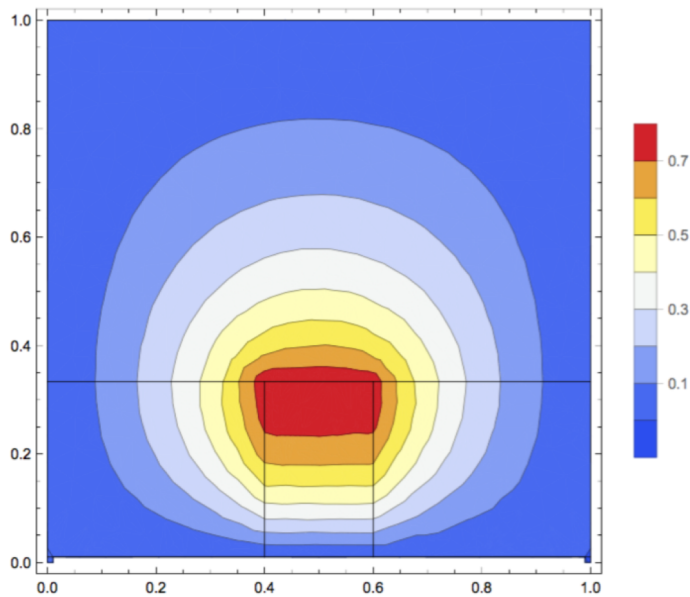


```
g[x_, y_] = -Grad[ufun[x, y], {x, y}];
```

g[x,y] is the electric field

```
F = - (ε0 / 2) * Sum[Dot[g[i, 1]^2, {0, 1}], {i, 0, 1, .01}]
```

-5.96266×10^{-11}

F is the force acting on the "tip", which I've defined as a horizontal line, y=1. The electric field squared is taken as the projection normal to y=1.

Appendix 2: Mapping the Surface Potential of Nafion by Kelvin Probe Force Microscopy (KPFM)

A. Introduction

Kelvin Probe Force Microscopy (KPFM) is non-contact tapping mode technique that measures the surface potential (V_s) between a Pt-coated tip and sample. Since V_s depends on the surface charge, we can infer how V_s depends on the channel size and shape similar to the EFM investigation of Nafion in Chapter 3. While the EFM signal is influenced by both the surface potential and dielectric permittivity of Nafion, the KPFM signal is only dependent on the surface potential. This provides a means of simplifying our interpretations of the EFM data and offering additional insight toward the surface charge characteristics. However, we did not find this to be the case when analyzing the individual hydrophilic domains. Therefore, our KPFM data was not featured in our initial EFM report.[121] Nevertheless, KPFM has offered interesting insight in the long-range heterogeneity of the surface charge of Nafion.

As in EFM, KPFM is a two pass interleaved scan. The topography and phase is collected in the first pass. During the second pass, the probe is lifted off the surface and V_s is collected.
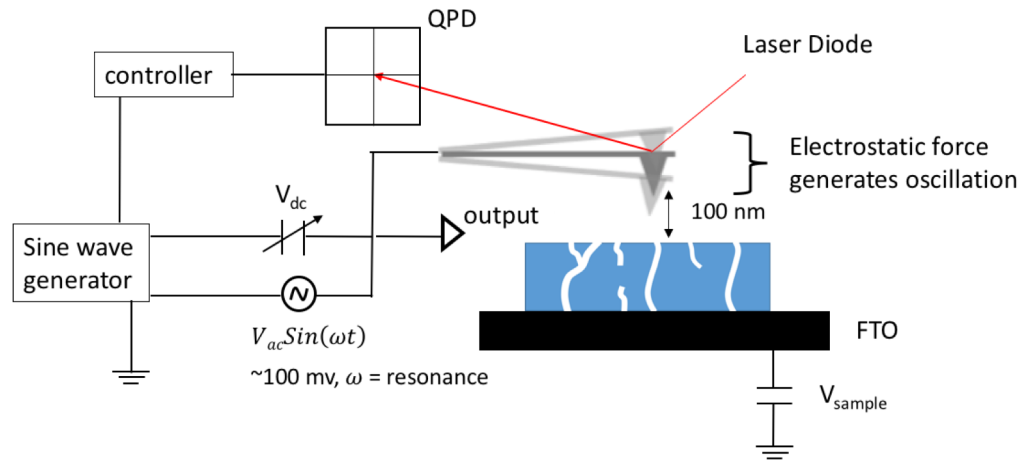
Figure A2.1: KPFM schematic

A schematic of the KPFM feedback system is shown in Figure A2.1. The primary difference between EFM and KPFM is that the cantilever is not mechanically driven, only the electrostatic force generates cantilever oscillation. An AC voltage (V_{ac}) and DC offset voltage (V_{dc}) is applied to the tip. The frequency of V_{ac} is set to the mechanical resonance of the cantilever ($\sim$ 300 kHz) with an amplitude of typically 100 mV. The KPFM feedback system seeks to minimize the amplitude of the cantilever oscillation by matching V_{dc} with the surface potential. This can be explained mathematically by treating the tip-sample system like a capacitor. The total potential is defined as the sum of the applied voltages and the surface potential.

$$V_{total} = V_{dc} + V_{ac}Sin(\omega t) + V_s \tag{A2.1}$$

Based on the derivations from chapter 3, the expression for the force can be derived.

$$F = \frac{1}{2}\frac{dC}{dz}\left(\left[(V_{dc} - Vs)^2 + \frac{1}{2}{V_{ac}}^2\right] + 2[(V_{dc} - Vs)V_{ac}Sin(\omega t)] - \left[\frac{1}{2}{V_{ac}}^2 Cos(2\omega t)\right]\right) \quad (A2.2)$$

The amplitude of the cantilever oscillation is detected by the quadrant photodiode (QPD). A lock-in amplifier that is built into the MFP-3D controller is used to detect the amplitude. It can be seen in Eqn. A2.2 that the electrostatic force is minimized when V_{dc}-V_s = 0.

The total surface potential of Nafion is due to a combination of proton surface charge density (σ), the applied sample voltage V_{sample}, the immobile SO_3^- charge, and the work function difference between the tip and the fluorocarbon matrix. If we assume that the potential due to the sulfonate groups and the fluorocarbon matrix contributes only a constant background, then several KPFM images acquired at different V_{sample} will allow us to determine σ.

B. Methods

Our sample preparation procedure was the same as in the EFM procedure described in Chapter 3. Briefly, 5% Nafion dispersion solution in isopropyl alcohol was prepared. A clean FTO was dipped into Nafion solution for 30 seconds and removed and air-dried. A bias wire connected the controller to the FTO via copper tape and alligator clips. The front-side of the controller has various user input/outputs. For the EFM and KPFM experiments, the "User0" output BNC connection was used to apply sample voltages.

Conductive Pt-coated AFM probes were used (Mikromash HQ:XSC11). The shortest probe was selected for KPFM (~300 kHz resonance), which has been found to be advantageous for attractive-mode imaging. As in EFM, KPFM imaging mode can be operated with the standard cantilever holder. The imaging mode is selected from the Mode Master panel. Prior to imaging, a standard cantilever tune is conducted, which is then followed by an electric tune. During the electric tune, a voltage is applied to the tip to generate a potential difference between the tip and the sample, which generates tip oscillation. The resonance frequency is set to the mechanical resonance of the cantilever and an electric tune amplitude of 1V was used to generate the tune. I have found that if the tune does not appear clean then a larger tune voltage is needed.

C. Calibration
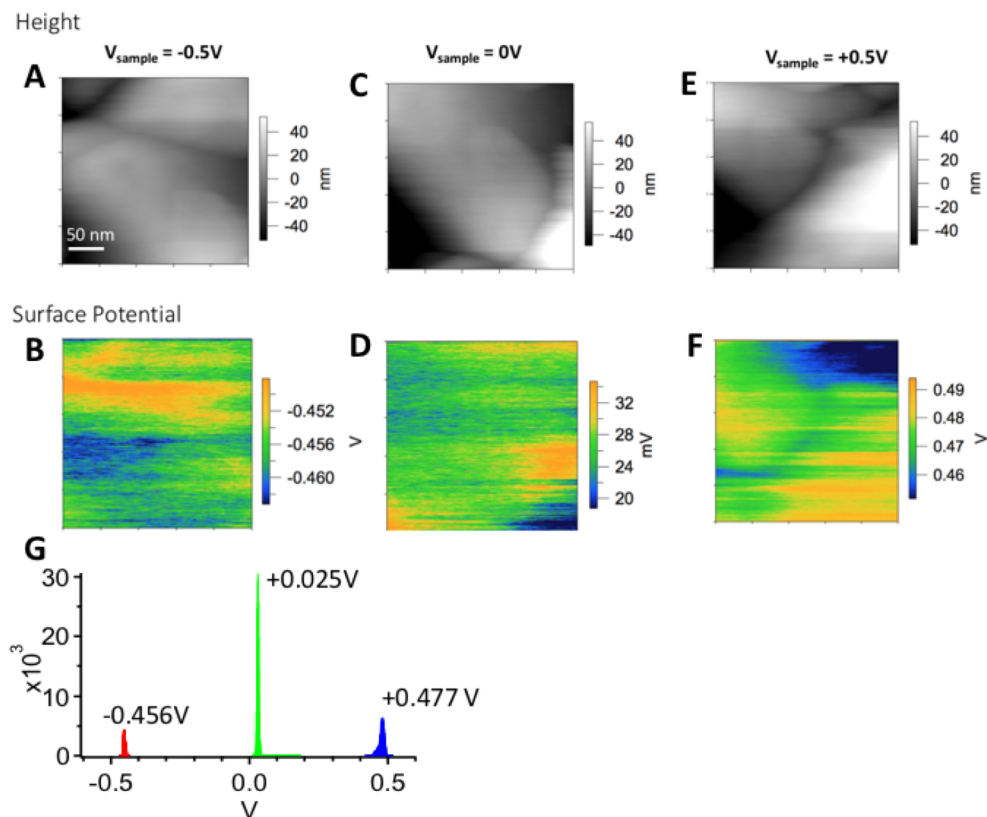
Figure A2.2: (A,C,E) Height and (B,D,F) KPFM calibration measurements of clean FTO at 3 different sample voltages at 50 nm lift height. (G) Distribution of surface potential at -0.5V (red), 0V (green), and +0.5V (blue).

    Calibration measurements were made on the conductive FTO substrate. Topography is shown in the top row while corresponding surface potential is shown in the middle row. Bias voltages were applied from the controller to the surface. Scan parameters including lift height, scan size, and scan speed were the same for the Nafion measurements. The order at which they were biased were also the same for the Nafion: -0.5V was acquired first, 0V second, +0.5V third. No drift was observed. The images show that variation in surface potential corresponds to changes in FTO topography.
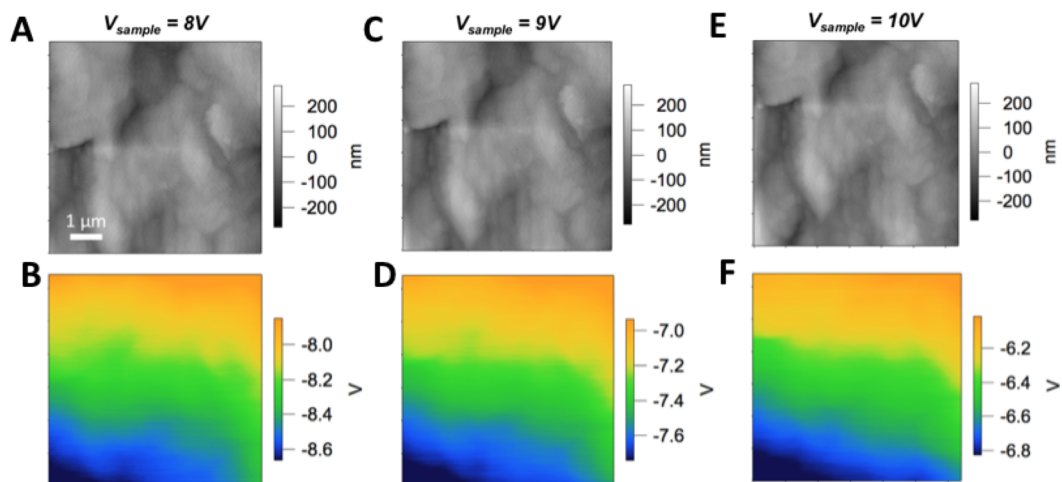
Figure A2.3: (Top row) Topography and (bottom row) surface potential were acquired at different sample biases.

The surface potential of neat Teflon using thick 100 micron sheets was measured to acquire an understanding of the overall negative surface potential background in Nafion and the effect of dielectric screening. We found that scanning at voltages at or close to 0V was not possible as a result of our AFM controller having a maximum voltage sensing range of +/- 10V. However, we could still observe negative potentials at high sample biases. Additionally, if we took the average surface potential and subtract from the sample bias for each image, a gradual decrease was observed: -16.23V, -16.341V, -16.423V, for 8V, 9V, and 10V respectively. This suggests that the Teflon film was screening charge near the surface, lowering the surface potential.

D. Analysis of Individual Hydrophilic Domains
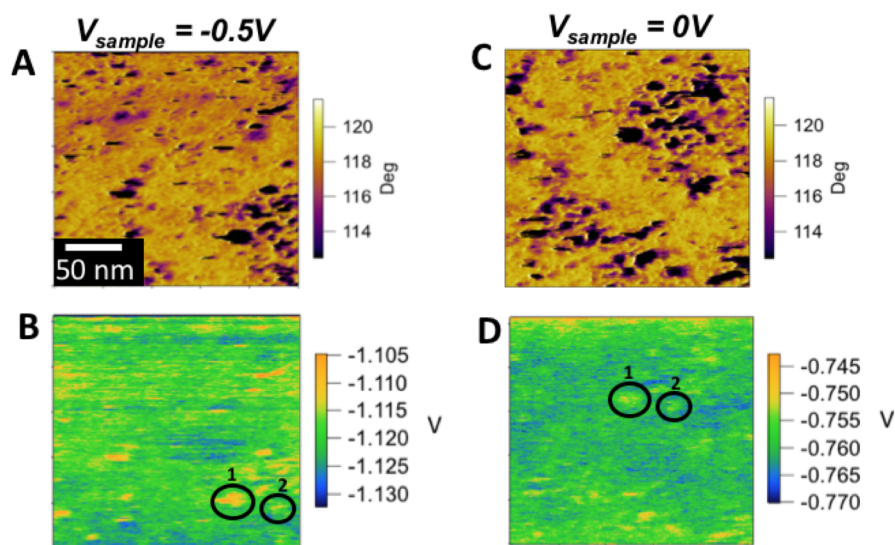
Figure A2.4: 200x200 nm AFM images of (A,C) 1st pass phase taken in attractive mode and (B,D) corresponding surface potential images taken at -0.5V (A,B) and 0V sample voltage (C,D). The lift height in the 2nd pass is 50 nm.

Figure A2.4 shows both first pass phase and second pass surface potential images under different biases. A lift height of 50 nm above attractive-mode (~55 nm above the surface) was used in all KPFM images. We imaged the same scan region under -0.5V and 0V bias and analyzed the surface potential of isolated channels. The same domains can be seen in both image sets. The surface potential of individual domains is more positive than the background, as expected since the aqueous domains contain the acidic protons. The contrast relative to the background is greater for the -0.5V KPFM image than the 0V. This is also expected since protons are pulled away from the surface under negative sample bias. The relative motion of mobile charges can be deduced from histograms of the surface potential for all aqueous domains at -0.5V and 0V shown in Fig. A2.5. At a negative sample bias, protons are depleted near the surface providing a strong contrast between the domains

and fluorocarbon matrix, especially for connected channels where dielectric screening is absent. that KPFM can be influenced by long-range electrostatic interactions, sampling beneath the surface may extend 10-100 nm,[92,164] but the influence of imbedded charges decays exponentially with tip-sample distance.[165,166] We believe that the influence of any subsurface charge is negligible for our lift height of 50 nm.
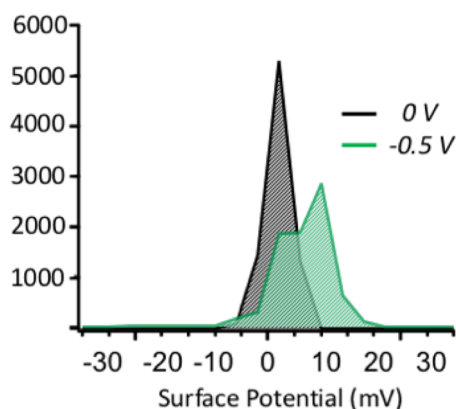
Figure A2.5: Distributions of surface potential of aqueous domains at 0V (black) and -0.5V (green) sample bias voltage.

The distribution in surface potential for the aqueous channels is shown in Fig. A2.5 for a 0V sample bias (black) and -0.5V sample bias (green). The histograms of Fig. A2.5 are derived from background subtracted KPFM images of Fig A2.4. Each aqueous domain is identified using the tapping-mode phase image of Fig A2.4. A mask is drawn around the aqueous channel to determine the channel surface area. The same area mask is then used to select the surface potential data in the corresponding KPFM image. The histograms of Fig. A2.5 represent data from ~ 20 individual channels and include 8169 points. It is useful to note that the size of the aqueous domains included in Fig. A2.4 range from 70 nm^2 to 250

145

nm^2. The histograms of Fig. A2.5 have a bias toward the larger domains, however, since the data is acquired for the same region of the sample a relative comparison of the surface potential distributions is valid.

A detailed understanding of the heterogeneity in σ can be gleaned from the shape of the histograms of Fig. A2.5. At 0V bias the distribution in KPFM signal for the aqueous domains is uniform and symmetric with an average signal slightly above the KPFM signal for the fluorocarbon matrix. At -0.5V, however, the distribution in KPFM signal becomes asymmetric relative to the maximum and is strongly skewed toward the background value. This result is attributed to the asymmetry in the charge depletion for each of the channels. At -0.5V bias protons are depleted near the surface. A long connected channel would result in a large depletion of protons near the surface, and this in turn results in a large surface potential and a large KPFM signal. By definition, a short dead-end channel would be separated from the electrode surface by the hydrophobic fluorocarbon matrix. The protons in the dead-end channels are thus screened from the electrode, which results in a smaller depletion of protons from the surface than for long, connected channels. This results in a much smaller change in the surface potential, is observed for dead-end channels then connected channels. Dielectric screening has been observed to reduce the surface potential in KPFM for other systems.[167] Thus, the channels with KPFM signal near the peak maximum represent connected channels (denoted by 1 in the image of Fig. A2.4B) and the channels with KPFM signal near the background signal represent dead-end channels (denoted by 2 in the image of Fig. A2.4B).

It is however important to note the spatial resolution of the KPFM images are comparable to the first pass phase images. Therefore, it is likely these spots of positive

146

charge are artifacts of the topography. This can be avoided by imaging with a greater lift-height, however the surface potential resolution decays with lift-height. Because of this, we turned our investigation to larger KPFM images with a greater lift-height (100 nm) and collected larger images in attempts to observe heterogeneity over longer ranges.

E. Analysis of Larger KPFM Images
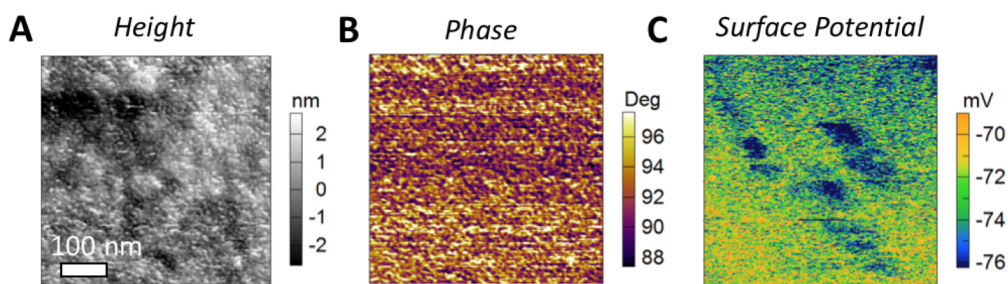
Figure A2.6: First pass images of the (A) height and (B) attractive-mode phase, and second pass image of the surface potential taken at a sample voltage of +0.5V.

Figure A2.6 shows a 500x500 nm AFM images with height and phase in the first pass and the surface potential gathered in the second pass with applied FTO sample voltage of +0.5V. While Figure A2.6A and B represents a typical height and phase image of Nafion, respectively, Figure A2.6C shows heterogeneity in the surface potential over a long range. In our analysis of individual domains, the surface potential contrast is bright (positive from the background). Here, we find large regions of dark contrast that ~4-6 mV less than the background surface potential. The regions of dark contrast in the surface potential image resembles the "worm-like" regions that have been previously observed of Nafion with cp-AFM under hydrated conditions.[23] It is possible that the dark contrast could represent

regions of trapped charge or "dead-end" channels within the Nafion membrane. In our EFM

investigation, we found that the appearance of dead-end and connected channels were

randomly dispersed. However, we were limited to a smaller scan and a smaller number of

regions of interest. What is also interesting about this data-set is that there is no indication of

the height or the phase influencing the surface potential. We investigated this further by

collecting larger KPFM images to observe the frequency of these extended regions.
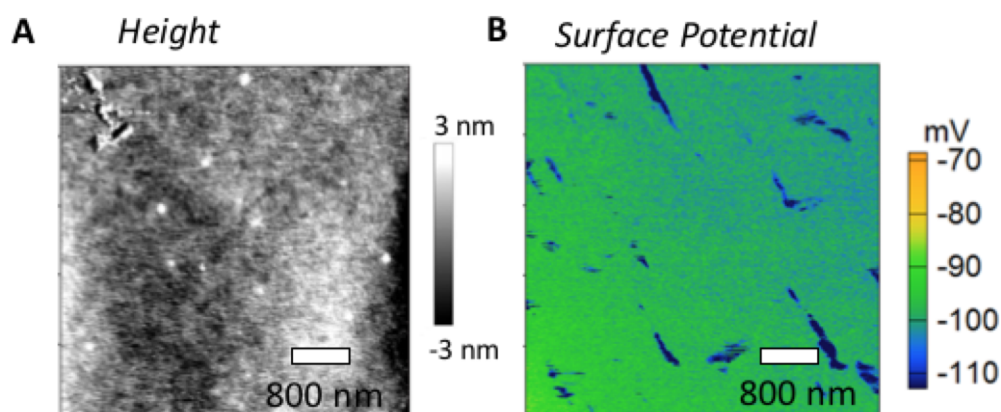
Figure A2.7: (A) First pass height and (B) second pass surface potential image of Nafion.

A 5x5 μm KPFM scan was collected in a similar location of this sample with the

same lift height of 100 nm and a sample voltage of +0.5V. Figure A2.7A shows a relatively

flat height image while Figure A2.7B continues to show the extended regions of dark

contrast. From this image, it is observed that these regions are 50-100 nm in width and

extend over a micron in length. Since images shown in Figure A2.7C and A2.7B are only at

+0.5V sample voltage, we turned our investigation to determine how these regions would

change in surface potential contrast depending on the change in V_{sample}.
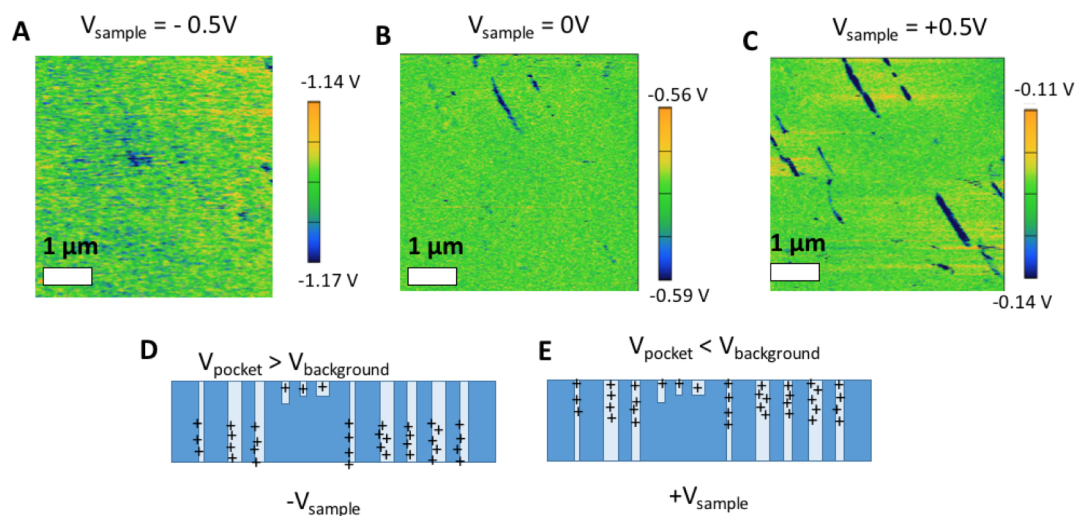
Figure A2.8: (A-C) Surface potential images of the same scan region at (A) -0.5V, (B) 0V, and (C) +0.5V sample voltage. (D,E) Cartoon of Nafion illustrating how the surface potential of the "dead-end" channels (V_{pocket}) change depending on V_{sample}. (D) At negative sample voltage, V_{pocket} is greater than or equal to the background surface potential ($V_{background}$). (E) At positive sample voltage, V_{pocket} is less than $V_{background}$.

Figure A2.8 shows how the surface potential contrast depends on V_{sample}. At -0.5V applied to the FTO, shown in Figure A2.8A, we observed a homogeneous surface potential and hence no extended dark regions were observed. The average surface potential background ($V_{background}$) was -1.15V, which is close to the $V_{background}$ shown in A2.4B. At 0V, shown in A2.8B, we began to observe the appearance of extended dark regions near the top of the image with $V_{background}$ shifting to -0.57V. At +0.5V, shown in A2.6C, we observed the strongest surface potential contrast with $V_{background}$ shifting to -0.125V. Cartoons of how variation in channel connectivity can give rise to differences in surface potential depending on the sample voltage is illustrated in Figure A2.6D-E. In both cartoons, the majority of the channels are connected throughout the membrane with the "dead-end" channels in the middle consisting of a pocket of charge. Illustrated in Figure A2.8D at negative V_{sample},

protons within the connected channels are depleted from the surface and migrate toward the bottom of the membrane while protons in the disconnected channels are trapped at the surface. This gives rise to a surface potential of the "dead-end" channels (V_{pocket}) greater than $V_{background}$. In this data-set, we did not see the contrast flip and appear bright as what was observed in Figure A2.4B. At more negative V_{sample}, the contrast might flip, we are limited to a range of -1.5V – +1.5V due to the strong piezo-like response of the Nafion membrane. In Figure A2.8E at positive V_{sample}, protons within the connected channels migrate toward the top of the membrane while protons remain trapped at the surface. This gives rise to a V_{pocket} less than $V_{background}$.
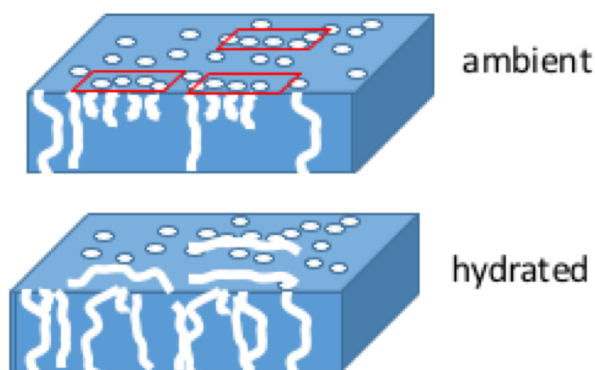
Figure A2.9: Cartoon of Nafion under ambient and hydrated conditions illustrating proposed seeding mechanism for the formation of extended "worm-like" surface structures.

If the "dead-end" channels are clustered together in extended regions under ambient conditions, this provides insight toward how these regions grow and dominate the surface under hydrated conditions. Figure A2.9 shows a cartoon of a proposed model for the formation of extended "worm-like" surface structures that has been observed previously.[23,74]

The cartoon shows how the disconnected channels are arranged as highlighted in red. It is possible that these regions could coalesce to form the micron scale features observed under pre-boiled and hydrated conditions.

F. Conclusions and Future Directions

KPFM of Nafion provides a direct measurement of the surface potential from the nanometer to micron length scale. In our pursuits to measure how the surface potential of individual hydrophilic domains depend on the change in the surface potential, we came across too many imaging artifacts, which was likely a result of the low lift-height. At larger lift-heights and larger scan sizes we observed extended features with dark surface potential contrast ranging 100 nm-1 μm in length. These regions of dark contrast were not influenced by the first pass topography or phase. We found that the surface potential contrast depends on the sign of V_{sample}.

What remains to be seen is if these features become more prevalent after pre-treating the membrane. It has been shown that when Nafion 212 is boiled in 1.0 M H_2SO_4 for 1 hour followed by boiling in DI for 1 hour and equilibrated under 95% RH, "worm-like" features dominate the surface. [23,74] We have also shown similar features of hydrated FAA-3 in Chapter 4. Control experiments must be conducted to understand how the surface potential depends on the RH and IEC. At low RH one would anticipate a more negative surface potential due to a fluorocarbon-rich surface and the lack of mobile protons that can migrate toward the surface. One would also expect more disconnected channels, which would give rise to increased heterogeneity in the surface potential. At high RH, the channels become more connected and saturated with water. Hence, protons can easily migrate toward the surface giving rise to a more uniform and positive surface potential. A similar effect would

take place with samples varying in IEC. When ordering the Nafion dispersion solution from Fuel Cell Store, two types can be ordered: 0.95meq/g and 1.03 meq/g. In work reported here, we used 0.95 meq/g (1100 EW). Higher IEC membranes are more likely to form connected channels because there are more sulfonic acid side chains per gram of fluorocarbon backbone. Therefore, one would anticipate a shift toward a more positive and uniform surface potential. Both of these experiments would be important controls to verify if these extended regions are inherent to the membrane, and provide quantitative method for measuring the surface potential as a function of RH and IEC.

Appendix 3: EFM of Clean FTO

EFM measurements of clean FTO were made to understand how the dielectric permittivity of air influences the parabolic EFM response as a function of bias voltage. FTO also serves as a good calibration sample for EFM measurements because the FTO voltage can be measured with a voltmeter. Figure A3.1 shows the first pass height image and second pass EFM phase image. Figure A3.1B was taken at 350 mV. The same region was scanned at 7 different voltages to construct the parabolic EFM response. All EFM images were taken at a lift-height of 100 nm from the surface.
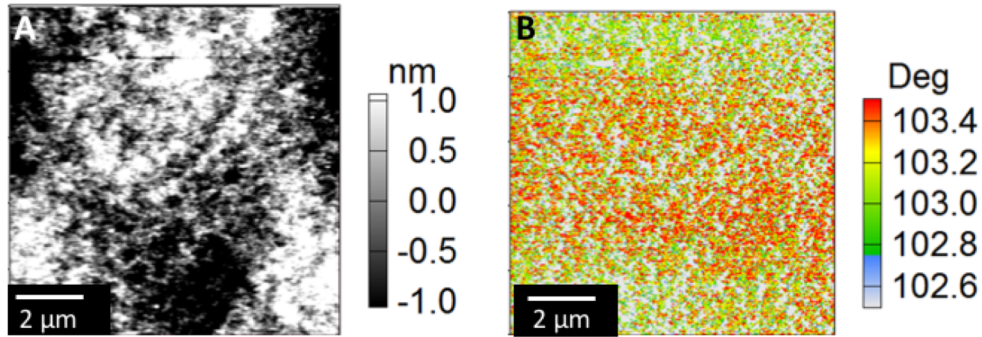
Figure A3.1: (A) Height and (B) 2nd pass EFM phase image of FTO at V$_{EFM}$ = 350 mV and 100 nm lift-height.

The parabolic EFM response as a function of V$_{EFM}$ of clean FTO is shown in Figure A3.1. We have defined V$_{EFM}$ = V$_{tip}$ – V$_{FTO}$. In our experiments, V$_{tip}$ is grounded, therefore V$_{EFM}$ = - V$_{FTO}$. Each data point represents the average EFM phase of an entire 10 x 10 μm image. The data was plotted and fit to a quadratic in Igor Pro. A and B are the linear and quadratic fitting parameters, respectively. The linear fit term was A = 0.47 °/V and the quadratic fit term was B = -7.17 °/V^2.
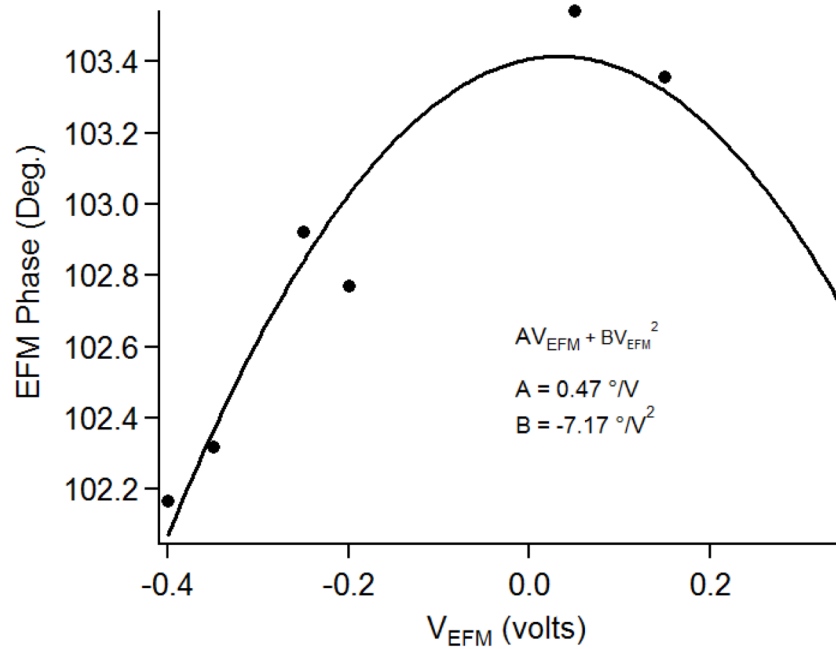
Figure A3.2: Average EFM phase of the same scan region of image A3.1 at 7 different sample voltages. The conductive tip and FTO form a capacitor with air as the dielectric medium. Hence, a quadratic curve can be fit to the data. The linear and quadratic fit of the curve are denoted as A and B, respectively.

References

(1)   Song, C.; Zhang, J. Electrocatalytic Oxygen Reduction Reaction. In *PEM Fuel Cell Electrocatalysts and Catalyst Layers*; Springer London: London, 2008; pp 89–134.

(2)   Duffy, M. *Fuel Cell System Cost for Transportation-2008 Cost Estimate (Revised), Independent Review, Published for the U.S. Department of Energy Hydrogen Program (Book)*; 2009.

(3)   Litster, S.; McLean, G. PEM Fuel Cell Electrodes. *J. Power Sources* **2004**, *130* (1–2),

61–76.

(4)   Cooper, C. D.; Burk, J. J.; Taylor, C. P.; Buratto, S. K. Ultra-Low Pt Loading Catalyst
        Layers Prepared by Pulse Electrochemical Deposition for PEM Fuel Cells. *J. Appl.
        Electrochem.* **2017**, *47* (6), 699–709.

(5)   Dai, L.; Xue, Y.; Qu, L.; Choi, H.-J.; Baek, J.-B. Metal-Free Catalysts for Oxygen
        Reduction Reaction. *Chem. Rev.* **2015**, *115* (11), 4823–4892.

(6)   Gong, K.; Du, F.; Xia, Z.; Durstock, M.; Dai, L. Nitrogen-Doped Carbon Nanotube
        Arrays with High Electrocatalytic Activity for Oxygen Reduction. *Science* **2009**, *323*
        (5915), 760–764.

(7)   Varcoe, J. R.; Slade, R. C. T.; Wright, G. L.; Chen, Y. Steady-State Dc and
        Impedance Investigations of H2/O2 Alkaline Membrane Fuel Cells with Commercial
        Pt/C, Ag/C, and Au/C Cathodes. *J. Phys. Chem. B* **2006**, *110* (42), 21041–21049.

(8)   Mauritz, K. A.; Moore, R. B. State of Understanding of Nafion. *Chem. Rev.* **2004**,
        104 (10), 4535–4586.

(9)   Zawodzinski, T. A.; Derouin, C.; Radzinski, S.; Sherman, R. J.; Smith, V. T.;
        Springer, T. E.; Gottesfeld, S. Water Uptake by and Transport Through Nafion® 117
        Membranes. *J. Electrochem. Soc.* **1993**, *140* (4), 1041.

(10)   Paddison, S. J.; Paul, R. The Nature of Proton Transport in Fully Hydrated Nafion®.
        Phys. Chem. Chem. Phys. **2002**, *4* (7), 1158–1163.

(11)   Choi, P.; Jalani, N. H.; Datta, R. Thermodynamics and Proton Transport in Nafion. *J.
        Electrochem. Soc.* **2005**, *152* (3), E123.

(12)   Weber, A. Z.; Newman, J. Transport in Polymer-Electrolyte Membranes. *J.
        Electrochem. Soc.* **2003**, *150* (7), A1008.

(13)   Rubatat, L.; Gebel, G.; Diat, O. Fibrillar Structure of Nafion: Matching Fourier and Real Space Studies of Corresponding Films and Solutions. *Macromolecules* **2004**, *37* (20), 7772–7783.

(14)   Schmidt-Rohr, K.; Chen, Q. Parallel Cylindrical Water Nanochannels in Nafion Fuel-Cell Membranes. *Nat. Mater.* **2007**, *7* (1), 75–83.

(15)   Hsu, W. Y.; Gierke, T. D. Ion Transport and Clustering in Nafion Perfluorinated Membranes. *J. Memb. Sci.* **1983**, *13* (3), 307–326.

(16)   Gostick, J. T.; Weber, A. Z. Resistor-Network Modeling of Ionic Conduction in Polymer Electrolytes. *Electrochim. Acta* **2015**, *179*, 137–145.

(17)   Elliott, J. A.; Wu, D.; Paddison, S. J.; Moore, R. B. A Unified Morphological Description of Nafion Membranes from SAXS and Mesoscale Simulations. *Soft Matter* **2011**, *7* (15), 6820.

(18)   Rubatat, L.; Rollet, A. L.; Gebel, G.; Diat, O. Evidence of Elongated Polymeric Aggregates in Nafion. *Macromolecules* **2002**, *35* (10), 4050–4055.

(19)   Schmidt-Rohr, K.; Chen, Q. Parallel Cylindrical Water Nanochannels in Nafion Fuel-Cell Membranes. *Nat. Mater.* **2008**, *7* (1), 75–83.

(20)   Allen, F. I.; Comolli, L. R.; Kusoglu, A.; Modestino, M. A.; Minor, A. M.; Weber, A. Z. Morphology of Hydrated As-Cast Nafion Revealed through Cryo Electron Tomography. *ACS Macro Lett.* **2015**, *4* (1), 1–5.

(21)   Xue, T.; Trent, J. S.; Osseo-Asare, K. Characterization of Nafion® Membranes by Transmission Electron Microscopy. *J. Memb. Sci.* **1989**, *45* (3), 261–271.

(22)   James, P. J.; Antognozzi, M.; Tamayo, J.; McMaster, T. J.; Newton, J. M.; Miles, M. J. Interpretation of Contrast in Tapping Mode AFM and Shear Force Microscopy. A

Study of Nafion. *Langmuir* **2001**, *17* (2), 349–360.

(23)   O'Dea, J. R.; Economou, N. J.; Buratto, S. K. Surface Morphology of Nafion at Hydrated and Dehydrated Conditions. *Macromolecules* **2013**, *46* (6), 2267–2274.

(24)   O'Dea, J. R.; Buratto, S. K. Phase Imaging of Proton Exchange Membranes under Attractive and Repulsive Tip−Sample Interaction Forces. *J. Phys. Chem. B* **2011**, *115* (5), 1014–1020.

(25)   Tamayo, J.; García, R. Relationship between Phase Shift and Energy Dissipation in Tapping-Mode Scanning Force Microscopy. *Appl. Phys. Lett.* **1998**, *73* (20), 2926.

(26)   David A. Bussian; James R. O'Dea; Horia Metiu, A.; Buratto*, S. K. Nanoscale Current Imaging of the Conducting Channels in Proton Exchange Membrane Fuel Cells. *Nano Lett.* **2007**, *7* (2), 227–232.

(27)   Nicholas Economou. Investigation of Morphology and Proton Conductivity in Proton Exchange Membranes under Variable Operating Conditions by Atomic Force Microscopy, University of California, Santa Barbara, 2014.

(28)   Economou, N. J.; Barnes, A. M.; Wheat, A. J.; Schaberg, M. S.; Hamrock, S. J.; Buratto, S. K. Investigation of Humidity Dependent Surface Morphology and Proton Conduction in Multi-Acid Side Chain Membranes by Conductive Probe Atomic Force Microscopy. *J. Phys. Chem. B* **2015**, *119* (44), 14280–14287.

(29)   Merle, G.; Wessling, M.; Nijmeijer, K. Anion Exchange Membranes for Alkaline Fuel Cells: A Review. *J. Memb. Sci.* **2011**, *377* (1–2), 1–35.

(30)   Varcoe, J. R.; Slade, R. C. T. Prospects for Alkaline Anion-Exchange Membranes in Low Temperature Fuel Cells. *Fuel Cells* **2005**, *5* (2), 187–200.

(31)   Hickner, M. A.; Herring, A. M.; Coughlin, E. B. Anion Exchange Membranes:

Current Status and Moving Forward. *J. Polym. Sci. Part B Polym. Phys.* **2013**, *51* (24), 1727–1735.

(32)   Weber, A. Z.; Newman, J. Modeling Transport in Polymer-Electrolyte Fuel Cells. *Chem. Rev.* **2004**, *104* (10), 4679–4726.

(33)   Marx, D.; Chandra, A.; Tuckerman, M. E. Aqueous Basic Solutions: Hydroxide Solvation, Structural Diffusion, and Comparison to the Hydrated Proton.

(34)   Marino, M. G.; Melchior, J. P.; Wohlfarth, A.; Kreuer, K. D. Hydroxide, Halide and Water Transport in a Model Anion Exchange Membrane. **2014**.

(35)   Siroma, Z.; Watanabe, S.; Yasuda, K.; Fukuta, K.; Yanagi, H. Mathematical Modeling of the Concentration Profile of Carbonate Ions in an Anion Exchange Membrane Fuel Cell. *J. Electrochem. Soc.* **2011**, *158* (6), B682.

(36)   Sata, T.; Tsujimoto, M.; Yamaguchi, T.; Matsusaki, K. Change of Anion Exchange Membranes in an Aqueous Sodium Hydroxide Solution at High Temperature. *J. Memb. Sci.* **1996**, *112* (2), 161–170.

(37)   Kreuer, K.-D.; Jannasch, P. A Practical Method for Measuring the Ion Exchange Capacity Decrease of Hydroxide Exchange Membranes during Intrinsic Degradation. *J. Power Sources* **2018**, *375*, 361–366.

(38)   Zhang, W.; Liu, Y.; Jackson, A. C.; Savage, A. M.; Ertem, S. P.; Tsai, T.-H.; Seifert, S.; Beyer, F. L.; Liberatore, M. W.; Herring, A. M.; Coughlin, E. B. Achieving Continuous Anion Transport Domains Using Block Copolymers Containing Phosphonium Cations. *Macromolecules* **2016**, *49* (13), 4714–4722.

(39)   Ding, J.; Chuy, C.; Holdcroft, S. Enhanced Conductivity in Morphologically Controlled Proton Exchange Membranes: Synthesis of Macromonomers by SFRP and

Their Incorporation into Graft Polymers. *Macromolecules* **2002**, *35* (4), 1348–1355.

(40) Park, M. J.; Kim, S.; Minor, A. M.; Hexemer, A.; Balsara, N. P. Control of Domain
      Orientation in Block Copolymer Electrolyte Membranes at the Interface with Humid
      Air. *Adv. Mater.* **2009**, *21* (2), 203–208.

(41) Hibbs, M. R.; Hickner, M. A.; Alam, T. M.; McIntyre, S. K.; Fujimoto, C. H.;
      Cornelius, C. J. Transport Properties of Hydroxide and Proton Conducting
      Membranes. *Chem. Mater.* **2008**, *20* (7), 2566–2573.

(42) Noonan, K. J. T.; Hugar, K. M.; Kostalik, H. A.; Lobkovsky, E. B.; Abruña, H. D.;
      Coates, G. W. Phosphonium-Functionalized Polyethylene: A New Class of Base-
      Stable Alkaline Anion Exchange Membranes. *J. Am. Chem. Soc.* **2012**, *134* (44),
      18161–18164.

(43) Wang, Y.; Chen, K. S.; Mishler, J.; Cho, S. C.; Adroher, X. C. A Review of Polymer
      Electrolyte Membrane Fuel Cells: Technology, Applications, and Needs on
      Fundamental Research. *Appl. Energy* **2011**, *88* (4), 981–1007.

(44) Smitha, B.; Sridhar, S.; Khan, A. A. Solid Polymer Electrolyte Membranes for Fuel
      Cell Applications—a Review. *J. Memb. Sci.* **2005**, *259* (1–2), 10–26.

(45) Hamrock, S. J.; Yandrasits, M. A. Proton Exchange Membranes for Fuel Cell
      Applications. *J. Macromol. Sci. Part C Polym. Rev.* **2006**, *46* (3), 219–244.

(46) Parthasarathy, A.; Srinivasan, S.; Appleby, A. J.; Martin, C. R. Temperature
      Dependence of the Electrode Kinetics of Oxygen Reduction at the Platinum/Nafion®
      Interface—A Microelectrode Investigation. *J. Electrochem. Soc.* **1992**, *139* (9), 2530.

(47) Gottesfeld, S.; Pafford, J. *A New Approach to the Problem of Carbon Monoxide
      Poisoning in Fuel Cells Operating at Low Temperatures*.

(48) Zawodzinski, T. A.; Springer, T. E.; Davey, J.; Jestel, R.; Lopez, C.; Valerio, J.; Gottesfeld, S. A Comparative Study of Water Uptake By and Transport Through Ionomeric Fuel Cell Membranes. *J. Electrochem. Soc.* **1993**, *140* (7), 1981.

(49) Shawn J. Osborn; Mohammad K. Hassan, †; Gilles M. Divoux; David W. Rhoades; Kenneth A. Mauritz, A.; Moore*, R. B. Glass Transition Temperature of Perfluorosulfonic Acid Ionomers. *Macromolecules* **2007**, *40*, 3886–3890.

(50) Zhang, S.; Dou, S.; Colby, R. H.; Runt, J. Glass Transition and Ionic Conduction in Plasticized and Doped Ionomers. *J. Non. Cryst. Solids* **2005**, *351* (33–36), 2825–2830.

(51) Tant, M. R.; Darst, K. P.; Lee, K. D.; Martin, C. W. Structure and Properties of Short-Side-Chain Perfluorosulfonate Ionomers. In *ACS Symposium Series 395; American Chemical Society: Washington, DC*; 1989; pp 370–400.

(52) Nandan, D.; Mohan, H.; Iyer, R. M. Methanol and Water Uptake, Densities, Equivalental Volumes and Thicknesses of Several Uni- and Divalent Ionic Perfluorosulphonate Exchange Membranes (Nafion-117) and Their Methanol-Water Fractionation Behaviour at 298 K. *J. Memb. Sci.* **1992**, *71* (1–2), 69–80.

(53) Adjemian, K. T.; Lee, S. J.; Srinivasan, S.; Benziger, J.; Bocarsly, A. B. Silicon Oxide Nafion Composite Membranes for Proton-Exchange Membrane Fuel Cell Operation at 80-140°C. *J. Electrochem. Soc.* **2002**, *149* (3), A256.

(54) Gibbons, J. F.; Hess, L. D. (Laverne D.; Sigmon, T. W.; Materials Research Society. Annual Meeting (1980 : Boston, M. .; Miyayama, M. *Influence of Titania Morphology on the Electrochemical Properties of Composite Polymer Electrolyte Membranes.*; North Holland, 1981; Vol. 1126.

(55) Titvinidze, G.; Wohlfarth, A.; Kreuer, K.-D.; Schuster, M.; Meyer, W. H. Reinforcement of Highly Proton Conducting Multi-Block Copolymers by Online Crosslinking. *Fuel Cells* **2014**, *14* (2), 325–331.

(56) Guo, Q.; N. Pintauro, P.; Tang, H.; O'Connor, S. Sulfonated and Crosslinked Polyphosphazene-Based Proton-Exchange Membranes. *J. Memb. Sci.* **1999**, *154* (2), 175–181.

(57) Ye, Y.-S.; Yen, Y.-C.; Cheng, C.-C.; Chen, W.-Y.; Tsai, L.-T.; Chang, F.-C. Sulfonated Poly(Ether Ether Ketone) Membranes Crosslinked with Sulfonic Acid Containing Benzoxazine Monomer as Proton Exchange Membranes. *Polymer (Guildf).* **2009**, *50* (14), 3196–3203.

(58) Mikhailenko, S. D.; Wang, K.; Kaliaguine, S.; Xing, P.; Robertson, G. P.; Guiver, M. D. Proton Conducting Membranes Based on Cross-Linked Sulfonated Poly(Ether Ether Ketone) (SPEEK). *J. Memb. Sci.* **2004**, *233* (1–2), 93–99.

(59) H. Liu, C.K. Mittelsteadt, T.J. Norman, A.E. Griffith, A. B. L. Solid Polymer Electrolyte Composite Membrane Comprising a Porous Support and a Solid Polymer Electrolyte Including a Dispersed Reduced Noble Metal or Noble Metal Oxide, October 4, 2015.

(60) Schaberg, M. S.; Abulu, J. E.; Haugen, G. M.; Emery, M. A.; O'Conner, S. J.; Xiong, P. N.; Hamrock, S. New Multi Acid Side-Chain Ionomers for Proton Exchange Membrane Fuel Cells. In *ECS Transactions*; The Electrochemical Society, 2010; Vol. 33, pp 627–633.

(61) Hamrock, S. *U.S. Department of Energy Hydrogen Program 2011 Annual Merit Review Proceedings.*; 2011.

(62)   Clark II, J. K.; Paddison, S. J. Proton Dissociation and Transfer in Proton Exchange Membrane Ionomers with Multiple and Distinct Pendant Acid Groups: An Ab Initio Study. *Electrochim. Acta* **2013**, *101*, 279–292.

(63)   A. Elliott, J.; Wu, D.; J. Paddison, S.; B. Moore, R. A Unified Morphological Description of Nafion Membranes from SAXS and Mesoscale Simulations. *Soft Matter* **2011**, *7* (15), 6820–6827.

(64)   Takimoto, N.; Wu, L.; Ohira, A.; Takeoka, Y.; Rikukawa, M. Hydration Behavior of Perfluorinated and Hydrocarbon-Type Proton Exchange Membranes: Relationship between Morphology and Proton Conduction. *Polymer (Guildf).* **2009**, *50* (2), 534–540.

(65)   Affoune, A. M.; Yamada, A.; Umeda, M. Letters Surface Observation of Solvent-Impregnated Nafion Membrane with Atomic Force Microscopy. *Langmuir* **2004**, *20* (17), 6965–6968.

(66)   Affoune, A. M.; Yamada, A.; Umeda, M. Conductivity and Surface Morphology of Nafion Membrane in Water and Alcohol Environments. *J. Power Sources* **2005**, *148*, 9–17.

(67)   He, Q.; Kusoglu, A.; Lucas, I. T.; Clark, K.; Weber, A. Z.; Kostecki, R. Correlating Humidity-Dependent Ionically Conductive Surface Area with Transport Phenomena in Proton-Exchange Membranes. *J. Phys. Chem. B* **2011**, *115*, 11650–11657.

(68)   Aleksandrova, E.; Hiesgen, R.; Andreas Friedrich, K.; Roduner, E. Electrochemical Atomic Force Microscopy Study of Proton Conductivity in a Nafion Membrane. *Phys. Chem. Chem. Phys.* **2007**, *9* (21), 2735.

(69)   Mclean, R. S.; Sauer, B. B. Tapping-Mode AFM Studies Using Phase Detection for

Resolution of Nanophases in Segmented Polyurethanes and Other Block Copolymers. *Macromolecules* **1997**, *30* (26), 8314–8317.

(70)   James, P. J.; Elliott, J. A.; McMaster, T. J.; Newton, J. M.; Elliott, A. M. S.; Hanna, S.; Miles, M. J. Hydration of Nafion® Studied by AFM and X-Ray Scattering. *J. Mater. Sci.* **2000**, *35* (20), 5111–5119.

(71)   Liu, Y.; Horan, J. L.; Schlichting, G. J.; Caire, B. R.; Liberatore, M. W.; Hamrock, S. J.; Haugen, G. M.; Yandrasits, M. A.; Seifert, N.; Herring, A. M. A Small-Angle X-Ray Scattering Study of the Development of Morphology in Films Formed from the 3M Perfluorinated Sulfonic Acid Ionomer. *Macromolecules* **2012**, *45* (18), 7495–7503.

(72)   Paddison, S. J.; Elliott, J. A. On the Consequences of Side Chain Flexibility and Backbone Conformation on Hydration and Proton Dissociation in Perfluorosulfonic Acid Membranes. *Phys. Chem. Chem. Phys.* **2006**, *8* (18), 2193.

(73)   Picture Thresholding Using an Iterative Selection Method. *IEEE Trans. Syst. Man. Cybern.* **1978**, *8* (8), 630–632.

(74)   Economou, N. J.; O'Dea, J. R.; McConnaughy, T. B.; Buratto, S. K. Morphological Differences in Short Side Chain and Long Side Chain Perfluorosulfonic Acid Proton Exchange Membranes at Low and High Water Contents. *RSC Adv.* **2013**, *3* (42), 19525.

(75)   Hsu, W. Y.; Gierke, T. D. Ion Transport and Clustering in Nafion Perfluorinated Membranes. *J. Memb. Sci.* **1983**, *13* (3), 307–326.

(76)   Gierke, T. D.; Munn, G. E.; Wilson, F. C. The Morphology in Nafion Perfluorinated Membrane Products, as Determined by Wide- and Small-Angle x-Ray Studies. *J.*

Polym. Sci. Polym. Phys. Ed. **1981**, *19* (11), 1687–1704.

(77) Hiesgen, R.; Wehl, I.; Aleksandrova, E.; Roduner, E.; Bauder, A.; Friedrich, K. A. Nanoscale Properties of Polymer Fuel Cell Materials-A Selected Review. *Int. J. Energy Res.* **2009**, *34* (14), 1223–1238.

(78) Mclean, R. S.; Sauer, B. B. *Tapping-Mode AFM Studies Using Phase Detection for Resolution of Nanophases in Segmented Polyurethanes and Other Block Copolymers*; 1997.

(79) Kreuer, K.-D. The Role of Internal Pressure for the Hydration and Transport Properties of Ionomers and Polyelectrolytes. *Solid State Ionics* **2013**, *252*, 93–101.

(80) Kusoglu, A.; Kienitz, B. L.; Weber, A. Z. Understanding the Effects of Compression and Constraints on Water Uptake of Fuel-Cell Membranes. *J. Electrochem. Soc.* **2011**, *158* (12), B1504.

(81) Springer, T. E.; Zawodzinski, T. A.; Gottesfeld, S. Polymer Electrolyte Fuel Cell Model. *J. Electrochem. Soc.* **1991**, *138* (8), 2334.

(82) He, W.; Yi, J. S.; Van Nguyen, T. Two-Phase Flow Model of the Cathode of PEM Fuel Cells Using Interdigitated Flow Fields. *AIChE J.* **2000**, *46* (10), 2053–2064.

(83) Wilson, M. S.; Gottesfeld, S. Thin-Film Catalyst Layers for Polymer Electrolyte Fuel Cell Electrodes. *J. Appl. Electrochem.* **1992**, *22* (1), 1–7.

(84) Komarov, P. V; Khalatur, P. G.; Khokhlov, A. R. Large-Scale Atomistic and Quantum-Mechanical Simulations of a Nafion Membrane: Morphology, Proton Solvation and Charge Transport. *Beilstein J. Nanotechnol.* **2013**, *4* (1), 567–587.

(85) Sone, Y.; Ekdunge, P.; Simonsson, D. Proton Conductivity of Nafion 117 as Measured by a Four-Electrode AC Impedance Method. *J. Electrochem. Soc.* **1996**,

143 (4), 1254.

(86)   Aleksandrova, E.; Hiesgen, R.; Andreas Friedrich, K.; Roduner, E. Electrochemical

Atomic Force Microscopy Study of Proton Conductivity in a Nafion Membrane.

Phys. Chem. Chem. Phys. **2007**, *9* (21), 2735.

(87)   Barth, C.; Foster, A. S.; Henry, C. R.; Shluger, A. L. Recent Trends in Surface

Characterization and Chemistry with High-Resolution Scanning Force Methods. *Adv.*

Mater. **2011**, *23* (4), 477–501.

(88)   Cherniavskaya, O.; Chen, L.; Weng, V.; Yuditsky, L.; Brus, L. E. Quantitative

Noncontact Electrostatic Force Imaging of Nanocrystal Polarizability. *J. Phys. Chem.*

B **2003**, *107* (7), 1525–1531.

(89)   Malvankar, N. S.; Yalcin, S. E.; Tuominen, M. T.; Lovley, D. R. Visualization of

Charge Propagation along Individual Pili Proteins Using Ambient Electrostatic Force

Microscopy. *Nat. Nanotechnol.* **2014**, *9* (12), 1012–1017.

(90)   Krishnan, R.; Hahn, M. A.; Yu, Z.; Silcox, J.; Fauchet, P. M.; Krauss, T. D.

Polarization Surface-Charge Density of Single Semiconductor Quantum Rods. *Phys.*

Rev. Lett. **2004**, *92* (21), 216803.

(91)   Schaadt, D. M.; Yu, E. T.; Sankar, S.; Berkowitz, A. E. Charge Storage in Co

Nanoclusters Embedded in SiO2 by Scanning Force Microscopy. *Appl. Phys. Lett*

1999, *74* (3), 472–474.

(92)   Rumberger, B.; Bennett, M.; Zhang, J.; Dura, J. A.; Israeloff, N. E. Communication:

Nanoscale Ion Fluctuations in Nafion Polymer Electrolyte. *J. Chem. Phys.* **2014**, *141*

(7), 071102.

(93)   O'Hayre, R.; Lee, M.; Prinz, F. B. Ionic and Electronic Impedance Imaging Using

Atomic Force Microscopy. *J. Appl. Phys.* **2004**, *95* (12), 8382–8392.

(94) Mélin, T.; Zdrojek, M.; Brunel, D. Electrostatic Force Microscopy and Kelvin Force Microscopy as a Probe of the Electrostatic and Electronic Properties of Carbon Nanotubes. In *Scanning Probe Microscopy in Nanoscience and Nanotechnology*; Springer, Berlin, Heidelberg, 2010; pp 89–128.

(95) Kim, S.; No, K.; Hong, S. Visualization of Ion Transport in Nafion Using Electrochemical Strain Microscopy. *Chem. Commun.* **2016**, *52* (4), 831–834.

(96) Mélin, T.; Diesinger, H.; Deresmes, D.; Stiévenard, D. Electric Force Microscopy of Individually Charged Nanoparticles on Conductors: An Analytical Model for Quantitative Charge Imaging. *Phys. Rev. B* **2004**, *69* (3), 035321.

(97) Martin, Y.; Abraham, D. W.; Kumar Wickramasinghe, H. High-Resolution Capacitance Measurement and Potentiometry by Force Microscopy. *Appl. Phys. Lett* **1988**, *52*, 1103.

(98) Belaidi, S.; Girard, P.; Leveque, G. Electrostatic Forces Acting on the Tip in Atomic Force Microscopy: Modelization and Comparison with Analytic Expressions. *J. Appl. Phys.* **1997**, *81*, 1023.

(99) Belaidi, S.; Lebon, F.; Girard, P.; Leveque, G.; Pagano, S. *Finite Element Simulations of the Resolution in Electrostatic Force Microscopy*; 1998; Vol. 66.

(100) Sacha, G. M.; Sahagún, E.; Sáenz, J. J. A Method for Calculating Capacitances and Electrostatic Forces in Atomic Force Microscopy. *J. Appl. Phys* **2007**, *101*, 24310.

(101) Eikerling, M.; Kornyshev, A. A.; Kuznetsov, A. M.; Ulstrup, J.; Walbran, S. Mechanisms of Proton Conductance in Polymer Electrolyte Membranes. **2001**.

(102) Berg, P.; Benjaminsen, B. E. Effects of Finite-Size Ions and Relative Permittivity in a

Nanopore Model of a Polymer Electrolyte Membrane. *Electrochim. Acta* **2014**, *120*, 429–438.

(103) Carmo, M.; Doubek, G.; Sekol, R. C.; Linardi, M.; Taylor, A. D. Development and Electrochemical Studies of Membrane Electrode Assemblies for Polymer Electrolyte Alkaline Fuel Cells Using FAA Membrane and Ionomer. *J. Power Sources* **2013**, *230*, 169–175.

(104) Britton, B.; Holdcroft, S. The Control and Effect of Pore Size Distribution in AEMFC Catalyst Layers. *J. Electrochem. Soc.* **2016**, *163* (5), F353–F358.

(105) Yang, Z.; Zhou, J.; Wang, S.; Hou, J.; Wu, L.; Xu, T. A Strategy to Construct Alkali-Stable Anion Exchange Membranes Bearing Ammonium Groups via Flexible Spacers. *J. Mater. Chem. A* **2015**, *3* (29), 15015–15019.

(106) Mazin, P. V.; Kapustina, N. A.; Tarasevich, M. R. Direct Ethanol Oxidation Fuel Cell with Anionite Membrane and Alkaline Electrolyte. *Russ. J. Electrochem.* **2011**, *47* (3), 275–281.

(107) Vandiver, M. A.; Caire, B. R.; Carver, J. R.; Waldrop, K.; Hibbs, M. R.; Varcoe, J. R.; Herring, A. M.; Liberatore, M. W. Mechanical Characterization of Anion Exchange Membranes by Extensional Rheology under Controlled Hydration. *J. Electrochem. Soc.* **2014**, *161* (10), H677–H683.

(108) Ziv, N.; Mondal, A. N.; Weissbach, T.; Holdcroft, S.; Dekel, D. R. Effect of CO2 on the Properties of Anion Exchange Membranes for Fuel Cell Applications. *J. Memb. Sci.* **2019**, *586*, 140–150.

(109) Kusoglu, A.; Dursch, T. J.; Weber, A. Z. Nanostructure/Swelling Relationships of Bulk and Thin-Film PFSA Ionomers. *Adv. Funct. Mater.* **2016**, *26* (27), 4961–4975.

(110) Bass, M.; Berman, A.; Singh, A.; Konovalov, O.; Freger, V. Surface-Induced Micelle Orientation in Nafion Films. *Macromolecules* **2011**, *44* (8), 2893–2899.

(111) Kreuer, K.-D.; Portale, G. A Critical Revision of the Nano-Morphology of Proton Conducting Ionomers and Polyelectrolytes for Fuel Cell Applications. *Adv. Funct. Mater.* **2013**, *23* (43), 5390–5397.

(112) Zheng, Y.; Ash, U.; Pandey, R. P.; Ozioko, A. G.; Ponce-González, J.; Handl, M.; Weissbach, T.; Varcoe, J. R.; Holdcroft, S.; Liberatore, M. W.; Hiesgen, R.; Dekel, D. R. Water Uptake Study of Anion Exchange Membranes. *Macromolecules* **2018**, *51* (9), 3264–3278.

(113) Fang, S. J.; Haplepete, S.; Chen, W.; Helms, C. R.; Edwards, H. Analyzing Atomic Force Microscopy Images Using Spectral Methods. *J. Appl. Phys.* **1998**, *82* (12), 5891.

(114) Hiesgen, R.; Helmly, S.; Galm, I.; Morawietz, T.; Handl, M.; Friedrich, K. Microscopic Analysis of Current and Mechanical Properties of Nafion® Studied by Atomic Force Microscopy. *Membranes (Basel).* **2012**, *2* (4), 783–803.

(115) Hiesgen, R.; Morawietz, T.; Handl, M.; Corasaniti, M.; Friedrich, K. A. Atomic Force Microscopy on Cross Sections of Fuel Cell Membranes, Electrodes, and Membrane Electrode Assemblies. *Electrochim. Acta* **2015**, *162*, 86–99.

(116) Divekar, A. G.; Park, A. M.; Owczarczyk, Z. R.; Seifert, S.; Pivovar, B. S.; Herring, A. M. A Study of Carbonate Formation Kinetics and Morphological Effects Observed on OH $^-$ Form of Pfaem When Exposed to Air Containing CO $_2$. *ECS Trans.* **2017**, *80* (8), 1005–1011.

(117) Hara, M.; Kimura, T.; Nakamura, T.; Shimada, M.; Ono, H.; Shimada, S.; Miyatake,

K.; Uchida, M.; Inukai, J.; Watanabe, M. Effect of Surface Ion Conductivity of Anion Exchange Membranes on Fuel Cell Performance. *Langmuir* **2016**, *32* (37), 9557–9565.

(118) Kimura, T.; Akiyama, R.; Miyatake, K.; Inukai, J. Phase Separation and Ion Conductivity in the Bulk and at the Surface of Anion Exchange Membranes with Different Ion Exchange Capacities at Different Humidities. *J. Power Sources* **2018**, *375*, 397–403.

(119) Ziv, N.; Dekel, D. R. A Practical Method for Measuring the True Hydroxide Conductivity of Anion Exchange Membranes. *Electrochem. commun.* **2018**, *88*, 109–113.

(120) Bass, M.; Berman, A.; Singh, A.; Konovalov, O.; Freger, V. Surface Structure of Nafion in Vapor and Liquid. *J. Phys. Chem. B* **2010**, *114* (11), 3784–3790.

(121) Barnes, A. M.; Buratto, S. K. Imaging Channel Connectivity in Nafion Using Electrostatic Force Microscopy. *J. Phys. Chem. B* **2018**, *122* (3), 1289–1295.

(122) Mandal, M.; Huang, G.; Kohl, P. A. Highly Conductive Anion-Exchange Membranes Based on Cross-Linked Poly(Norbornene): Vinyl Addition Polymerization. **2019**.

(123) Chen, W.; Mandal, M.; Huang, G.; Wu, X.; He, G.; Kohl, P. A. Highly Conducting Anion-Exchange Membranes Based on Cross-Linked Poly(Norbornene): Ring Opening Metathesis Polymerization. **2019**.

(124) Feng, T.; Lin, B.; Zhang, S.; Yuan, N.; Chu, F.; Hickner, M. A.; Wang, C.; Zhu, L.; Ding, J. Imidazolium-Based Organic–Inorganic Hybrid Anion Exchange Membranes for Fuel Cell Applications. *J. Memb. Sci.* **2016**, *508*, 7–14.

(125) Yan, X.; Gu, S.; He, G.; Wu, X.; Benziger, J. Imidazolium-Functionalized Poly(Ether

Ether Ketone) as Membrane and Electrode Ionomer for Low-Temperature Alkaline Membrane Direct Methanol Fuel Cell. *J. Power Sources* **2014**, *250*, 90–97.

(126) Gu, S.; Skovgard, J.; Yan, Y. S. Engineering the Van Der Waals Interaction in Cross-Linking-Free Hydroxide Exchange Membranes for Low Swelling and High Conductivity. *ChemSusChem* **2012**, *5* (5), 843–848.

(127) Disabb-Miller, M. L.; Zha, Y.; DeCarlo, A. J.; Pawar, M.; Tew, G. N.; Hickner, M. A. Water Uptake and Ion Mobility in Cross-Linked Bis(Terpyridine)Ruthenium-Based Anion Exchange Membranes. *Macromolecules* **2013**, *46* (23), 9279–9287.

(128) Gu, S.; Cai, R.; Luo, T.; Chen, Z.; Sun, M.; Liu, Y.; He, G.; Yan, Y. A Soluble and Highly Conductive Ionomer for High-Performance Hydroxide Exchange Membrane Fuel Cells. *Angew. Chemie - Int. Ed.* **2009**, *48* (35), 6499–6502.

(129) Cotanda, P.; Sudre, G.; Modestino, M. A.; Chen, X. C.; Balsara, N. P. High Anion Conductivity and Low Water Uptake of Phosphonium Containing Diblock Copolymer Membranes. *Macromolecules* **2014**, *47* (21), 7540–7547.

(130) Li, N.; Leng, Y.; Hickner, M. A.; Wang, C.-Y. Highly Stable, Anion Conductive, Comb-Shaped Copolymers for Alkaline Fuel Cells. *J. Am. Chem. Soc.* **2013**, *135* (27), 10124–10133.

(131) Zhang, W.; Liu, Y.; Jackson, A. C.; Savage, A. M.; Ertem, S. P.; Tsai, T. H.; Seifert, S.; Beyer, F. L.; Liberatore, M. W.; Herring, A. M.; Coughlin, E. B. Achieving Continuous Anion Transport Domains Using Block Copolymers Containing Phosphonium Cations. *Macromolecules* **2016**, *49* (13), 4714–4722.

(132) Kumar, R.; Muthukumar, M. Microphase Separation in Polyelectrolytic Diblock Copolymer Melt: Weak Segregation Limit. *J. Chem. Phys.* **2007**, *126* (21), 214902.

(133) Rojas, A. A.; Inceoglu, S.; Mackay, N. G.; Thelen, J. L.; Devaux, D.; Stone, G. M.; Balsara, N. P. Effect of Lithium-Ion Concentration on Morphology and Ion Transport in Single-Ion-Conducting Block Copolymer Electrolytes. *Macromolecules* **2015**, *48* (18), 6589–6595.

(134) Park, M. J.; Balsara, N. P. Phase Behavior of Symmetric Sulfonated Block Copolymers. *Macromolecules* **2008**, *41* (10), 3678–3687.

(135) Sing, C. E.; Zwanikken, J. W.; Cruz, M. O. de la. Electrostatic Control of Block Copolymer Morphology. *Nat. Mater.* **2014**, *13* (7), 694–698.

(136) Kumar, R.; Muthukumar, M. Microphase Separation in Polyelectrolytic Diblock Copolymer Melt : Weak Segregation Limit Microphase Separation in Polyelectrolytic Diblock Copolymer Melt : **2017**, *214902* (2007).

(137) Jiang, Y.; Freyer, J. L.; Cotanda, P.; Brucks, S. D.; Killops, K. L.; Bandar, J. S.; Torsitano, C.; Balsara, N. P.; Lambert, T. H.; Campos, L. M. Functional Polyelectrolytes. *Nat. Commun.* **2015**, *6*, 1–7.

(138) Sing, C. E.; Zwanikken, J. W.; Olvera, M.; Cruz, D. Theory of Melt Polyelectrolyte Blends and Block Copolymers : Phase Behavior , Surface Tension , and Microphase Periodicity Theory of Melt Polyelectrolyte Blends and Block Copolymers : Phase Behavior , Surface Tension , and Microphase Periodicity. **2017**, *034902* (2015).

(139) Sing, C. E.; Olvera, M.; Cruz, D. Polyelectrolyte Blends and Nontrivial Behavior in E Ff Ective Flory − Huggins Parameters. **2014**.

(140) Sing, C. E. Development of the Modern Theory of Polymeric Complex Coacervation. *Adv. Colloid Interface Sci.* **2017**, *239*, 2–16.

(141) Perry, S. L.; Sing, C. E. PRISM-Based Theory of Complex Coacervation: Excluded

Volume versus Chain Correlation. **2015**, *v*.

(142) Irwin, M. T.; Hickey, R. J.; Xie, S.; Bates, F. S.; Lodge, T. P. Lithium Salt-Induced
Microstructure and Ordering in Diblock Copolymer/Homopolymer Blends. **2016**.

(143) Komura, M.; Yoshitake, A.; Komiyama, H.; Iyoda, T. Control of Air-Interface-
Induced Perpendicular Nanocylinder Orientation in Liquid Crystal Block Copolymer
Films by a Surface-Covering Method. *Macromolecules* **2015**, *48* (3), 672–678.

(144) Harrisson, S.; Couvreur, P.; Nicolas, J. Use of Solvent Effects to Improve Control
over Nitroxide-Mediated Polymerization of Isoprene. *Macromol. Rapid Commun.*
2012, *33* (9), 805–810.

(145) Lacroix-Desmazes, P.; Delair, T.; Pichot, C.; Boutevin, B. Synthesis of
Poly(Chloromethylstyrene-b-Styrene) Block Copolymers by Controlled Free-Radical
Polymerization. *J. Polym. Sci. Part A Polym. Chem.* **2000**, *38* (21), 3845–3854.

(146) Nakano, T.; Kawaguchi, D.; Matsushita, Y. Anisotropic Self-Assembly of Gold
Nanoparticle Grafted with Polyisoprene and Polystyrene Having Symmetric Polymer
Composition. *J. Am. Chem. Soc* **2013**, *135*, 36.

(147) Li, W.; Wang, H.; Yu, L.; Morkved, T. L.; Jaeger, H. M. Syntheses of
Oligophenylenevinylenes-Polyisoprene Diblock Copolymers and Their Microphase
Separation. **1999**.

(148) Bates, F. S.; Fredrickson, G. H. Block Copolymer Thermodynamics: Theory and
Experiment. *Annu. Rev. Phys. Chem.* **1990**, *41* (1), 525–557.

(149) Hasegawa, H.; Hashimoto, T. Morphology of Block Polymers near a Free Surface.
Macromolecules **1985**, *18* (3), 589–590.

(150) Komura, M.; Iyoda, T. AFM Cross-Sectional Imaging of Perpendicularly Oriented

Nanocylinder Structures of Microphase-Separated Block Copolymer Films by Crystal-like Cleavage.

(151) Khanna, V.; Cochran, E. W.; Hexemer, A.; Stein, G. E.; Fredrickson, G. H.; Kramer, E. J.; Li, X.; Wang, J.; Hahn, S. F. Effect of Chain Architecture and Surface Energies on the Ordering Behavior of Lamellar and Cylinder Forming Block Copolymers. *Macromolecules* **2006**, *39* (26), 9346–9356.

(152) Adams, J. L.; Quiram, D. J.; Graessley, W. W.; Register, R. A.; Marchand, G. R. *Ordering Dynamics of Compositionally Asymmetric Styrene-Isoprene Block Copolymers*; 1996.

(153) Kim, J. K.; Lee, H. H.; Ree, M.; Lee, K.-B.; Park, Y. Ordering Kinetics of Cylindrical and Spherical Microdomains in an SIS Block Copolymer by Synchrotron SAXS and Rheology. *Macromol. Chem. Phys.* **1998**, *199* (4), 641–653.

(154) Elabd, Y. A.; Napadensky, E.; Charles W. Walker, A.; Winey, K. I. Transport Properties of Sulfonated Poly(Styrene-b-Isobutylene-b-Styrene) Triblock Copolymers at High Ion-Exchange Capacities. *Macromolecules* **2006**, *39* (1), 399–407.

(155) Tanaka, M.; Fukasawa, K.; Nishino, E.; Yamaguchi, S.; Yamada, K.; Tanaka, H.; Bae, B.; Miyatake, K.; Watanabe, M. Anion Conductive Block Poly(Arylene Ether)s: Synthesis, Properties, and Application in Alkaline Fuel Cells. *J. Am. Chem. Soc.* **2011**, *133* (27), 10646–10654.

(156) Yalcin, S. E.; Labastide, J. A.; Sowle, D. L.; Barnes, M. D. Spectral Properties of Multiply Charged Semiconductor Quantum Dots. *Nano Lett.* **2011**, *11* (10), 4425–4430.

(157) Heim, T.; Lmimouni, K.; Vuillaume, D. Ambipolar Charge Injection and Transport in

a Single Pentacene Monolayer Island. *Nano Lett.* **2004**, *4* (11), 2145–2150.

(158) Jaquith, M.; Muller, E. M.; Marohn, J. A. Time-Resolved Electric Force Microscopy of Charge Trapping in Polycrystalline Pentacene. *Journ Phys. Chem. B* **2007**, *111* (27), 7711–7714.

(159) Kim, S.; Briber, R. M.; Karim, A.; Jones, R. L.; Kim, H.-C. Environment-Controlled Spin Coating To Rapidly Orient Microdomains in Thin Block Copolymer Films. *Macromolecules* **2007**, *40* (12), 4102–4105.

(160) Gu, X.; Gunkel, I.; Hexemer, A.; Russell, T. P. Controlling Domain Spacing and Grain Size in Cylindrical Block Copolymer Thin Films by Means of Thermal and Solvent Vapor Annealing. *Macromolecules* **2016**, *49* (9), 3373–3381.

(161) Barnes, A. M.; Du, Y.; Zhang, W.; Seifert, S.; Buratto, S. K.; Bryan Coughlin, E. Phosphonium-Containing Block Copolymer Anion Exchange Membranes: Effect of Quaternization Level on Bulk and Surface Morphologies at Hydrated and Dehydrated States Macromolecules XXXX, XXX, XXX−XXX. *Macromolecules* **2019**, *16*, 31.

(162) Chen, D.; Hickner, M. A. Degradation of Imidazolium-and Quaternary Ammonium-Functionalized Poly(Fluorenyl Ether Ketone Sulfone) Anion Exchange Membranes. **2012**.

(163) Park, A. M.; Owczarczyk, Z. R.; Garner, L. E.; Yang-Neyerlin, A. C.; Long, H.; Antunes, C. M.; Sturgeon, M. R.; Lindell, M. J.; Hamrock, S. J.; Yandrasits, M.; Pivovar, B. S. Synthesis and Characterization of Perfluorinated Anion Exchange Membranes. *ECS Trans.* **2017**, *80* (8), 957–966.

(164) Liscio, A.; Palermo, V.; Fenwick, O.; Braun, S.; Müllen, K.; Fahlman, M.; Cacialli, F.; Samorí, P. Local Surface Potential of π-Conjugated Nanostructures by Kelvin

Probe Force Microscopy: Effect of the Sampling Depth. *Small* **2011**, *7* (5), 634–639.

(165) Borowik, Ł.; Kusiaku, K.; Théron, D.; Mélin, T. Calculating Kelvin Force Microscopy Signals from Static Force Fields. *Appl. Phys. Lett.* **2010**, *96* (10), 103119.

(166) Fuchs, F.; Caffy, F.; Demadrille, R.; Mélin, T.; Grévin, B. High-Resolution Kelvin Probe Force Microscopy Imaging of Interface Dipoles and Photogenerated Charges in Organic Donor–Acceptor Photovoltaic Blends. *ACS Nano* **2016**, *10* (1), 739–746.

(167) Sugimura, H.; Ishida, Y.; Hayashi, K.; Takai, O.; Nakagiri, N. Potential Shielding by the Surface Water Layer in Kelvin Probe Force Microscopy. *Appl. Phys. Lett.* **2002**, *80* (8), 1459–1461.